

---

# Search for Magnetically-Induced Patterns in Cosmic Ray Arrival Directions using a new Extragalactic Filter Technique at the Pierre Auger Observatory

Von der Fakultät für Mathematik, Informatik und Naturwissenschaften der RWTH  
Aachen University zur Erlangung des akademischen Grades eines Doktors der  
Naturwissenschaften genehmigte Dissertation

vorgelegt von

**Martin Urban, M.Sc.**  
aus Aachen

Berichter:  
Universitätsprofessor Herr Prof. Dr.rer.nat Martin Erdmann  
Universitätsprofessor Herr Prof. Dr.rer.nat Thomas Hebbeker

Tag der mündlichen Prüfung: 03.05.2019

Diese Dissertation ist auf den Internetseiten der Universitätsbibliothek online verfügbar.

---



# Contents

<b>1</b>	<b>Introduction</b>	<b>1</b>
<b>2</b>	<b>Detection of Air Showers at the Pierre Auger Observatory</b>	<b>3</b>
2.1	Air Showers . . . . .	3
2.2	The Pierre Auger Observatory . . . . .	6
2.2.1	The Fluorescence Detector . . . . .	8
2.2.2	The Surface Detector . . . . .	11
<b>3</b>	<b>Key Measurements of Cosmic Rays</b>	<b>13</b>
3.1	Energy Spectrum . . . . .	13
3.2	Arrival Directions . . . . .	15
3.3	Composition . . . . .	17
3.4	Constraining Source Properties . . . . .	20
<b>4</b>	<b>Origin and Propagation</b>	<b>23</b>
4.1	Acceleration Models and Source Candidates . . . . .	23
4.2	Propagation . . . . .	26
<b>5</b>	<b>Deflections in Galactic Magnetic Fields</b>	<b>31</b>
5.1	Field Parameterizations . . . . .	33
5.2	Impact of the Galactic Magnetic Field on Cosmic Ray Arrival . . . . .	35
5.2.1	Deflection Angles . . . . .	36
5.2.2	Dispersion . . . . .	38
5.2.3	Multiple Images . . . . .	40
5.2.4	Field Transparency . . . . .	42
5.2.5	Small-scale Random Field . . . . .	45
5.3	Influences of Field Uncertainties on Cosmic Ray Arrival . . . . .	47

5.3.1	Comparison of Deflection Angles . . . . .	47
5.3.2	Comparison of Arrival Directions . . . . .	50
5.3.3	Simulated Point Source Search . . . . .	51
5.3.4	Summary of the Influence of Field Uncertainties on Cosmic Ray Arrival . . . . .	54
5.4	Conclusion . . . . .	54
<b>6</b>	<b>Experimental Setup</b>	<b>57</b>
6.1	Trigger Definitions . . . . .	57
6.1.1	Active and Non-Rejected Stations . . . . .	58
6.1.2	Active Triangles . . . . .	59
6.1.3	Implementations of the Fiducial Trigger and the Active Triangles	59
6.2	Event Reconstruction . . . . .	61
6.3	Data Selection . . . . .	64
<b>7</b>	<b>Analysis Strategy</b>	<b>69</b>
7.1	Simulation of astrophysical scenarios . . . . .	70
7.2	Backward Transformation of Cosmic Rays . . . . .	77
7.3	Search for Outstanding Extragalactic Directions . . . . .	80
7.4	Forward Transformation through the Galactic Magnetic Field . . . . .	82
7.5	Likelihood Test of Corridors in the Cosmic Ray Arrival Directions . . . . .	83
7.6	Optimization of Free Parameters . . . . .	84
7.7	Sensitivity to the Detection of Anisotropy . . . . .	88
7.8	Dependency on Magnetic Field Uncertainties . . . . .	92
7.9	Technical Implementation . . . . .	94
<b>8</b>	<b>Search for Local Structures in the Arrival Directions of Cosmic Rays</b>	<b>95</b>
8.1	Outstanding Extragalactic Directions . . . . .	95
8.2	Results of the Likelihood Test . . . . .	97
8.3	Cosmic Rays in Corridors of Arrival Directions on Earth . . . . .	99
<b>9</b>	<b>Conclusion</b>	<b>105</b>
	<b>Bibliography</b>	<b>126</b>
	<b>Danksagung - Acknowledgements</b>	<b>133</b>

# List of Figures

2.1	Schematic view of an air shower . . . . .	4
2.2	Heitler Model . . . . .	5
2.3	Layout of the Pierre Auger Observatory . . . . .	7
2.4	Surface detector station and building of the fluorescence detector . . . . .	7
2.5	Telescope of the fluorescence detector . . . . .	8
2.6	Triggered pixels at the fluorescence detector . . . . .	9
2.7	Hybrid event . . . . .	10
2.8	Measurement of the slant depth for event 39819479 . . . . .	10
2.9	Surface detector station . . . . .	11
2.10	Time distribution at the surface detector . . . . .	12
3.1	Energy spectrum of cosmic rays . . . . .	14
3.2	Energy spectrum at the highest energies . . . . .	14
3.3	Cosmic ray flux above 8 EeV . . . . .	15
3.4	Observed excess map of cosmic rays . . . . .	17
3.5	Test statistic of the comparison to different source candidates . . . . .	17
3.6	$\langle X_{\max} \rangle$ and $\sigma(X_{\max})$ measured by the Pierre Auger Observatory . . . . .	18
3.7	Average logarithm of the mass number . . . . .	19
3.8	Fit of four mass groups to the $X_{\max}$ distribution . . . . .	20
3.9	Cutoff rigidity and spectral index at the source . . . . .	21
4.1	Hillas diagram . . . . .	25
4.2	Photon background fields . . . . .	27
4.3	Energy loss length . . . . .	28
4.4	Propagation distance . . . . .	29
5.1	Galactic magnetic field strength in $x - z$ slice . . . . .	33

5.2	Example trajectories of antiprotons in the GMF . . . . .	34
5.3	Magnitude of the angular deflections $\beta$ . . . . .	35
5.4	Average angular deflections $\langle\beta\rangle$ . . . . .	37
5.5	Arrival distributions for cosmic rays with rigidity $R = 10$ EV . . . . .	38
5.6	Average extent $\langle r_{50}\rangle$ of arrival probability distributions on Earth . . . . .	40
5.7	Mean multiplicity $\langle n\rangle$ of images . . . . .	41
5.8	Observation probability and flux for JF12 model . . . . .	42
5.9	Integrated relative flux $F$ of observed cosmic rays . . . . .	43
5.10	Trajectories for antimatter and directions with unobserved matter . . . . .	44
5.11	Directions with unobserved matter . . . . .	45
5.12	Definition of angular distances . . . . .	46
5.13	Difference $\Psi$ in the directions of the deflections between JF12 and PT11 . . . . .	48
5.14	Angular distance $\delta$ of cosmic rays after deflections in JF12 and PT11 . . . . .	49
5.15	Arrival distributions on Earth using different magnetic field models . . . . .	51
5.16	Simulated point source search with ten sources . . . . .	53
6.1	Active triangle calculation . . . . .	59
6.2	Hexagons . . . . .	60
6.3	Surface detector VEM Signal . . . . .	62
6.4	Angular resolution . . . . .	63
6.5	Correlation between $S_{38}$ and $E_{\text{FD}}$ . . . . .	64
6.6	Relative event numbers and relative energy uncertainty . . . . .	66
6.7	Distribution of azimuth and zenith angles . . . . .	67
6.8	Distribution of longitude and latitude angles . . . . .	67
6.9	Integral number of events above different energies . . . . .	68
7.1	Two-point autocorrelation on hybrid data . . . . .	73
7.2	Fit of the signal fraction . . . . .	74
7.3	Signal fractions at $E_{\text{min}} = 12$ EeV . . . . .	74
7.4	Simulated energy and charge spectra . . . . .	75
7.5	Simulated arrival directions . . . . .	76
7.6	Backward transformation of a cosmic ray with $E = 160$ EeV . . . . .	78

---

7.7	Bwardack transformation through the galactic magnetic field . . . . .	79
7.8	Outstanding directions filtered by the DBSCAN algorithm . . . . .	80
7.9	Schematic view of the DBSCAN algorithm . . . . .	81
7.10	Forward transformed signal contribution . . . . .	83
7.11	Test statistic as function of the parameters of the likelihood fit . . . . .	84
7.12	Number of filtered extragalactic regions . . . . .	85
7.13	Probabilities to detect no outstanding region . . . . .	86
7.14	Distribution of the test statistic . . . . .	87
7.15	Significance as function of the two parameters of the cluster algorithm . . . . .	88
7.16	Test statistic ratio for two iterations . . . . .	88
7.17	Expected sensitivity . . . . .	89
7.18	Median angular distance of the center of the closest corridor . . . . .	89
7.19	Angular distances between filtered extragalactic corridors and sources . . . . .	90
7.20	Efficiency and purity . . . . .	91
7.21	Simulation of the directional uncertainty of the GMF . . . . .	92
7.22	Angular distance and test statistic for a rotated GMF . . . . .	93
7.23	Direction of the closest filtered corridor for rotated GMF . . . . .	94
8.1	Backward transformed measured cosmic rays . . . . .	96
8.2	Outstanding extragalactic regions . . . . .	96
8.3	Deviation from isotropy assuming neutral particles and anti-particles . . . . .	97
8.4	Distribution of the test statistic . . . . .	98
8.5	Comparison of the test statistic to isotropic simulations . . . . .	99
8.6	Energy distribution of correlating cosmic rays . . . . .	100
8.7	Best fitting rigidity of correlating cosmic rays . . . . .	101
8.8	Charge distributions for two cosmic rays . . . . .	102
8.9	Charge distribution map . . . . .	103



# Abbreviations

<b>ADST</b>	Advanced Data Summary Tree
<b>AERA</b>	Auger Engineering Radio Array
<b>AGASA</b>	Akeno Giant Air Shower Array
<b>AGN</b>	Active Galactic Nucleus
<b>CDAS</b>	Central Data Acquisition System
<b>CLF</b>	Central Laser Facility
<b>CMB</b>	Cosmic Microwave Background
<b>CNO</b>	Carbon Nitrogen Oxygen
<b>CO</b>	Coihueco
<b>CPU</b>	Central Processing Unit
<b>CR</b>	Cosmic Ray
<b>CRB</b>	Cosmic Radio Background
<b>DBSCAN</b>	Density-Based Spatial Clustering of Applications with Noise
<b>EAS</b>	Extensive Air Shower
<b>EBL</b>	Extragalactic Background Light
<b>EGMF</b>	Extragalactic Magnetic Field
<b>FD</b>	Fluorescence Detector
<b>FoV</b>	Field of View
<b>GMF</b>	Galactic Magnetic Field
<b>GPS</b>	Global Positioning System
<b>GPU</b>	Graphics Processing Unit
<b>GRB</b>	Gamma Ray Burst
<b>GZK</b>	Greisen Zatsepin Kuzmin
<b>HEAT</b>	High Elevation Auger Telescopes
<b>HiRES</b>	High Resolution Fly's Eye
<b>ICRC</b>	International Cosmic Ray Conference
<b>JF12</b>	Jansson and Farrar model from 2012
<b>KASCADE</b>	Karlsruhe Shower Core and Array Detector
<b>LDF</b>	Lateral Distribution Function
<b>LHC</b>	Large Hadron Collider
<b>LA</b>	Loma Amarilla
<b>LL</b>	Los Leones
<b>LM</b>	Los Morados

<b>NKG</b>	Nishimura Kamata Greisen
<b>NumPy</b>	Library for numerical computation within Python
<b>PDF</b>	Probability Density Function
<b>PMT</b>	Photomultiplier tube
<b>PT11</b>	Pshirkov and Tinyakov model from 2011
<b>PT11-ASS</b>	Axialsymmetric spiral model from Pshirkov and Tinyakov
<b>PT11-BSS</b>	Bisymmetric spiral model from Pshirkov and Tinyakov
<b>RD</b>	Radio Detector
<b>SciPy</b>	Library for scientific computation within Python
<b>SBG</b>	Starburst Galaxy
<b>SD</b>	Surface Detector
<b>SSD</b>	Scintillator Surface Detector
<b>TA</b>	Telescope Array
<b>TH</b>	Threshold
<b>ToT</b>	Time over Threshold
<b>UHECR</b>	Ultra-High Energy Cosmic Ray
<b>VEM</b>	Vertical Equivalent Muon
<b>XLF</b>	eXtreme Laser Facility

# 1. Introduction

The Earth is hit constantly from all directions by particles from outer space. These cosmic rays contribute significantly to the background radiation on Earth [1] which was detected in 1912 by Victor Hess and honored with the Nobel prize in 1936. When an ultra-high energy cosmic ray (UHECR) with an energy above 1 EeV interacts with molecules in the atmosphere an extensive air shower evolves consisting of a cascade of secondary particles.

The world's largest detector for air showers, the Pierre Auger observatory in Argentina, which is named after one of the discoverers of air showers [2, 3, 4], already detected cosmic rays with energies above 100 EeV. This is several orders of magnitude higher than the single particle energy produced at the most powerful human built accelerator, the LHC at CERN with a design energy of 14 TeV. The answer to the questions how and where these energies can be reached remains unclear up to today as the sources are not yet detected. Typically, searches for sources can be grouped into two categories: firstly, comparisons of the arrival directions of cosmic rays to source catalogs obtained from observations e.g. by radio telescopes. Here, an evidence is found that a selection of star burst galaxies describes the measured directions better than a purely isotropic background [5]. Analyses of the second category try to reveal anisotropies by advanced transformations of the observables. The most important result in these searches where no source model is assumed is the discovery of a dipolar structure in the arrival directions of cosmic rays [6]. However, this does not directly allow a selection of a set of sources although it might be a hint that the sources could be in the direction of the supergalactic plane.

The search for the sources of UHECRs is subject to a particular challenge, the deflection in magnetic fields, which means that the measured directions do not point straight back to the sources. The peculiarity is that the deflections depend on the structure of the magnetic field, the energy and the charge of the cosmic particle, but only energy and arrival direction are directly measured. The reconstruction of the mass and thus the charge of the primary cosmic ray is demanding as in air showers only secondary particles are measured. Note that the energy can be obtained from the number of secondary particles and that a direct measurement of cosmic rays at the highest energies is not feasible due to the low flux in the order of one particle per square kilometer and year.

Magnetic fields exist inside and outside our galaxy. The extragalactic space consists mainly of voids and thus these fields are believed to be weak although estimates of the strength differ in several orders of magnitude [7, 8]. Models of the galactic magnetic field are tuned to measurements of Faraday rotation and synchrotron emission.

Within the scope of this thesis different models are investigated by comparing their impact on cosmic ray deflection. Furthermore, a filter method is developed searching for overdense thread-like structures in the arrival directions of cosmic rays matching the expected deflections in a galactic magnetic field model. It makes use of the fact, that the natural frame to find a point source are the directions of cosmic rays before they are affected by the dominating deflections of the galactic magnetic field. In this frame outstanding directions above isotropic expectations are filtered and evaluated in a log-likelihood method. Starting with these outstanding directions, their predicted directions on Earth including deflections in the galactic magnetic field are compared to the directions of the measured UHECRs. The combination of correcting the deflections of UHECRs in the galactic magnetic field and applying the model to the filtered directions allows to partly compensate the uncertainties in the galactic magnetic field models. This is similar to a frequency filter where a signal is filtered out by applying a Fourier transformation and its inverse. A slightly mistuned transformation still allows to filter out a signal in the frequency domain and thus to remove noise in the time domain. The method is developed and optimized on the basis of astrophysical simulations, and then applied in a search for outstanding directions in the measured data of the surface detector of the Pierre Auger observatory.

This thesis is structured as follows, first air showers and the Pierre Auger observatory are presented (chapter 2), afterwards the most important measurements in UHECR physics are shown (chapter 3). Next, models for the sources and acceleration mechanisms are depicted (chapter 4). In chapter 5 the impact of different galactic magnetic field models on the deflections of cosmic rays is investigated. Then, the experimental setup leading to a selection of a data set is shown (chapter 6). The filter method is presented in chapter 7. Here, different parameters e.g. for the filtering algorithm and the impact of uncertainties of the galactic magnetic field are studied. Finally, the analysis is applied to the selected data set in chapter 8.

## 2. Detection of Air Showers at the Pierre Auger Observatory

Cosmic rays reaching Earth interact with the particles in the atmosphere and develop an air shower. Here, secondary particles are created in a cascade of interactions; at the highest energies a so-called extensive air shower (EAS) typically has a spread of several square kilometers on ground. The measurement of EAS allows to reconstruct properties like energy and incoming direction of the primary cosmic rays. The largest cosmic ray observatory on Earth is the Pierre Auger Observatory in Argentina. It is equipped with various detector types allowing it to measure both the longitudinal profile and the lateral distribution of particles in an extensive air shower.

This section is structured as follows: First, air showers are presented (section 2.1), then the Pierre Auger Observatory is described (section 2.2). Here, emphasis is given to the presentations of the Fluorescence Detector (FD) and the Surface Detector (SD).

### 2.1 Air Showers

A primary ultra-high energy cosmic ray (UHECR) interacting with a molecule in the atmosphere produces secondary particles that themselves still have very high energies allowing them to produce more and more particles in a cascade. When reaching ground an EAS typically has a size of several square kilometers depending on its zenith angle.

The particles in an EAS are typically divided into three groups, see figure 2.1. The hadronic component mainly consists of protons  $p$ , neutrons  $n$  and the unstable kaons  $K^\pm$  and pions  $\pi^\pm$ . Their decays feed the muonic and electronic components. Neutrinos are also often included to the former, sometimes they are also considered as a separate component due to their low interaction probability with matter, which makes their measurement difficult.

Modeling of air showers is computationally challenging due to the enormous number of particles i.e. more than  $10^{10}$  [10, 11, 12, 13]. However, the electromagnetic cascade consisting of photons, electrons and positrons is described in a simplified model by Heitler [14], see figure 2.2. The latter lose energy by bremsstrahlung whereas photons typically convert in the electric field of a nearby atom into an electron positron pair via the pair production process. This is the dominant interaction process for photon energies above twice the electron mass  $E_\gamma = 2m_e \approx 1 \text{ MeV}$  [15]. Both processes can

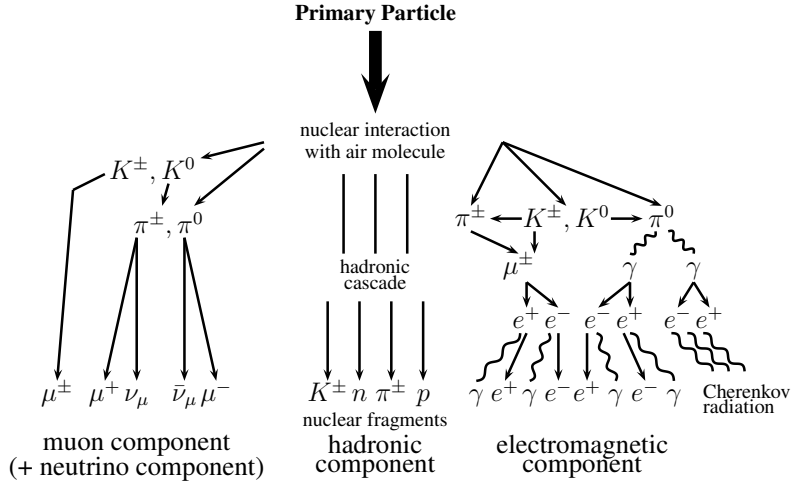


Figure 2.1: Schematic view of an air shower showing the muon, hadronic, and electromagnetic component. Modified from [9].

be described by the amount of traversed matter before interaction which is called the radiation length  $X_0$ . For photons,  $X_0$  corresponds to the mean free path  $\lambda = \rho/X_0$  for pair production whereas for electrons and positrons  $X_0$  is defined as the mean distance after which their energy is reduced to  $1/e$ . Typical values for the mean free path in air are in the order of  $6.8 \cdot 10^{-8}$  m [16] depending on humidity, temperature, and density  $\rho$ , leading to  $X_0 \approx 37 \text{ g cm}^{-2}$  [13].

The Heitler model assumes that  $X_0$  is equal for photons, electrons and positrons. Thus, the progression of the shower in the atmosphere does not depend on the type of the initial particle and can be described in  $n$  steps of  $X_0$ . An initial particle with energy  $E_0$  has produced  $2^n$  particles in the shower after  $n$  steps with each having an energy  $E_n = \frac{E_0}{2^n}$  assuming that the energy is equally distributed. This process continues until a critical energy  $E_{\text{crit}} \approx 85 \text{ MeV}$  is reached [11, 14]. The corresponding atmospheric depth where the shower has reached its maximum of particles can be calculated directly from the initial energy

$$X_{\text{max}} = \frac{\ln\left(\frac{E_0}{E_{\text{crit}}}\right)}{\ln 2} \cdot X_0. \quad (2.1)$$

Summarizing, the Heitler model allows to predict the proportionality between the initial energy  $E_0$  and the maximum number of reached particles  $N_{\text{max}} = E_0/E_{\text{crit}}$  and the logarithmic dependency of the shower maximum on the initial energy, see equation (2.1). However, the model does not allow to make precise predictions due to its simplifying assumptions, e.g. the predicted ratio between the number of photons  $N_\gamma$  and the total number of electrons and positrons  $N_{e^\pm}$  is  $N_{e^\pm}/N_\gamma = 2$  whereas measurements report typically a ratio  $\approx 6$  [17]. This discrepancy can be understood with the knowledge that bremsstrahlung typically does not produce a single photon. Note that the Heitler model has been extended to provide a higher precision or even to approximate the hadronic component of the shower [11, 18].

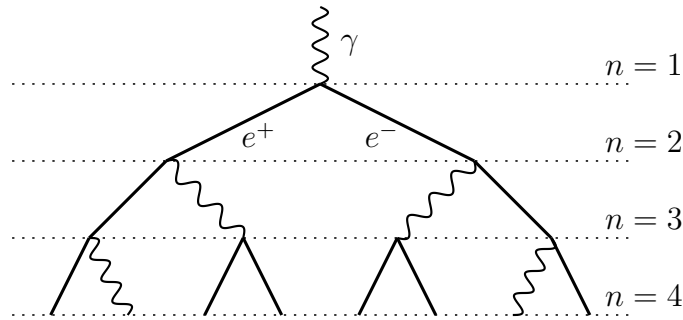


Figure 2.2: Heitler model of an electromagnetic cascade. Electrons and positrons are created from a photon via pair-production, both radiate off a photon via the Bremsstrahlung process, modified from [11].

The hadronic component is created in the first interaction but its description is more complicated as various particle types and multiparticle decays have to be taken into account. Typically air shower simulation software [10, 12] is connected to one of the following hadronic interaction models EPOS-LHC [19], SIBYLL-2.3c [20, 21] and QGSJETII-04 [22] to create hadrons taking the different cross sections into account. These models are tuned to data measured with high precision at the Large Hadron Collider (LHC) at a center of mass energy of  $E = 13$  TeV leading to accurate predictions at these energies. However, ultra-high energy cosmic rays with energies  $E \geq 10^{20}$  eV are observed [23] and thus, the required extrapolation used by the hadronic interaction models is a major source of uncertainty for simulations. One of the largest discrepancies between simulation and observation is the muon excess in measurements [24]. Despite these uncertainties, the shower maximum, including the muonic and hadronic components, is similar to the maximum of the electromagnetic shower component as the electromagnetic particles outnumber the hadronic and muonic components [11, 13].

For a complete description of air showers, their incoming zenith angles  $\theta$  and the dependency of the air density  $\rho$  on the height  $h$  have to be taken into account. This leads to the concept of the slant atmospheric depth

$$X(\theta, h) = \frac{1}{\cos \theta} \int_h^\infty \rho(h') dh'. \quad (2.2)$$

Note, in analogy to modern detectors in high energy physics the atmosphere plays the role of the calorimeter in air shower physics.

After the shower has reached its maximum  $X_{\max}$ , the number of particles decreases again due to decays of the unstable mesons (mainly  $K^\pm$ ,  $\pi^\pm$ ) and muons. This longitudinal profile of the number of particles  $N(X)$  as a function of the atmospheric depth  $X$  has first been described by the Gaisser-Hillas parameterization [25]

$$N(X) = N_{\max} \left( \frac{X - X_1}{X_{\max} - X_1} \right)^{\frac{X_{\max} - X_1}{\lambda_{\text{int}}}} \cdot \exp \left( - \frac{X_{\max} - X}{\lambda_{\text{int}}} \right). \quad (2.3)$$

Here,  $X_1$  is the depth of the first interaction and  $\lambda_{\text{int}}$  the interaction length. Due to the proportionality between the number of particles and the energy, the integration of the parameterization allows to estimate the energy of the primary cosmic ray.

When the shower reaches the ground, it typically contains only electrons and muons. There exist many parameterizations for their lateral distribution function (LDF) on ground which are typically based on the Nishimura-Kamata-Greisen (NKG) function [26, 27]. It describes the particle density on ground as a function of the distance  $r$  to the shower center, the phenomenological shower age  $s = \frac{3X}{X+2X_{\text{max}}}$  and the electron shower size  $N_e$  [28].

$$\rho_{\text{NKG}}(r, s, N_e) = \frac{N_e}{r_M^2} \cdot \frac{\Gamma(4.5 - s)}{2\pi\Gamma(s)\Gamma(4.5 - 2s)} \cdot \left(\frac{r}{r_M}\right)^{s-2} \cdot \left(1 + \frac{r}{r_M}\right)^{s-4.5} \quad (2.4)$$

Here,  $r_M$  is the Molière radius and  $\Gamma$  the gamma function. Most experiments use an optimization of this function concerning their detector layout or variations providing a better description for electrons or muons [28, 29, 30, 31, 32].

## 2.2 The Pierre Auger Observatory

The Pierre Auger observatory is the world's largest observatory for the detection of air showers induced by ultra-high energy cosmic rays. It is located in Argentina in the Pampa Amarilla close to the city Malargüe in the province Mendoza. The observatory was built from 2004 – 2008. The recent approval of a detector upgrade secures its operation until 2025. It is equipped with different types of detectors, see figure 2.3. They allow hybrid measurements of air showers achieving a better accuracy than a reconstruction by only a single detector type [33]. The picture in figure 2.4 displays the two original detector types, a building of the fluorescence detector (FD) and a station of the surface detector (SD).

The FD is composed of 24 telescopes at the 4 locations Coihueco (CO), Los Leones (LL), Loma Amarilla (LA) and Los Morados (LM). At Coihueco, 3 additional High Elevation Auger Telescopes (HEAT) have been installed to detect lower energetic particles which typically have a lower  $X_{\text{max}}$  value, see equation (2.1). The FD measures the longitudinal profile of an air shower. More details can be found in section 2.2.1.

The SD consists of 1660 water Cherenkov stations distributed in a hexagonal grid with a spacing of 1500 m leading to a total instrumented area of 3000 km<sup>2</sup> [34]. Additional stations with a spacing of 750 m (Infill) extend the SD array close to Coihueco. The individual stations measure the passage of the ultra-relativistic particles in the shower front such that the combination of all stations allows to record the footprint of an EAS. The SD is described more precisely in section 2.2.2.

Recently, the Auger Engineering Radio Array (AERA) became part of the observatory. Its radio antennas allow a third independent measurement of cosmic rays by measuring the radio footprint of an extensive air shower. For an overview of AERA see [35, 36, 37, 38]. A full overview over the Pierre Auger Observatory can be found in [39].

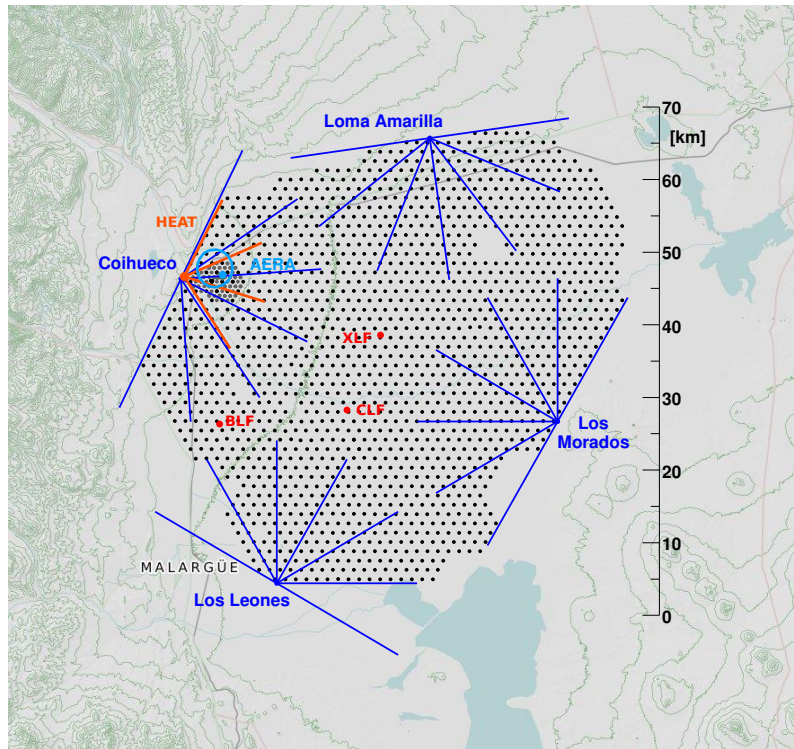


Figure 2.3: Layout of the Pierre Auger Observatory. The black dots denote the surface detector array, the telescopes of fluorescence detector are marked by the blue triangles. Different laser facilities serve monitoring and calibration purposes (XLF, CLF, BLF). The radio antenna array AERA is located close to the low energy extension HEAT and Infill. Taken from [40].



Figure 2.4: Surface detector station with solar panel GPS and communication antenna in the foreground. In the FD building the shutters for the telescopes are closed. The antenna next to the FD building is connected to the data acquisition system of the SD array.

### 2.2.1 The Fluorescence Detector

The charged particles in an air shower can excite nitrogen in the air which in turn isotropically emits fluorescent light during relaxation. The light is produced proportionally to the energy dissipation of an air shower in the atmosphere [41, 42]. Thus, the atmosphere works like a calorimeter [43].

Light reaching a telescope first passes through an opened shutter and a UV filter before being focused by a segmented mirror onto the camera consisting of 440 photomultipliers (PMT), see figure 2.5. The PMTs are connected to a high voltage required to amplify the signal and the readout electronics. The demands on electronics are high, since it has to support a large signal range per PMT, but on the other hand has to deal with a temporally changing photon background. Due to the high amplification, the telescopes can only be operated in dark moonless nights. Bad weather conditions or the presence of the moon within  $5^\circ$  of the field of view (FoV) of a telescope further reduce the total uptime fraction to an average value of 13 % [44].

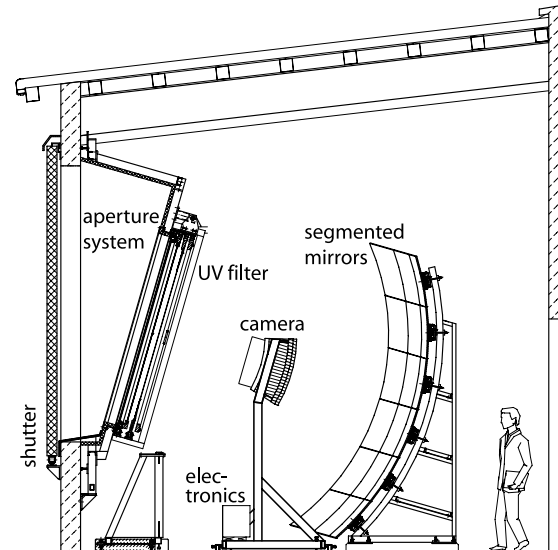


Figure 2.5: Schematic view of a telescope of the fluorescence detector. The shutter is closed at daytime and closes automatically when too much light is detected by the camera. The UV light is filtered by the UV filter and the mirror focuses the light onto the pixels of the camera. Taken from [45].

The system has an absolute and a relative calibration mode. For the absolute calibration a large light source with a diameter of 2.5 m is placed at the telescope aperture illuminating each pixel with the same flux. The relative calibration is executed at the beginning and the end of each night shift with LEDs emitting light at 5 different wavelengths from 320 nm to 405 nm to monitor short and long time changes in the detector response. The atmosphere is also monitored as humidity and especially aerosol content influence the scattering of fluorescence light in the air. The aerosol content is measured continuously by different laser systems, namely the eXtreme

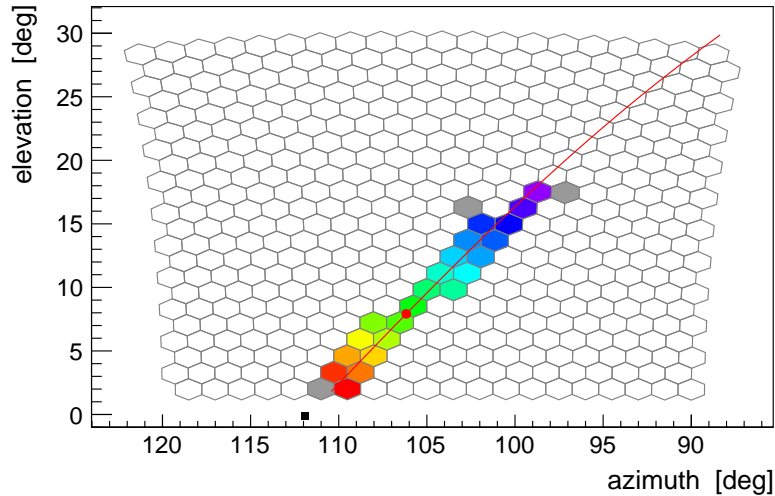


Figure 2.6: Triggered pixels at Los Morados for an event with SdId = 39819479.

Laser Facility (XLF), the central laser facility (CLF) and the lidars installed behind each FD building. The amount of the back-scattered light allows to estimate the aerosol content in the atmosphere.

Figure 2.6 displays the triggered pixels of a hybrid event measured at Los Morados. The field of view of each telescope is  $30^\circ \times 30^\circ$  in azimuth and elevation. The color code denotes the trigger time of the pixels with purple being an early time and red the latest time. The gray pixels are removed from the reconstruction of the direction shown as red line. Often showers pass through the field of view of neighboring telescopes such that the reconstruction is typically performed per FD eye consisting of 6 telescopes.

Generally, the directional reconstruction starts by first estimating the shower detector plane and than later calculating the pointing direction  $\chi_i$  in this plane of each pixel to the ground. When denoting the angle and time when the shower has its smallest distance  $R_p$  to the detector with  $\chi_0$  and  $t_0$ , the arrival times of the individual pixels are calculated by  $t_i = t_0 + R_p/c \cdot \tan [(\chi_0 - \chi_i)/2]$  allowing to fit the arrival direction. Here,  $c$  is the speed of light.

The uncertainties can be estimated by reconstructing the known direction of laser shots provided by the CLF. Note that the reconstruction of the direction of events measured by FD works best when at least one SD station is triggered, as closest distance  $R_p$  and the corresponding time  $t_0$  and angle  $\chi_0$  can not be well determined when the track in the telescope is short. In this so-called hybrid reconstruction, the resolutions of the location of the shower core and the arrival direction are better than 50 m and  $0.6^\circ$  respectively.

Figure 2.7 shows the measurement of one event by all FD telescopes. The red lines display the individually reconstructed directions from the four telescopes, the blue line the average direction. The surface detector is denoted by the array of gray dots; its reconstruction of the event is shown in section 2.2.2.

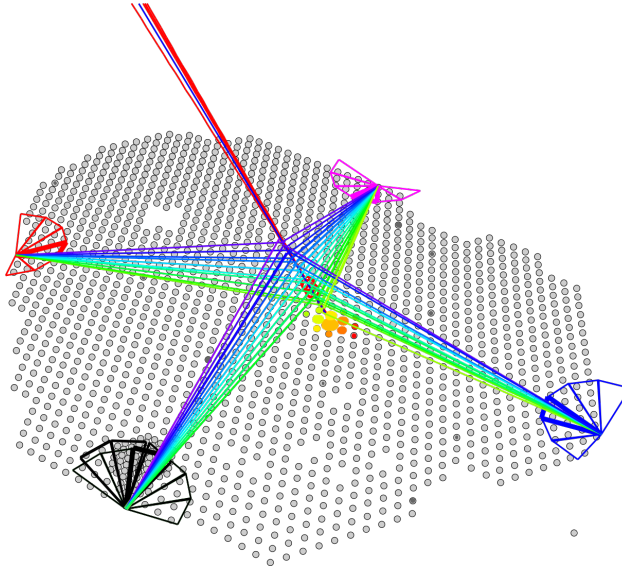


Figure 2.7: Hybrid event with SdId = 39819479 measured 6 October 2016 in the central part of the array. All four FD telescopes and the surface detector independently reconstructed the event with an average energy of 41 EeV.

The energy deposit  $dE/dX$  in the atmosphere as function of the slant depth is shown in figure 2.8. Corrections for atmospheric effects such as the attenuation due to aerosols are already applied, for more details see [45]. The depth of the shower maximum  $X_{\max}$  is clearly visible at  $\sim 700 \text{ g cm}^{-2}$ . The fit of the Gaisser-Hillas function, see equation (2.3), has a  $\chi^2/\text{Ndof} = 0.88$  and is shown by the red line. A first energy estimate can be obtained by integration of the profile. However, to reconstruct the full energy corrections have to be applied. The correction with the greatest impact is the invisible energy correction, taking into account energy carried away by neutrinos and high energy muons, similar to modern detectors in high energy physics.

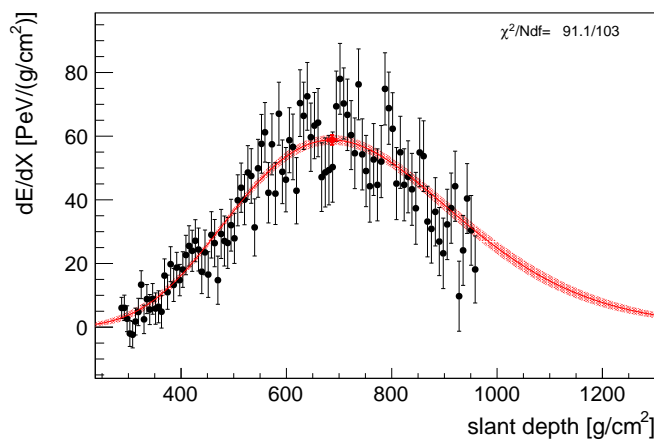


Figure 2.8: Measurement of the slant depth for the event with SdId = 39819479 at Los Leones. For more details refer to the text.

### 2.2.2 The Surface Detector

The surface detector consists of 1660 tanks as depicted in figure 2.9. Particles of an EAS traversing a station emit Cherenkov light in the ultra purified water which can then be measured by three photomultipliers (PMT). The usage of ultra purified water is required to reduce the attenuation of the Cherenkov light and to allow a stable operation for at least 20 years. The stations are placed on a hexagonal grid with a spacing of 1500 m and thus the shower is sampled at discrete points. The station diameter of 3.6 m is chosen such that the sampling error in the number of particles is below 20 % at a distance of 1000 m from the core of a shower induced by a primary cosmic ray with an energy of 10 EeV [34]. The height of the water in the station is at 1.2 m allowing to absorb 85 % of the electromagnetic component of the shower at a distance of 100 m from the core whereas passing muons create a signal proportional to their geometric path length.

The water is contained in a Tyvek foil which has the task to reflect the light to the PMT sitting at the top of the detector. Each station is equipped with a solar panel and a battery box which allows for an independent operation with a duty cycle of almost 100 %. Further equipment includes a communication antenna sending timing and position information obtained from the GPS receiver and trigger information to the central data acquisition system (CDAS).

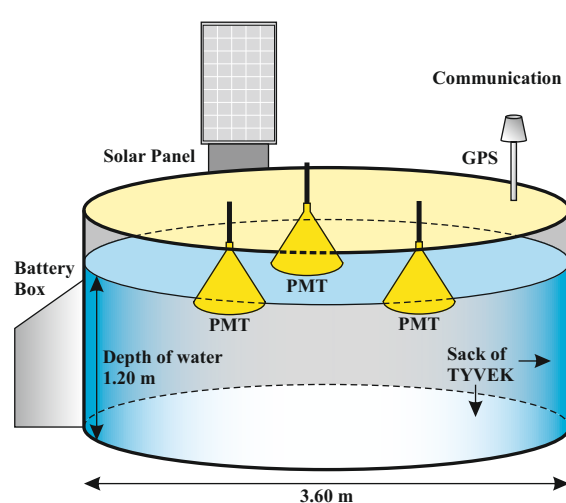


Figure 2.9: Schematic view of a surface detector station containing more than 12 000 l of ultra purified water [34].

The arrival times measured by multiple SD stations as a function of the distance to the shower core are shown in figure 2.10. From a fit of a parabolic shower front a first estimate can be made on the direction of the shower and thus the primary cosmic ray. A fit of the NKG lateral density function, see equation (2.4), to the signal strength observed in each station allows to estimate the energy. Note that the calorimetric energy measurement in the FD is used to perform an absolute calibration of the energy measurement in SD [43, 46]. Since the triggers of the SD were extended in the scope of this work, a more detailed description of the reconstruction from

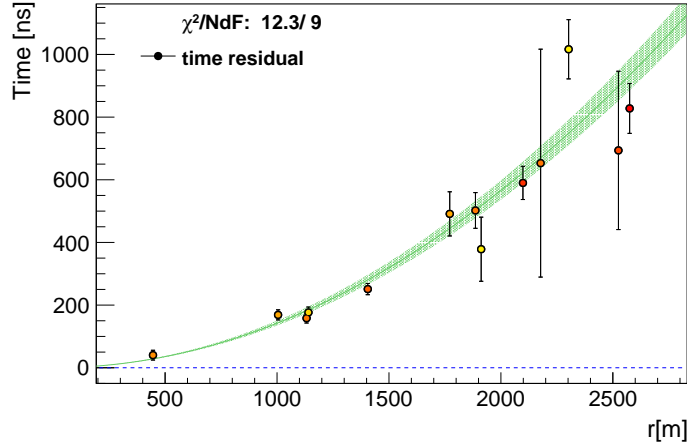


Figure 2.10: Signal times of the surface detector used to reconstruct the shower direction.

triggering events up to the energy reconstruction of the primary cosmic ray can be found in chapter 6.

Similar to the extension HEAT of FD, the SD has been extended by the so called Infill array allowing to measure cosmic rays at lower energies [47]. This was achieved by reducing the distance between the stations to 750 m leading to a full efficiency at energies above 0.3 EeV which is ten times lower than for the regular SD array. The array is placed in the FoV of Coihueco allowing to measure hybrid events together with the HEAT detector or the radio extension AERA. A further extension is called AMIGA [48] and consists of buried detectors allowing for a better measurement of the muonic component of the shower, which is essential to investigate the mass of the primary particle. Furthermore, all surface detector stations will be upgraded by an additional scintillator bar on top allowing for a better muon measurement in the original stations [49].

# 3. Key Measurements of Cosmic Rays

Since the discovery of cosmic rays, the field of research and thus the understanding of the universe has grown steadily. The purpose of this chapter is to present the most important observations of cosmic rays with a focus on ultra-high energy cosmic rays (UHECR). First, the energy spectrum is presented before key measurements related to the arrival directions are introduced. Afterwards, the results of the composition measurements are shown. Finally, it is described which conclusions can be drawn about the sources of UHECRs from these measurements.

## 3.1 Energy Spectrum

Cosmic rays are measured over a vast energy range with a flux  $F(E)$  ranging over several orders of magnitude in energy  $E$ , see figure 3.1. At the lowest energies below  $\sim 1$  PeV the fluxes are high allowing for a direct measurement with satellite [50, 51] or balloon [52, 53] based experiments. Observations at intermediate and high energies above  $\sim 1$  PeV are typically achieved with a detector array on ground which indirectly measures the cosmic rays via air showers [54, 55, 56, 57, 58, 59, 60, 61]. At the highest energies above  $\sim 1$  EeV the flux is in the order of  $1 \text{ km}^{-1} \text{ yr}^{-2} \text{ sr}^{-1}$  such that the sizes of the experiments are huge [62, 63, 64, 65].

Generally, the energy spectrum can be described by a power law  $dN/dE \propto E^{-\gamma}$ . However, it has three prominent points at which the spectral index  $\gamma$  changes. The origins of these changes are one of the outstanding questions in astroparticle physics. At the knee at  $\sim 4$  PeV the slope increases from  $\gamma \approx 2.7$  to  $\gamma \approx 3.1$ . Various approaches to explain this feature include considering it as a property of the acceleration process [66] or a linking to leakage from the galaxy [67] or interactions in the interstellar medium [68]. Some models also investigate new physics processes [69]; for a full review see [70]

At the second knee at  $\sim 400$  PeV the spectrum becomes harder again with  $\gamma \approx 3.3$  [71, 72, 73]. Its origin is often believed to be the end of the spectrum of cosmic rays with a galactic origin with a fading out of lighter components [74].

The ankle is found at 4 EeV where the spectrum flattens, interestingly to a similar spectral index of  $\gamma = 2.7$  as at low energies. This has been measured with a high statistical significance by the Telescope Array and Pierre Auger collaborations as shown in figure 3.2. Both spectra are in good agreement when increasing Auger

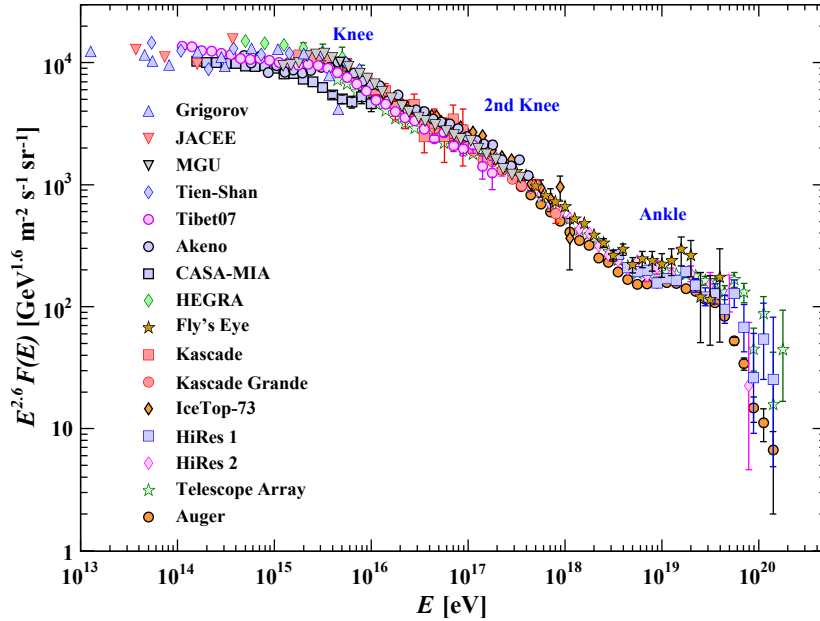


Figure 3.1: Energy spectrum of cosmic rays measured by different air shower experiments [15], data from [50]-[65].

energies by +5.2% and decreasing TA energies by  $-5.2\%$ . Such shifts are well within the individual systematic uncertainties [76]. Two interpretations for the origin of the ankle are currently discussed, either due to the extragalactic flux starting to dominate the galactic flux of cosmic rays, or a dip structure produced by energy losses of ultra-high energy protons occurring when a photon of the cosmic microwave background converts into an electron positron pair in the field of the proton. The

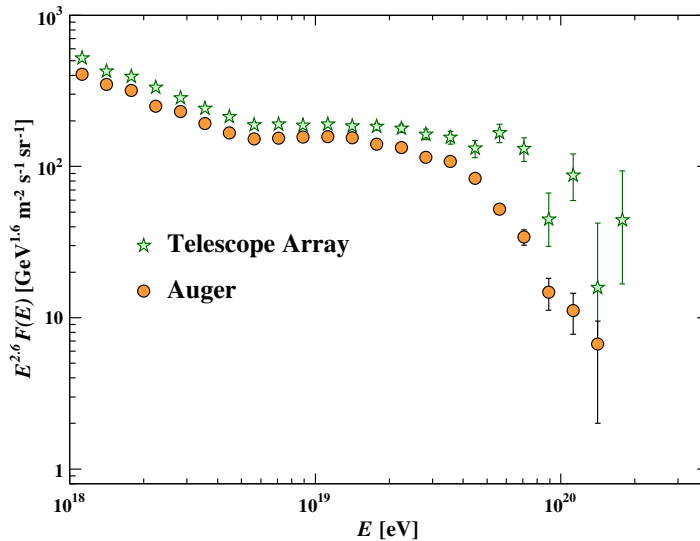


Figure 3.2: Energy spectrum at the highest energies measured by the Pierre Auger Observatory [75] and the Telescope Array (TA) [64]. Figure taken from [15].

composition plays an important role in this discussion since the measured heavy composition disfavors the dip models [77]. Here, the interpretation of data measured by the Telescope Array collaboration yields a light composition, whereas the results from the Pierre Auger collaboration tend to a heavier composition as depicted in section 3.3.

At the highest energies above 50 EeV both experiments observe a further steepening of the spectrum. This might be an indication that the acceleration mechanisms at the sources are not capable of producing higher energies. Alternatively, it can be explained by interactions during the propagation of UHECRs; for further details see chapter 4.

## 3.2 Arrival Directions

Next to the measurement of the energy spectrum, the investigation of the arrival directions of UHECRs for anisotropies is one of the key aspects in astroparticle physics. Here, two different types of analyses have to be distinguished: first, detecting anisotropy from the arrival directions themselves by investigating suitable variables and second, analyses comparing the measured directions to catalogs of source candidates motivated by other experiments or theory. For the first type of analysis, the most important observation is the detection of a large scale anisotropy for cosmic rays above 8 EeV detected with a significance at the level of  $5.2\sigma$ , see figure 3.3. It can be described by a dipole at a galactic longitude  $l = -127^\circ$  and galactic latitude  $b = -13^\circ$  with an amplitude of 6.5% [6]. The angular distance of the dipole from the galactic center is  $125^\circ$  indicating an extragalactic origin. It is also possible that galactic and extragalactic magnetic fields deflect cosmic rays originating from

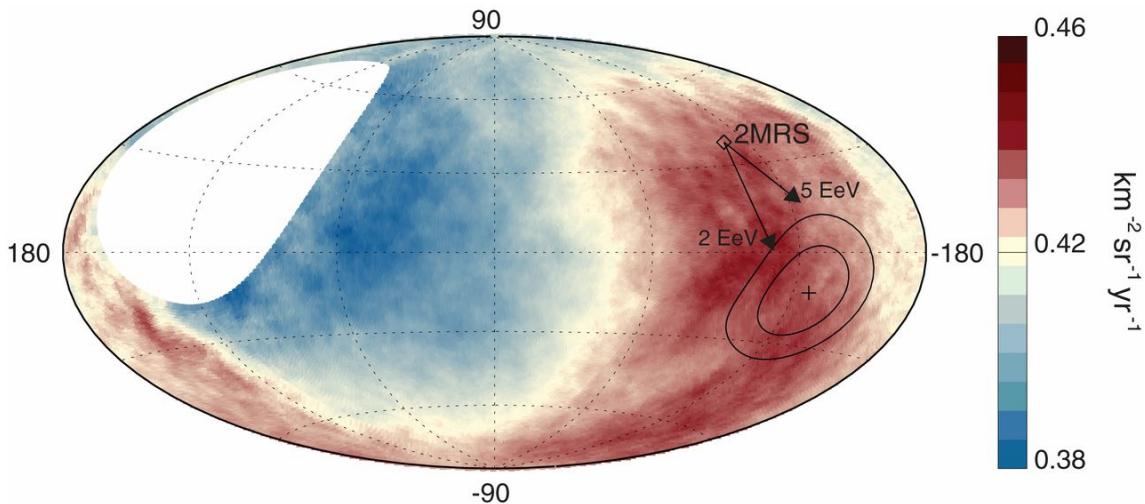


Figure 3.3: Cosmic ray flux above 8 EeV smoothed with a  $45^\circ$  top-hat function [6]. The 68% and 95% confidence levels are shown as black contours. The dipole of the 2MRS galaxy distribution [78] is denoted as well as its deflection in the galactic magnetic field model from Jansson and Farrar [79] assuming two different rigidities.

non-homogeneously distributed sources, i.e. sources in the 2MRS catalog [80]. The distribution of the source candidates in this catalog itself has a dipolar structure. To discover the origin of the dipole further analysis is required, i.e. of its dependency on energy and rigidity. The analyses of the angular power spectrum and needlets further confirm the detection [81].

Another variable allowing to investigate anisotropies without comparing to catalogs is the two-point autocorrelation capable of finding overdensities in the data by comparing the angular distances between all cosmic rays to isotropic simulations. Here, no significance was found [82]. Also a search for correlations between the arrival direction of UHECRs and the inverse of the energy as a hint on alignment of cosmic rays in a coherent magnetic field was performed, but the found multiplets do not show any significant deviation from the isotropic distribution [83]. The same holds for an analysis of the angular power spectrum using a combined data set of the Pierre Auger and Telescope Array collaborations [84]. However, the Telescope Array collaboration found a direction with an intermediate scale anisotropy and a chance probability in an isotropic sky corresponding to  $3.4\sigma$  [85]. Note that this direction is outside the field of view of the Pierre Auger observatory.

Comparisons of the arrival directions of cosmic rays to a catalog of sources are typically performed by a likelihood analysis

$$\ln \mathcal{L} = \sum_{i \in \text{CRs}} \ln (f \cdot S_{\delta}(l_i, b_i) + (1 - f) \cdot B(l_i, b_i)). \quad (3.1)$$

Here,  $S$  is the signal distribution motivated by the catalog with an additional smearing  $\delta$ . It is evaluated for each cosmic ray  $i$  at the measured longitude  $l_i$  and latitude  $b_i$ .  $B$  denotes the background probability density obtained from the exposure of the observatory. Both distributions are combined using the signal fraction  $f$ . By comparing the test statistics  $t = \ln \mathcal{L} - \ln \mathcal{L}(f = 0)$  with the isotropic expectation, the significance of describing the arrival directions of the measured cosmic rays by the source model can be calculated.

It has been found that a model of selected star burst galaxies (SBG) fits the arrival directions of cosmic rays measured by the Pierre Auger observatory better than an isotropic distribution with a significance of  $4.0\sigma$ . The corresponding excess map with its maximum close to NGC4945 is shown in figure 3.4. A smaller excess is also visible at the sources M83 and NGC253. Comparisons to alternative catalogs taking i.e. selected AGN sources into account yield significances in the range  $2.7\sigma - 3.2\sigma$  [5, 86].

In this analysis the threshold energy above which events were taken into account was scanned, see figure 3.5. Here the two source models are shown additionally combined with two composition scenarios motivated by measurements, for more details see [87]. The SBG scenario outperforms the other models and has its maximum at a threshold energy of 39 EeV. It is interesting to note that this analysis does not incorporate deflections in galactic magnetic field but however 9.7% of the measured cosmic rays can be explained by the SBG scenario smeared by  $12.9^\circ$ .

Cosmic rays are also used in the context of the emerging area of multi-messenger observations of different objects. In an observation of the binary neutron star mer-

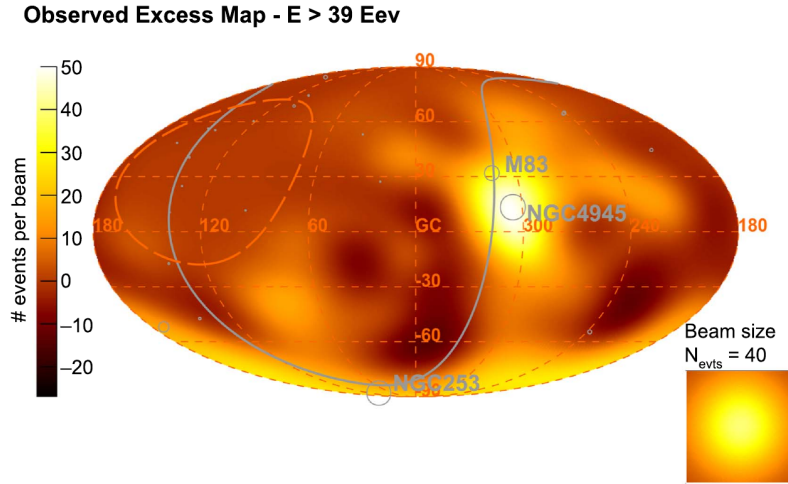


Figure 3.4: Observed excess map of cosmic rays with energies  $E \geq 39$  EeV, taken from [5].

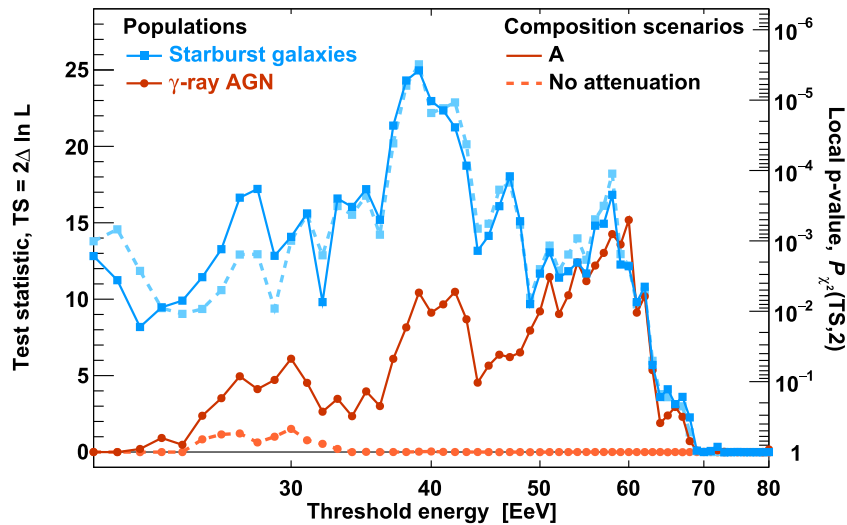


Figure 3.5: Test statistic of the comparison to different source candidates as a function of the threshold energy, taken from [5]. The source models are a selection of starburst galaxies and  $\gamma$  active galactic nuclei. Furthermore, two composition scenarios are displayed.

ger first detected through gravitational waves by the LIGO and VIRGO collaborations, the Pierre Auger collaboration and others looked for neutrino events [88, 89]. However, no candidates were detected which is consistent with model predictions. There were also no indications found for correlations of cosmic rays with neutrino events [90].

### 3.3 Composition

The study of the composition of cosmic rays plays an increasingly important role in astro-particle physics. It is typically investigated using the  $X_{\max}$  observable which is

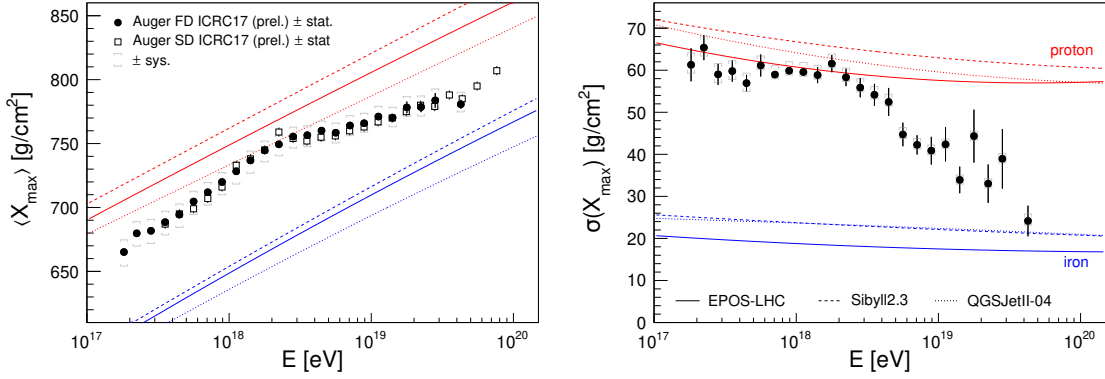


Figure 3.6: Measurement of the average depth of shower maximum  $\langle X_{\max} \rangle$  and standard deviation  $\sigma(X_{\max})$  by the Pierre Auger Observatory, taken from [91].

sensitive to the mass of the primary particle via a logarithmic dependency, see also section 2.1. Figure 3.6 shows the measurement of the mean and standard deviation of the shower depth as a function of energy. The red (blue) lines are predictions for protons (iron nuclei) using different interaction models. Both the mean and the spread of the  $X_{\max}$  distribution suggest a progressively heavier mass composition with energy as the distributions converge towards the iron predictions. The round data points contain the direct measurement of the maximum of shower depth via the fluorescence detector (FD) of the Pierre Auger observatory. For comparison, additional data points are shown in the left figure that use a method that determines  $X_{\max}$  using the rise-time of the signal in the surface detectors (SD) [92, 93]. This distribution has been cross-calibrated with the FD measurements. There are also more advanced methods allowing to reconstruct the shower depth from SD [94, 95], some of them even using novel deep learning techniques [96]. However, they require new reconstruction algorithms and can not be applied on top of the current and well tested methods.

Figure 3.7 presents the conversion of  $X_{\max}$  data to the mean mass numbers for different reconstructions. The direct measurement via the FD is displayed in blue and the measurement via the reconstruction from SD for both the full and the infill array in red. Additionally, the conversion of the maximum of the muonic component  $X_{\max}^{\mu}$  to a mass number is shown in green. Here, a huge gap to the other measurements is visible which can be explained by the muon deficit in simulations, see also section 2.1. Note that in contrast to figure 3.6 the cross-calibration between the SD and the FD measurements is omitted to show the differences. All measurements show the same trend towards a heavier composition at the highest energies. However, the conversions using EPOS-LHC yield a much heavier composition. Note that both models have been tuned at a center of mass energy of 13 TeV and have to extrapolate to the highest energies leading to a multiplication of uncertainties, see also section 2.1.

In contrast to the interpretation of the measurements by the Pierre Auger collaboration, the Telescope Array (TA) collaboration sees a compatibility with a proton dominated composition. The comparisons between both experiments are difficult because the Pierre Auger collaboration unfolds their detector resolution whereas TA

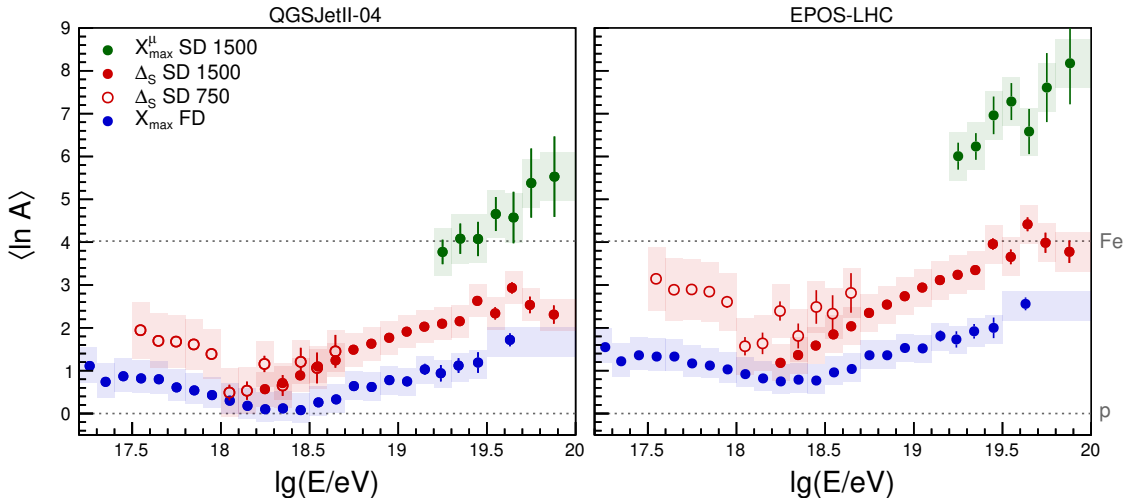


Figure 3.7: Average logarithm of the mass number obtained from using the (left) QGSJETII-04 [22] and (right) EPOS-LHC [19] hadronic interaction models, taken from [91], see also [97]. The blue markers denote the direct measurements from FD, the green circles the muonic component of the shower  $X_{\max}^{\mu}$  and the red markers the reconstruction based on the signal rise-time. Here, it is distinguished between the standard SD array with 1500 m spacing and the low energy extension with 750 m spacing. The horizontal dashed lines correspond to protons ( $A = 1$ ) and iron nuclei ( $A = 56$ ).

data is biased by detector resolution and reconstruction effects which on contrast maximizes the number of events [98]. However, a comparison is performed in the range  $18.2 \leq \log_{10}(E/eV) \leq 19.0$  with the following method as the TA data set is statistically limited at higher energies. First, an Auger-like  $X_{\max}$  distribution is obtained by simulating cosmic rays following a mixed composition fitted to the Auger measurements. In a next step the events are run through the TA analysis framework which especially includes detector efficiency and acceptance. This allows for a comparison to the published distribution by TA. Good agreement between both  $X_{\max}$  distributions is found using two complementary statistical tests, the Anderson-Darling [99] and the Kolmogorov-Smirnov [100, 101] test which are sensitive to the tail and the peak respectively.

In the region around the ankle at  $18.5 \leq \log_{10}(E/eV) \leq 19.0$  the data can be explained by a mixed composition including nuclei with mass numbers  $A > 4$  [77]. This is also visible in figure 3.8 where a four component model was fitted in 24 energy bins to the measured  $X_{\max}$  distribution.

$$G(X_{\max}; E_k) = \sum_{i \in \{p, \text{He}, \text{N}, \text{Fe}\}} w_i \cdot g(X_{\max}; A_i, E_k) \quad (3.2)$$

The method uses simulation templates  $g(X_{\max}; A_i, E_k)$  describing the  $X_{\max}$  distribution for each mass number  $A_i$  and energy bin center  $E_k$ . The factors  $w_i$  correspond to their relative abundance. Alternative approaches that incorporate the Gumbel distribution [103], which has been parameterized to describe the  $X_{\max}$  distribution

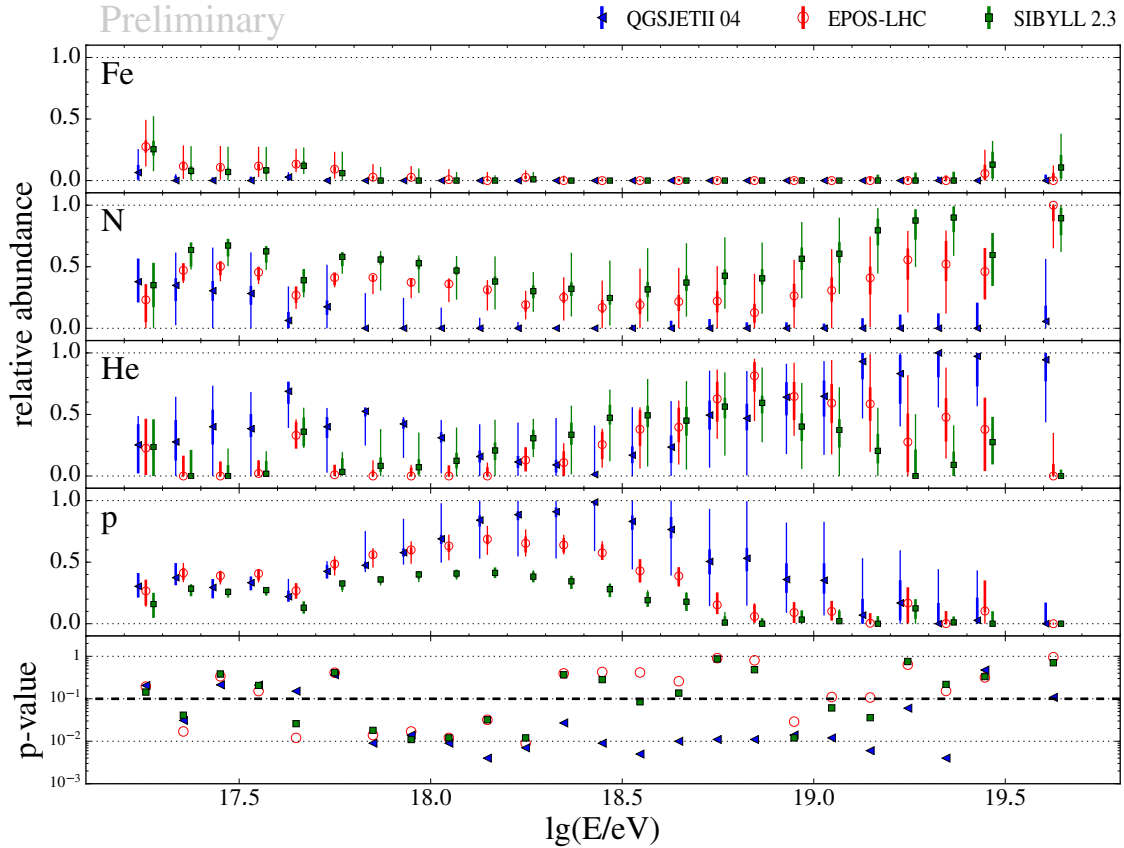


Figure 3.8: Energy dependent fit of four mass groups to the  $X_{\max}$  distribution. For details refer to the text, taken from [91], see also [102].

analytically, yield similar results. For  $17.5 \leq \log_{10}(E/\text{eV}) \leq 18.5$  and all interaction models the proton component is increased. For higher energies, helium and nitrogen dominate the mass composition, but here, the differences between the interaction models are too large to draw a conclusion if at an energy range of approximately  $18.5 \leq \log_{10}(E/\text{eV}) \leq 19.5$  helium and at higher energies nitrogen nuclei have the highest contribution as predicted by acceleration models for UHECRs. However, all models agree that the iron contribution is negligible in most of the energy bins.

### 3.4 Constraining Source Properties

Combining the measurements of the energy spectrum and the composition with an astrophysical model describing the sources of UHECRs allows to constrain the properties of the sources [87, 104, 105]. Common source models have parameters describing the mass composition at the source and additional parameters for the energy spectrum, typically a cutoff rigidity  $R_{\text{cut}}$  and spectral index  $\gamma$  describing a power law  $dN/dE \propto E^{-\gamma}$  for energies below the cutoff. The usage of a cutoff rigidity models that cosmic rays with higher charges can reach higher energies than particles with a lower charge. Thus, it assumes that the acceleration process is related to the

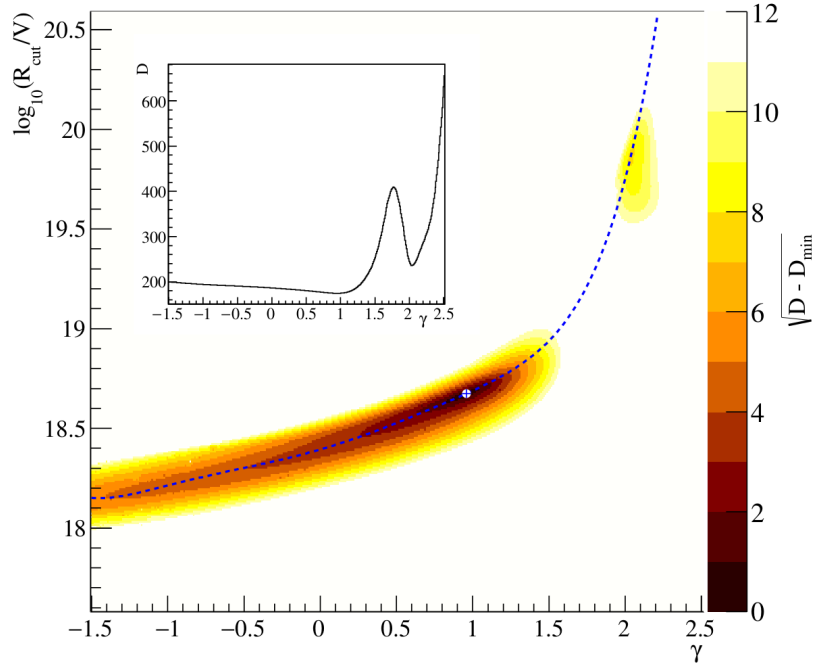


Figure 3.9: Cutoff rigidity and spectral index at the source, taken from [87]. The axes show the source spectral index  $\gamma$  and the cutoff rigidity  $\log_{10}(R_{\text{cut}}/V)$ . The colorbar displays the deviance, a statistical measure similar to a likelihood which is minimized during the fitting process. The blue line indicates a minimum valley and the inlay the distribution of  $\gamma$  along this line.

charge of UHECRs. Furthermore, propagation effects, e.g. decays, are taken into account in the fit.

Figure 3.9 shows the fit results for the energy spectrum of the sources. With the best fit value for the spectral index  $\gamma \approx 1$  the measured spectrum is steeper than the best fit injected spectrum at the sources. The inlay denoting the value of  $\gamma$  along the minimum valley makes this even more clear. Values  $\gamma > 1.5$  are strongly excluded whereas smaller values corresponding to a flatter or even increasing spectrum, which is theoretically challenging, can not be excluded. Consequently, propagation effects are important for the detection of sources. However, the best fit values for the masses at the sources show a dominating contribution of helium and nitrogen and only small fractions of lighter and heavier elements.



# 4. Origin and Propagation

Since the discovery of cosmic rays around 100 years ago, their origin, especially of those with ultra-high energies, has been one of the major puzzles in astroparticle physics. A further central question is whether the end of the spectrum (see section 3.1) occurs due to a lack of ability of the sources to accelerate cosmic rays to higher energies or because of dominant energy losses during the propagation.

This chapter is structured as followed: Different acceleration mechanisms and possible sites are highlighted in section 4.1 whereas the propagation in the inter- and extragalactic space is presented with a focus on interactions with photon background fields in section 4.2.

## 4.1 Acceleration Models and Source Candidates

The acceleration models of cosmic rays can be subdivided into two different approaches: For the top-down models, the decay of super-massive or super energetic particles into ultra-high energy cosmic rays (UHECRs) is considered. The idea behind these models is similar to the radioactive decay of a particle as measured in nuclear physics, just at increased energy. Typical examples for these theories are super-heavy dark matter [106, 107, 108], topological defects [109] and the Z-bursts model [110, 111]. However, these models all predict either a high photon or neutrino flux and are disfavored because neither effect has been observed [112, 113, 114, 115, 116, 117].

In the bottom-up models on the other hand an external mechanism accelerates particles from low to ultra-high energies. Here, one can distinguish between models using electric fields, so called “one-shot”, and stochastic models. In the first case the electric fields are created by changing magnetic fields [118], e.g.  $B \sim \mathcal{O}(\text{kG})$  [119]. Afterwards, the acceleration is comparable to the acceleration of charged particles in a capacitor. These models typically fail to explain the energy spectrum of cosmic rays, see section 3.1. Furthermore, a high energy density is required for the acceleration, but this also strongly increases the cross section of different energy loss processes [120, 121].

A stochastic mechanism where charged particles are accelerated by repeated deflections in magnetic clouds was initially proposed by Fermi [122]. Here, the particles gain energy on average when scattering at irregularities of the magnetic field of a partly ionized cloud. For ultra-relativistic particles and speeds of the cloud  $\beta \ll 1$  the average energy gain is  $\frac{\langle \Delta E \rangle}{E} \simeq \frac{4}{3} \beta^2$ . Note, in this so called second-order Fermi

acceleration, it is assumed that the directions of the accelerations are isotropically distributed for many scattering processes. In contrast, an acceleration in a preferred direction as in shocks leads to a linear dependency  $\frac{\langle \Delta E \rangle}{E} \simeq \frac{4}{3}\beta$  [123, 124, 125]. Consequently, this process is called first-order Fermi acceleration as the energy gain is linear in  $\beta$ .

For both models the energy of the particles after  $m$  encounters is  $E_m = (1 - \xi)^m \cdot E_0$  where  $E_0$  is the initial energy and  $\xi = \frac{\langle \Delta E \rangle}{E}$  the average relative energy gain. If  $p_{\text{esc}}$  is the probability of a particle to escape the shock region, the number of particles with energy greater  $E_m$  is

$$N(E > E_m) = N_0 \cdot \sum_{i=m}^{\infty} (1 - p_{\text{esc}})^i \propto \left( \frac{E_m}{E_0} \right)^{\gamma}. \quad (4.1)$$

Here,  $N_0$  is the initial number of particles and  $\gamma$  is given by

$$\gamma = \frac{\ln(1/(1 - p_{\text{esc}}))}{\ln(1 + \xi)} \approx \frac{p_{\text{esc}}}{\xi}. \quad (4.2)$$

Thus, the stochastic acceleration process naturally leads to a power law energy spectrum. For a detailed calculation of different properties in the Fermi acceleration process see [126].

However, the Fermi acceleration processes also have some limitations. Long acceleration times are required as typical speeds of the magnetic regions are in the order of  $\mathcal{O}(10 \text{ km s}^{-1})$  leading to a relative energy gain of  $\xi \sim 10^{-8}$ . Under the assumption that the acceleration region has a size of a few parsec, a particle scatters approximately once a year with a magnetic region. The second limitation is related to the injection of particles as they already must have a high initial energy to not being slowed down by the magnetic clouds. Thus a second mechanism is required to achieve an initial acceleration.

For the Fermi mechanisms the maximum achievable energy  $E_{\text{max}}$  is proportional to the size  $R$  of the region, its magnetic field strength  $B$ , the shock speed  $\beta$  and the charge of the particle  $Ze$ . This upper limit is naturally given by the Larmor radius of the accelerated particles in the magnetic field, see equation (4.3).

$$E_{\text{max}} \approx \beta c \cdot B \cdot R \cdot Ze \quad (4.3)$$

Figure 4.1 shows the magnetic field strengths and sizes of different source candidate objects including their uncertainties. It was originally created by Hillas in 1984 to summarize the knowledge about different acceleration sites [127]. Two diagonal lines show the required magnitudes of the magnetic field strength or size of region to accelerate particles up to the highest energies. As our galaxy has a radius in the order 20 pc and the magnetic field strength in the arms is in the order of  $\mu\text{G}$ , cosmic rays at the highest energies most likely originate from outside our galaxy. Only a few regions are around or above the lines and can be considered candidates.

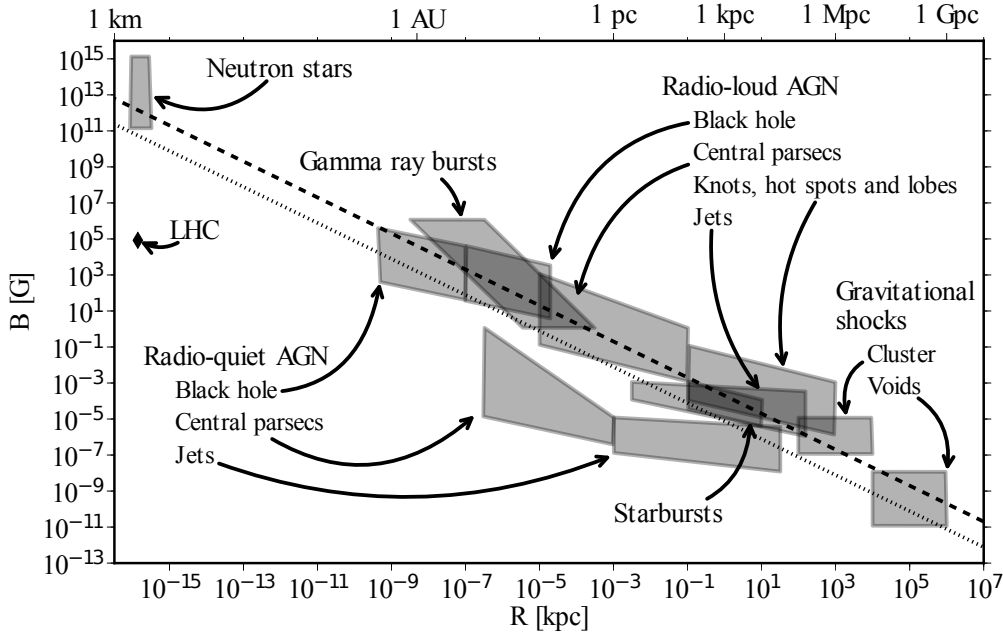


Figure 4.1: Hillas diagram showing the relation between the magnetic field strength and the radial size of possible UHECR sources including their uncertainties, originally from [127], modified from [128]. Above the dashed (dotted) line protons (iron nuclei) can be accelerated to  $10^{20}$  eV according to equation (4.3).

- Active galactic nuclei (AGN)** are among the brightest objects in the universe. In the center of an AGN there is a super-massive black hole attracting surrounding matter which builds an accretion disk. Most AGNs exhibit two highly relativistic jets perpendicular to the accretion disk. In figure 4.1 a distinction between radio-loud and quiet AGNs is made. The main difference in this classification is that radio-load AGNs produce large scale radio jets carrying a significant fraction of the luminosity whereas the emission in the jets for radio quiet AGNs is negligible. For more details see [129]. As UHECRs potentially can be accelerated close to the black hole, in the accretion disk and the jets of UHECRs, AGNs often discussed as source candidates. Correlation measurements between UHECRs arrival directions and catalogs, i.e. SWIFT BAT [130] and Veron-Cetty-Veron [131], have been carried out but did not yield significant results [132, 133, 134, 135].
- Neutron stars** have a size of a few km but exhibit very strong magnetic fields in the order of  $B \sim \mathcal{O}(10^{11} \div 10^{12} \text{ G})$  for normal neutron stars; magnetars can have even stronger fields up to  $10^{15} \text{ G}$  [136, 137, 138]. Some theoretical models for acceleration in magnetars predict accelerations up to  $10^{21} \text{ EeV}$  with an energy spectrum following  $E^{-2}$  [139]. Binary neutron stars have already been observed to be a source of gravitational waves [140, 88, 141], but no evidence for high energy neutrinos coincident with the merge of a binary neutron star

has been found [89]. This makes them unlikely as source candidates as neutrinos accompany the acceleration of cosmic rays but arrive earlier on Earth as they are not deflected in magnetic fields.

- **Gamma ray bursts (GRB)** are flashes of gamma-rays emitted in explosions in distant galaxies. Typically they last between few seconds up to a few minutes and emit energies up to  $50 \cdot 10^{43}$  J [142]. Their directions are observed to be uniformly distributed on the sky which potentially could explain the low anisotropy observed in the arrival directions of UHECRs [143]. However, as they are typically observed at redshifts  $z > 1$ , a high activity to explain the observed UHECRs is required, but not observed [144].
- **Starburst galaxies (SBG)** are galaxies with a large star formation rate. After an initial acceleration in the central part, a superwind driven by young stars and subsequent supernovae explosions could further accelerate cosmic rays [145, 146]. Two of the most prominent examples are M82 and NGC253 which were part of the SBG catalog that fits the data measured by the Pierre Auger Observatory better than a purely isotropic distribution with a statistical significance of  $4.0 \sigma$  [5].
- **Clusters of galaxies** can have magnetic field strengths in the range of a few tenth  $\mu\text{G}$  up to  $\sim 25 \mu\text{G}$  at scales up to 1 Mpc [147, 148]. Due to their large size, lower energetic particles are confined within the cluster whereas higher energetic particles can escape.

For a detailed review on the proposed acceleration processes at different sites see [149, 150, 151].

## 4.2 Propagation

After having gained enough energy to leave the acceleration region, cosmic rays are essentially influenced by two effects on their way through the universe. Firstly, they interact with the photon background fields, i.e. the cosmic microwave background (CMB) and secondly, they are deflected in magnetic fields. Sometimes, decays of unstable nuclei are considered as a third effect.

### Interaction with photon fields

The photon background fields range over more than 10 order of magnitude in energy, see figure 4.2. The interaction rate of a cosmic ray depends on the energy of the cosmic ray  $E_{\text{CR}}$ , the cross section  $\sigma(s)$  of the process and the differential energy density of the photon background  $dn/dE_\gamma$  [154]. First, the three most important parts of the spectrum are separately presented before explaining the physical interaction processes.

The **cosmic radio background (CRB)** at the lowest energies is believed to be created by extragalactic sources emitting radio emission below the current experimental limits [152, 155, 156]. Due to the dominant radio background in our Galaxy

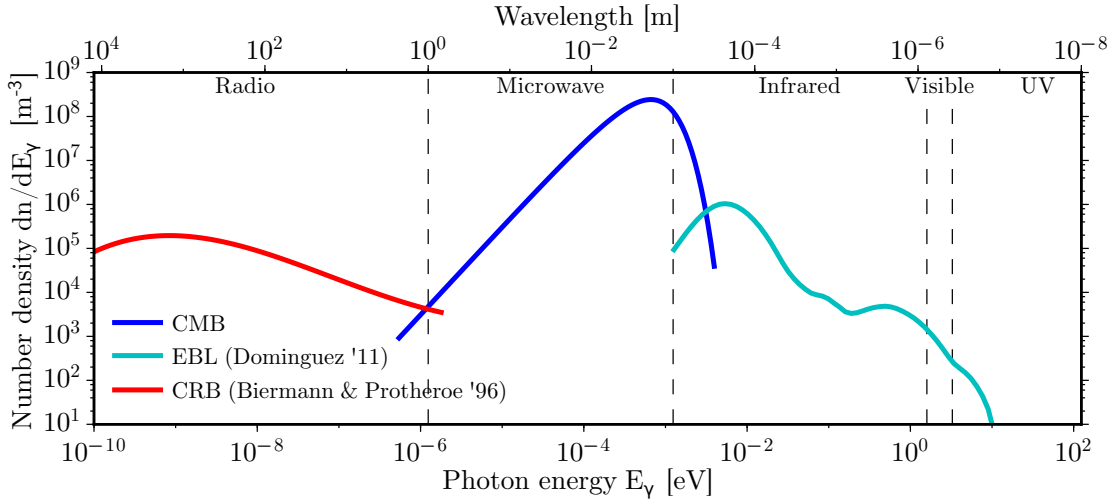


Figure 4.2: Spectrum of the photon background fields in the universe as a function of energy. On the top axis the wavelengths with typical classification names is shown. The models of the Cosmic Radio Background (CRB) [152] and the Extragalactic Background Light (EBL) [153] are shown in red and turquoise respectively. The blue curve shows the measured blackbody spectrum of the Cosmic Microwave Background (CMB). Figure modified from [104].

measurements are difficult, but most recent experimental results suggest a higher CRB density as in the models [157]. The interactions of cosmic rays with the CRB become only relevant at extremely high energies of the particles.

The **cosmic microwave background (CMB)** has the highest number density and its spectrum can almost perfectly be described by a blackbody spectrum at temperature  $T = 2.726$  K [15]. Its discovery by Penzias and Wilson in 1964 was honored with a Nobel prize in 1978 [158]. Today, it is considered as an important evidence for the Big Bang theory which can also explain its temperature by the expansion of the universe.

The **extragalactic background light (EBL)** is fueled by light from star formation processes and active galactic nuclei, so it strongly depends on cosmological evolution which makes modeling challenging [153, 159, 160, 161, 162]. A huge amount of the starlight is absorbed by dust in the universe and then re-emitted with a thermal spectrum visible at around  $10^{-2}$  eV. The second peak just below 1 eV can be explained by direct starlight.

The energy loss length is defined as propagation distance after which the cosmic ray has lost  $1/e \approx 37\%$  of its energy. It is shown for the three most relevant processes in figure 4.3.

**Electron pair production:** A photon  $\gamma_b$  of the background converts in the electromagnetic field of the charged cosmic ray into an electron positron pair leading to an energy loss of the initial cosmic ray:  $p + \gamma_b \rightarrow p + e^+ + e^-$ . This process has the

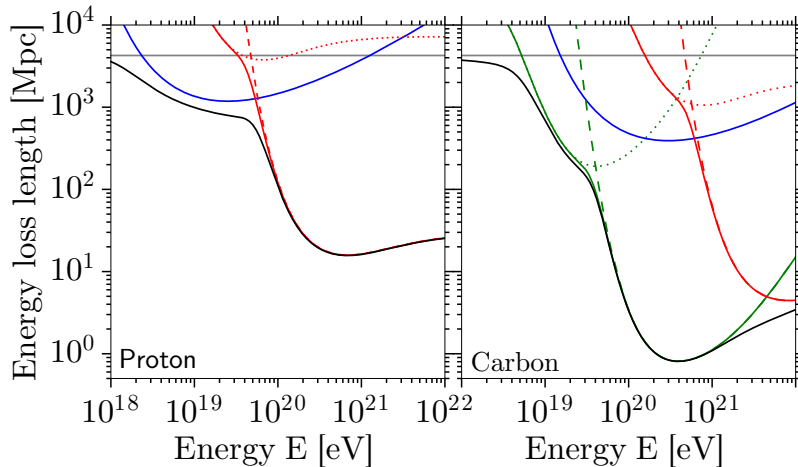


Figure 4.3: Energy loss length for protons and carbon nuclei. The pair production process is marked by the blue curve, photodisintegration in green and pion production in red. Dashed (dotted) lines show the contribution of the CMB (EBL). The horizontal line marks losses due to the expansion of the universe and the black curves denotes the combined energy loss length. Modified from [104].

lowest threshold of the three processes, and is thus the dominant process for protons at energies up to 100 EeV.

**Photodisintegration:** In an interaction with a background photon  $\gamma_b$ , a nucleus  $X_A^Z$  with mass number  $A$  and charge  $Z$  loses a proton:  $X_A^Z + \gamma_b \rightarrow X_{A-1}^{Z-1} + p$ . Photodisintegration is only relevant for nuclei where it is the most relevant process over the almost entire energy range.

**Production of hadrons:** In this reaction a proton is excited to a delta resonance which then further can decay, see equation (4.4). The decay probabilities for the intermediate states in equation (4.4) are  $\sim 66.6\%$  ( $\sim 33.3\%$ ) for the proton (neutron) channel. They can be calculated using the transition probabilities from quantum field theory. Note, the observed branching ratio of  $\Delta^+$  into a proton or neutron and a pion is  $BR(\Delta^+ \rightarrow N + \pi) \approx 100\%$  [15]. The neutron channel creates more particles which results in a slightly higher energy loss for an ultra-high energy proton.

$$p + \gamma_b \rightarrow \Delta^+ \rightarrow \begin{cases} p + \pi^0 & \longrightarrow p + 2\gamma \\ n + \pi^+ & \longrightarrow (p + e^- + \bar{\nu}_e) + (e^+ + \nu_e + \bar{\nu}_\mu) \end{cases} \quad (4.4)$$

The process becomes relevant for protons above a threshold energy of  $E_{\text{CR}} \sim 60$  EeV and can explain the cutoff of the energy spectrum. This so called GZK cutoff was proposed in 1966 by Greisen, Zatsepin and Kuzmin [163, 164] and was first observed by the HiRES collaboration [62] whereas the AGASA collaboration claimed that the energy spectrum continues without the GZK cutoff [165]. Meanwhile, the Pierre Auger and Telescope Array collaborations confirmed a further steepening with a significance larger than  $6\sigma$  [63, 166] consistent with the results of the HiRES collaboration.

Furthermore, the photo-pion production limits the maximum propagation distance of cosmic rays, see figure 4.4. Protons at the highest energies quickly lose energy on their propagation such that cosmic rays at the highest energies must originate from within  $\mathcal{O}(100 \text{ Mpc})$ . This limit is almost independent of the initial energy, as the cross section for the hadron production increases with energy. Thus, the mean energy loss is higher for a higher initial energy reducing the energy quicker than for a lower initial energy.

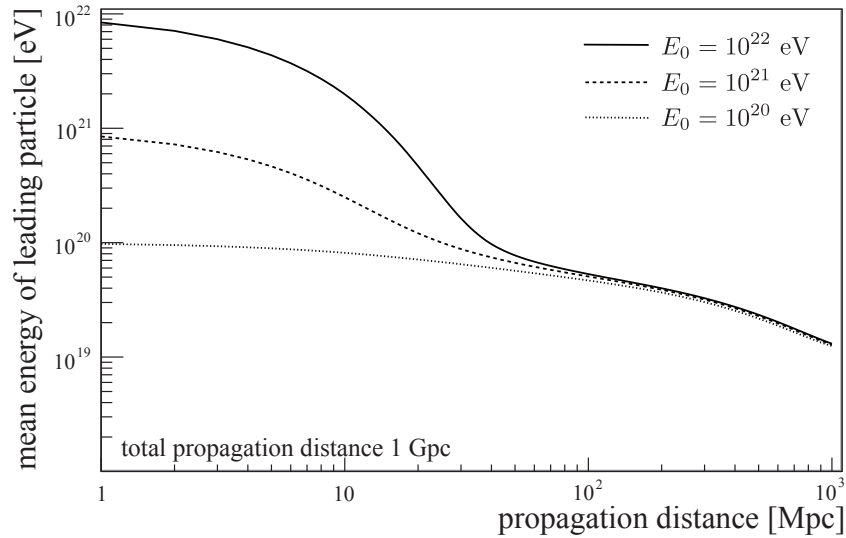


Figure 4.4: Propagation distance for protons with different initial energies, taken from [167].

### Deflection in extragalactic magnetic fields

*The following short summary is based on [168], for more details see also citations within this publication. My contribution to this study includes assistance in the strategic development of the analysis technology and the development of objectives based on my expertise on magnetic fields, which I acquired during my bachelor thesis and the journal publication “The nuclear window to the Extragalactic Universe” [169].*

Besides the interaction with photon background fields, cosmic rays are deflected in magnetic fields. Knowledge about extragalactic magnetic fields (EGMF) is dominated by theoretical models, as a direct measurement is not feasible and indirect measurements are dominated by the uncertainties of the galactic magnetic field (GMF). The simplest model of the EGMF is based on the assumption that the universe was unstructured at primordial times and consequently the magnetic fields were turbulent. This was first described mathematically by Kolmogorov [170]. Here, the magnetic field strength follows a wavenumber spectrum  $B \propto k^{-\alpha}$  limited by  $k_{\min} = \frac{2\pi}{L_{\max}}$  and  $k_{\max} = \frac{2\pi}{L_{\min}}$  with a minimal (maximal) coherence length  $L_{\min}$  ( $L_{\max}$ ). This leads to an effective coherence length where the magnetic field is constant:

$$L_c = \frac{L_{\max}}{2} \frac{\alpha - 1}{\alpha} \frac{1 - (L_{\min}/L_{\max})^\alpha}{1 - (L_{\min}/L_{\max})^{\alpha-1}} \quad (4.5)$$

In the case that the distance of a source to Earth is much greater than the coherence length ( $D \gg L_c$ ) the expected deflections can be described by equation (4.6) [171]. Note, simulations show that the deflection has the more the effect of a widening of a beam of cosmic rays than a directional deflection.

$$\beta = \beta_0 \cdot Z \cdot \sqrt{\frac{L_c}{\text{kpc}}} \cdot \sqrt{\frac{D}{\text{Mpc}}} \cdot \frac{\text{EeV}}{E} \cdot \frac{B}{\text{nG}} \quad (4.6)$$

The charge and energy of the cosmic rays are denoted by  $Z$  and  $E$  respectively. For the magnetic field strength  $B$  either the root mean square  $B_{\text{rms}}$  or the mean  $\bar{B}$  are used in literature. The normalization factor  $\beta_0$  has corresponding values in the range from  $0.2^\circ$  to  $1.2^\circ$  [172, 173, 174].

The deflections of cosmic rays coming from the five closest star burst galaxies with distances between  $D = 2.7 \text{ Mpc}$  for NGC253 and  $D = 17.9 \text{ Mpc}$  for NGC1068 were simulated in a study using the propagation software CRPropa3 [175]. In median we found a compatible value  $\tilde{\beta}_0 = 0.82^\circ$ . Furthermore, the scattering strength of the EGMF was estimated for a medium heavy composition of  $Z \approx 6$  to be  $\lesssim 2^\circ$  [168].

More complex models of the EGMF use large scale structure formation simulations, leading to a structured field where the local universe is mapped well, as close-by galaxies like Centaurus A are located at the correct position [173, 176, 177]. For these models, the scattering strength for sources below 18 Mpc has been estimated to be even smaller than for the turbulent magnetic fields as cosmic rays propagate mainly through voids with a weak magnetic field strength [168].

The galactic magnetic field (GMF) is better known as models can be tuned to Faraday rotation and polarized synchrotron radiation measurements. Due to their importance for this thesis, different models of the GMF and their impact on cosmic ray deflection are presented in detail in the next chapter 5.

## 5. Deflections in Galactic Magnetic Fields

*The content of this chapter has been prepublished in “The nuclear window to the extragalactic universe” [169]. My contribution to this journal publication includes the strategic development of the analysis technique to study various effects on cosmic rays from the galactic magnetic field, the execution of all partial analyses and the provision of all figures. In the context of this thesis every figure has been reproduced by an independent code implementation. Furthermore, all figures using the galactic magnetic field model of Pshirkov and Tinyakov (PT11) were extended to use both variants, the axialsymmetric and the bisymmetric spiral field (PT11-ASS and PT11-BSS) as the implementation in CRPropa3 [175] contained an incorrect definition of the coordinate system leading to a wrong position of the Earth. The corrections are small overall and do not change the fundamental physics messages. Corresponding text passages describing the PT11 field models have been adopted in this thesis. Additionally, some sentences were rephrased from writing in the “we-form” to a passive sentence structure, e.g. from “we define rigidity” to “rigidity is defined”.*

The origin of cosmic rays still remains an unanswered fundamental research question. Deflections of the charged particles in magnetic field make the search for the sources more difficult. For ultra-high energy cosmic rays, deflections in magnetic fields should diminish with increasing energy, such that directional correlations should lead to a straight-forward identification of accelerating sites. However, even at the highest energies the arrival distributions of cosmic rays appear to be rather isotropic. Only hints for departures from isotropic distributions have been reported, e.g., a so-called hot spot [85], and a dipole signal [135]. At least with the apparent isotropy, limits on the density of extragalactic sources were derived which depend on the cosmic ray energy [178].

A recent determination of ultra-high energy cosmic ray composition from measurements of the shower depth in the atmosphere revealed contributions of heavy nuclei above  $\sim 5$  EeV [97, 102]. This observation may explain the seemingly isotropic arrival distribution as deflections of nuclei in magnetic fields scale with their nuclear charges  $Z$ .

Obviously, when searching for cosmic ray sources, a key role is therefore attributed to magnetic fields. The galactic field in particular is strong enough to displace original arrival directions of protons with energy  $E = 60$  EeV by several degrees from their original arrival directions outside the galaxy [179]. The displacement angles for nuclei

even reach tens of degrees [180]. The knowledge on the extragalactic magnetic fields is much less certain, but is likely to be less important than the galactic field [181] and is not studied in this contribution.

To identify sources of cosmic rays, rather precise corrections for the propagation within the galactic field are needed which in turn can be used to constrain the field [182]. Beyond this, effects of lensing caused by the galactic field have been studied which influence the visibility of sources and the number of images appearing from a single source [183]. The influence of turbulent contributions to the galactic field has also been studied in the context of lensing [184] and nuclear deflections [185].

In previous directional correlation analyses of measured cosmic rays, only the overall magnitude of deflections was taken into account, e.g. [90], or corrections for cosmic ray deflections were applied using analytic magnetic field expressions reflecting the spiral structure of our galaxy [186].

Recently, parameterizations of the galactic magnetic field have been developed which are based on numerous measurements of Faraday rotation [79, 187], and in addition polarized synchrotron radiation for the second reference. Based on directional characteristics and the field strength of the parameterizations, deflections of cosmic rays are predicted to depend strongly on their arrival direction, charge and energy. In the following it is referred to the regular field with the bisymmetric (antisymmetric) disk model of the first reference as the PT11-BSS (PT11-ASS) field parameterization, and to the regular field of the latter as the JF12 field parameterization, respectively. Note, the wording PT11 means both parameterizations.

Angular distributions of cosmic rays in these galactic field parameterizations have been studied before, e.g., with respect to general properties of the JF12 parameterization [188], specific source candidates [189], general properties of deflections and magnifications [190, 191], and to the potential of revealing correlations between cosmic rays and their sources [192].

In this work it is investigated whether cosmic ray deflections in the galactic magnetic field can be reliably corrected for, given the current knowledge of the field. To simplify discussions of energy and nuclear dependencies, rigidity is defined as the ratio of the cosmic ray energy and number  $Z$  of elementary charges  $e$

$$R = \frac{E}{Z e} . \quad (5.1)$$

In these investigations galactic coordinates are used as reference system, with longitude  $l$  and latitude  $b$ . For a number of visualizations Cartesian coordinates are used alternatively with height  $z$  above the galactic plane, with the Earth being located at  $(x_E, y_E, z_E) = (-8.5, 0, 0)$  kpc.

Based on the two field parameterizations PT11 and JF12, key distributions of cosmic ray deflection, dispersion effects in arrival distributions, directional variance in field transparency, and the influence of random field components are discussed. From the rigidity dependencies of these distributions, a minimum rigidity threshold is recommended above which cosmic ray deflection may be controlled in terms of probability distributions.

Furthermore, the different results of the two galactic field parameterizations are taken as a measure of the current knowledge of the galactic field. Their cosmic ray angular deflections are compared and differences in the dispersion of arrival distributions studied. Finally, the practical consequences of galactic field corrections and their uncertainties are studied by performing simulated point source searches and by quantifying the field impact in terms of discovery potential.

## 5.1 Field Parameterizations

The two field parameterizations PT11 and JF12 each follow a different ansatz. Both take into account about 40,000 Faraday rotation measurements. The PT11 field has been fitted to two large sets of Faraday rotation measurements. The JF12 field has been adapted to several large sets of Faraday rotation measurements and to synchrotron polarization measurements, thereby increasing the information per analysed direction by two additional complementary measurements [190]. Both use the electron density model NE2001 [193] with an enlarged vertical scale for weighting the line-of-sight integrals of the magnetic field.

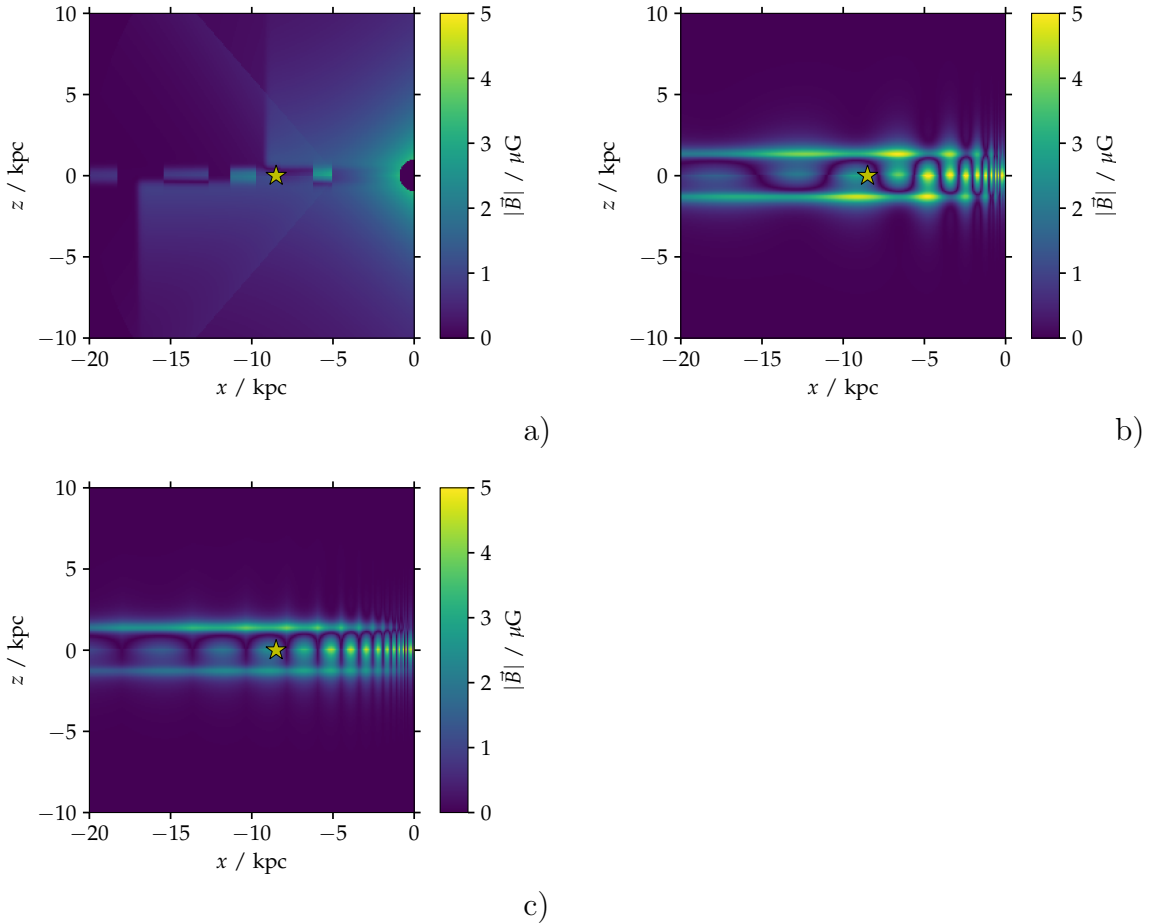


Figure 5.1: Strength of the galactic magnetic field as a function of the distance from the galactic center along the solar system line-of-sight, and of the distance perpendicular to the galactic plane for a) JF12, b) PT11-BSS and c) PT11-ASS. The yellow star denotes our solar environment.

Figure 5.1 shows the field strength as a function of the radial distance from the galactic center along the solar system line-of-sight and the distance perpendicular to the galactic plane. The fields exhibit different shapes and magnitudes; especially notable in figure 5.1a is the field extent of the JF12 parameterization above and below the galactic plane with non-negligible field strengths even at a distance of 10 kpc. The PT11 field (figures 5.1b and c), on the other hand, exhibits a rather concentrated halo field, which is centered around a distance of  $\sim 1.2$  kpc to the galactic plane.

When studying the magnitude of angular deflections of cosmic rays resulting from these parameterizations, the angle  $\beta$  between the incoming direction to the galaxy and the arrival direction on Earth is taken as a measure of the directional change (figure 5.2).

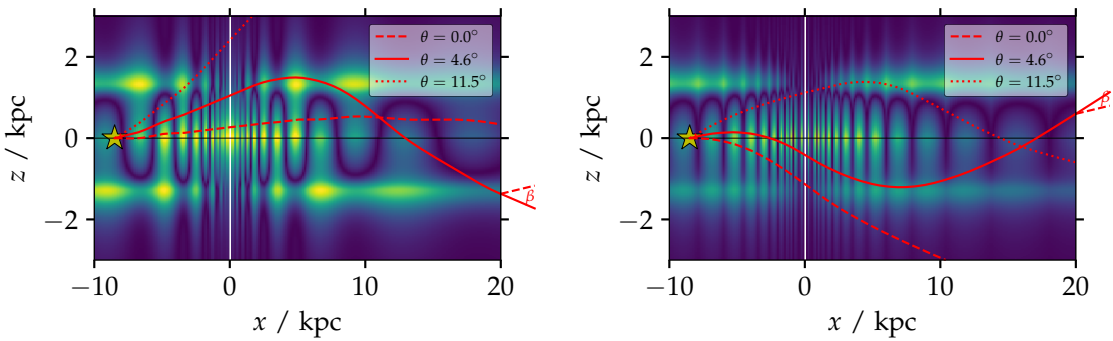


Figure 5.2: Example trajectories of antiprotons originating on Earth with different initial angular directions  $\Theta$  with respect to the galactic plane. The directional change  $\beta$  is defined as angle between the direction on Earth and the direction outside the galaxy. The magnetic field models in the background are left PT11-BSS and right PT11-ASS.

To get a first impression of the different deflections resulting from the two field parameterizations backward tracking techniques of antiprotons through the galactic field are used. With this technique individual trajectories for matter particles are obtained entering from outside the galaxy and then following the reverse path. The method ensures that every trajectory leads to observation on Earth.

In figure 5.3 the magnitudes of the angular deflections  $\beta$  of cosmic rays with rigidity  $R = 60$  EV are shown. The position in the map denotes the initial direction on Earth in galactic coordinates for the backtracked antiprotons. The color code refers to the magnitude of angular deflections which reach up to  $\beta = 28^\circ$ .

For the JF12 parameterization (figure 5.3a), deflections are largest near directions of the galactic center which is expected from the magnitude of the field shown in figure 5.1a. With the PT11 parameterization (figures 5.3b and c), deflections are largest in any direction near the galactic plane which is attributed to the strong disk field (figures 5.1b and c).

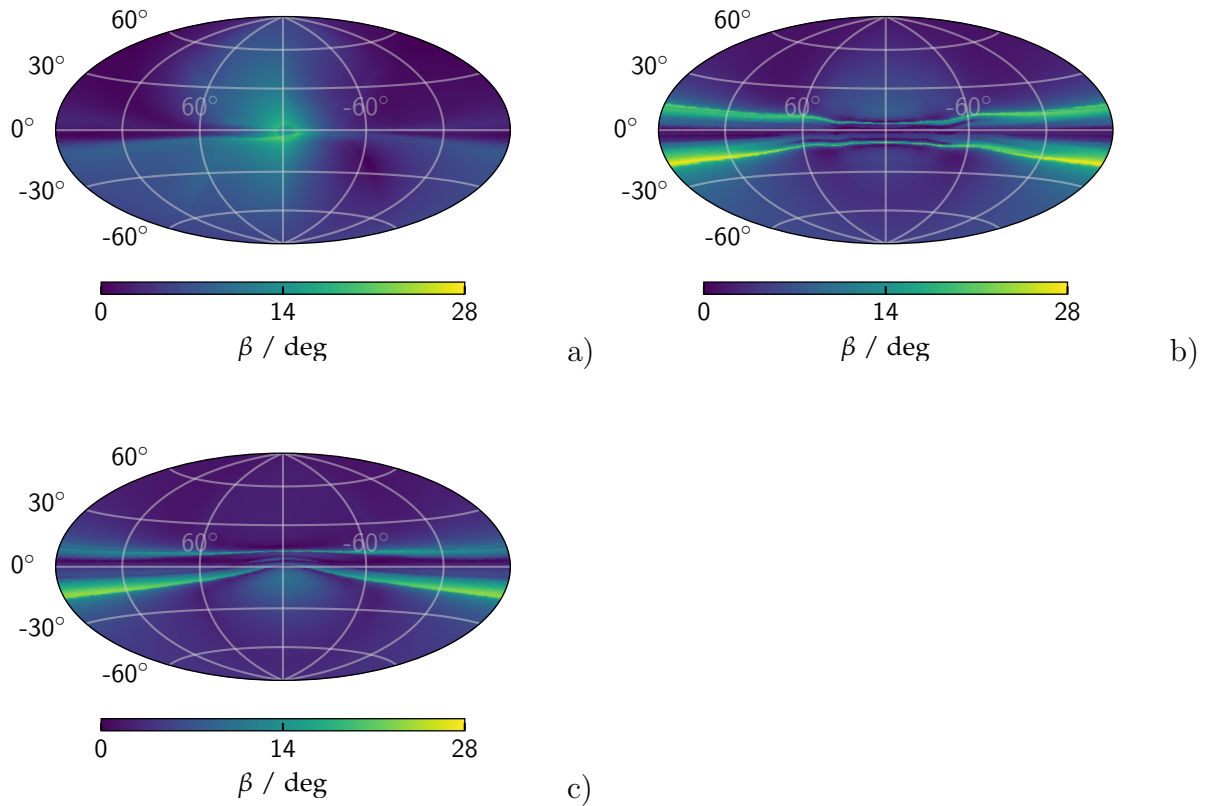


Figure 5.3: Magnitude of the angular deflections  $\beta$  in the galactic magnetic field for antimatter with rigidity  $R = 60$  EV starting from Earth in the direction presented in galactic coordinates, a) JF12, b) PT11-BSS and c) PT11-ASS.

As expected, the differences in the field parameterizations relate directly to a different impact on cosmic ray deflections. In the following section a number of aspects related to the directional changes of cosmic rays when traversing the galactic field are studied.

## 5.2 Impact of the Galactic Magnetic Field on Cosmic Ray Arrival

The goal of this section is to determine a kinematic regime where information on cosmic ray arrival directions can be obtained by transformation of probability distributions. For this purpose first cosmic ray angular deflections are analyzed as a function of rigidity. As primary criterion angular deflections are required to be below  $90^\circ$  in order to distinguish ballistic deflections from diffusive-type random walk.

Beyond this the dispersion of arrival probability distributions is investigated by the galactic field, and the splitting of arrival distributions into several images. Furthermore, directional dependencies of the field transparency for cosmic matter and antimatter particles are shown. The influence of random components of the field which imposes uncertainties on the arrival directions is also studied.

### 5.2.1 Deflection Angles

The two magnetic field parameterizations exhibit different field strengths above and below the galactic plane, and differ substantially in their field characteristics near the plane (figure 5.1). Therefore, the sky is divided into three regions of equal solid angles, and angular deflections are studied for each region separately. The boundaries of these regions are fixed at galactic latitudes of  $\pm 19.5^\circ$ .

To ensure that every cosmic ray trajectory leads to observation on Earth, the backward tracking method explained in the previous section is used. The term “northern region” is used to refer to antiparticles originating on Earth in the direction of positive latitudes above  $19.5^\circ$ . Negative latitudes below  $-19.5^\circ$ , on the other hand, are referred to as the “southern region”, while for latitudes in-between the term “disk region” is used.

In figure 5.4a the average directional change  $\langle\beta\rangle$  between the direction on Earth and the direction outside the galaxy is shown as a function of the cosmic ray rigidity  $R$  using the JF12 field. The distribution was derived from 5 million simulated cosmic rays per rigidity interval. In figure 5.4d the corresponding spread  $\sigma_\beta$  is displayed in terms of standard deviations. For low rigidities  $R \sim 0.1$  EV, cosmic ray confinement owing to the size of our galaxy and its magnetic field leads to large directional changes  $\langle\beta\rangle \sim 90^\circ$  and large average variations in  $\beta$  ( $\sigma_\beta \sim 40^\circ$ ).

At rigidity  $R = 6$  EV, the largest average deflection of  $\langle\beta\rangle \approx 50^\circ$  is found in the southern region (figure 5.4a, downward-pointing triangles). The corresponding spread amounts to  $\sigma_\beta \approx 15^\circ$  (figure 5.4d), such that for 95% of the cosmic rays the deflection angle remains below  $\beta = 90^\circ$ . The average deflection in the northern region is substantially smaller with only  $\langle\beta\rangle \approx 30^\circ$ , however, the spread of  $\sigma_\beta \approx 25^\circ$  is larger (upward-pointing triangles). Also here most of the cosmic ray deflections are below  $\beta = 90^\circ$ . A similar conclusion holds for the disk region (square symbols).

The PT11 parameterization exhibits very similar tendencies for rigidity  $R = 6$  EV as can be seen in figures 5.4b, c, e, f. In the disk region the deflections exceed those of the other regions for rigidities above  $R = 40$  EV (square symbols). Here the deflections also exceed that of the JF12 parameterization as already visualized in figure 5.3 above.

Overall, at rigidities  $R > 6$  EV the deflections are consistently reduced and correspondingly enhance the control over cosmic ray deflection. Therefore, in the following studies the rigidity of  $R = 6$  EV is used as a benchmark.

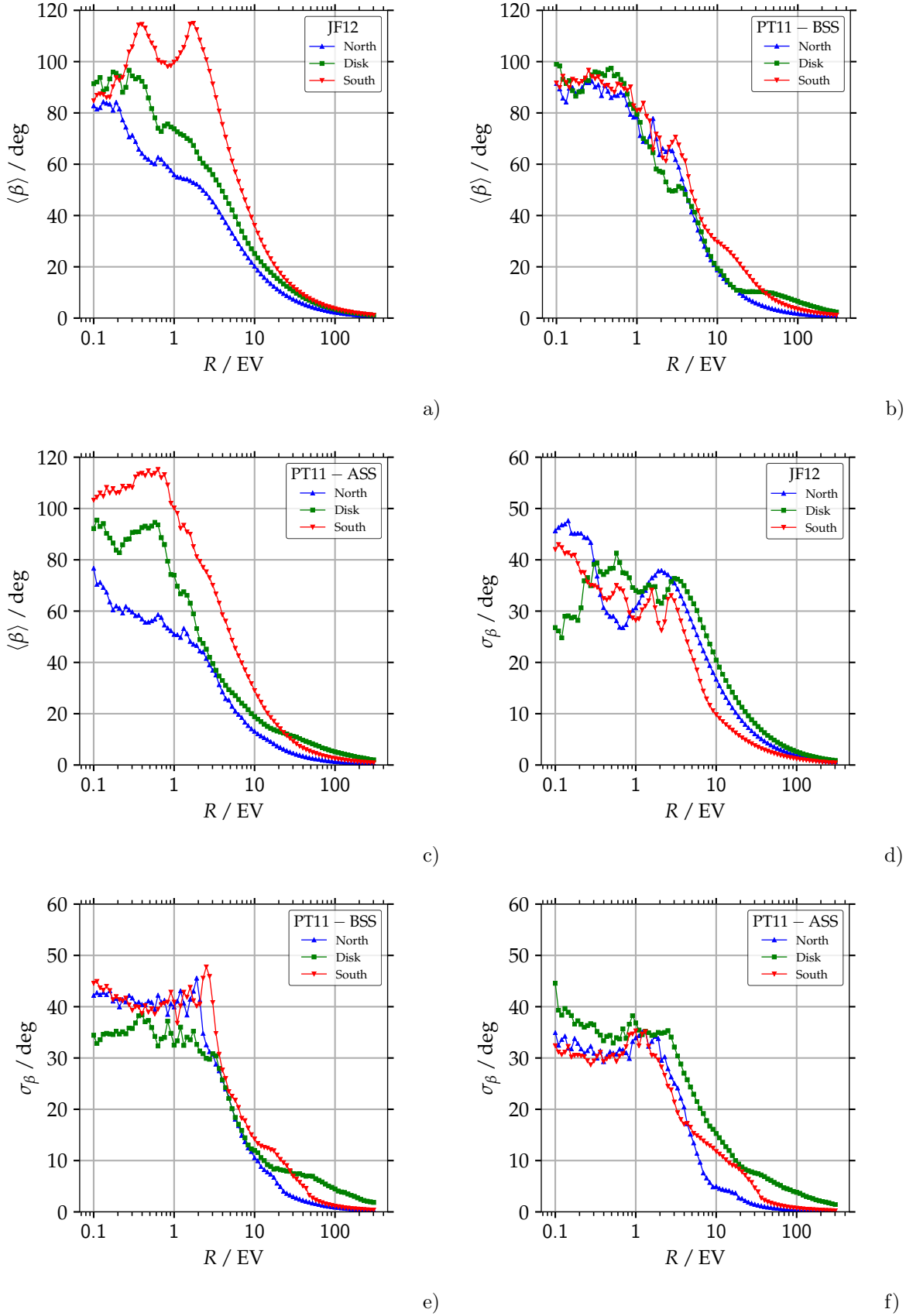


Figure 5.4: Average angular deflections  $\langle\beta\rangle$  in the galactic magnetic field for anti-matter originating on Earth in three regions separated by galactic latitudes  $\pm 19.5^\circ$  as a function of rigidity  $R$ , a) JF12, b) PT11-BSS, c) PT11-ASS. Spread  $\sigma_\beta$  of the angular deflections in terms of standard deviations, d) JF12, e) PT11-BSS, f) PT11-ASS.

## 5.2.2 Dispersion

Cosmic rays originating from a point source may arrive slightly dispersed after their propagation through extragalactic fields. When traversing the galactic field the extent of the arrival distribution may even be enlarged.

In order to obtain information on the arrival direction and arrival probability on Earth of a cosmic ray that enters the galaxy in any direction, a lensing technique is used [194, 195]. The lenses consist of matrices based on the HEALPix format [196], where the sphere is divided into  $N_{pix} = 49,152$  equally sized pixels of approximately  $1^\circ$  in size. For each rigidity interval a separate matrix is produced by backtracking a set of  $N_{pix} \times 100$  antiparticles, which are distributed uniformly in each pixel. The matrices thus contain the probability of a cosmic ray entering the galaxy with rigidity  $R$  at pixel direction  $(l_i, b_i)$  to be observed in pixel direction  $(l'_j, b'_j)$ . As defined above,  $l, l'$  refer to the galactic longitudes, and  $b, b'$  to the latitudes, respectively.

By design, the lenses project an extragalactic isotropic distribution onto an isotropic distribution on Earth. Note that some incoming directions have more simulated trajectories leading to observation on Earth, while other directions have less, such that there are directionally dependent variations in the transparency of the field. The lenses are normalized to ensure that the lenses return relative arrival probabilities, and that an isotropic cosmic ray flux is preserved. However, for cosmic rays arriving from individual sources the flux varies depending on the source directions which is shown below. The technical details of the lenses and their production are outlined in [128, 195]. The lenses used in this contribution were calculated with the CRPropa v3 program [175] using the PT11 and JF12 parameterizations.

In figure 5.5 examples of arrival directions on Earth are shown for simulated cosmic rays with rigidity  $R = 10$  EV together with their original source directions using the JF12 parameterization of the regular field. The incoming cosmic rays followed a Fisher probability distribution [197]  $f(\alpha, \kappa) = \kappa \exp(\kappa \cos \alpha) / (4\pi \sinh \kappa)$  with a

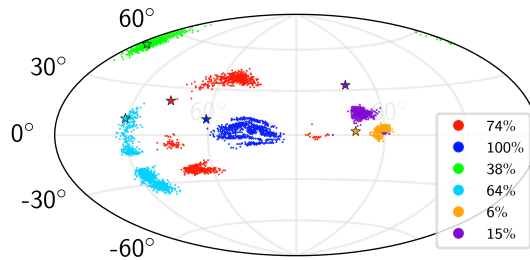


Figure 5.5: Arrival distributions for cosmic rays with rigidity  $R = 10$  EV originating from arbitrarily chosen sources (star symbols), and the relative arrival probability in percent. Relations of cosmic rays with their sources and corresponding arrival probabilities are indicated by the color code (JF12).

Gaussian width of  $\sigma = 1/\sqrt{\kappa} = 3^\circ$ . Their arrival directions were calculated with the lensing techniques described above. The color code indicates the relation between sources and their cosmic rays. For all scenarios, the fraction of arriving cosmic rays is shown on the right side of the figure, normalized to the source with the highest arrival probability.

Different images of the cosmic rays appear depending on their incoming direction. For example, a source direction which coincides on average with the cosmic rays after traversing the galactic field is denoted by the green symbols. Only a widening of the directional distribution is observed. Another example is a source direction where the cosmic ray distribution is displaced without a strong spread (purple symbols).

Examples of source directions where the cosmic rays are substantially deflected and exhibit a wide-spread distribution of arrival directions are denoted by the light blue and dark blue symbols. For some source directions, small variations in the cosmic ray incoming direction lead to largely different paths, and therefore to several distinct images of the arrival directions (red symbols).

To investigate dispersion effects in the galactic field, the initial cosmic rays are again chosen to follow a Fisher probability distribution with a Gaussian width of  $3^\circ$ . In principle this value could be related to dispersion effects caused by extragalactic fields, which implies a dependency on cosmic ray rigidity. However, to ensure clarity of the galactic field investigations, a fixed Gaussian spread is used for all cosmic rays incoming to our galaxy throughout this work.

After the cosmic rays traversed the galactic field, the direction and extent of the resulting arrival distribution are quantified by calculating around every HEALPix pixel  $(l'_j, b'_j)$  with non-zero probability a circular curve which includes 50% of all arrival probabilities. Then the radius  $r_{50}$  of the smallest circle is used as a measure of the extent of the probability distribution [198].

In figure 5.6 the extent of the arrival probability distributions is shown in terms of the smallest average radius  $\langle r_{50} \rangle$  as a function of cosmic ray rigidity  $R$ . Again the three galactic regions defined above are shown separately. As start with extragalactic directions the term “northern region” is used to refer to initial directions with galactic latitudes above  $19.5^\circ$ , etc.

The projection of the incoming distribution causes a dispersion or a focusing effect, depending on the original cosmic ray direction and its rigidity  $R$ . In the southern region (downward-pointing triangles) a focusing effect is visible for rigidities around  $R \sim 15$  EV. In contrast, the disk region (square symbols) exhibits dispersion effects up to the largest rigidities.

Below  $R = 1$  EV the average extent  $\langle r_{50} \rangle$  is large for both fields, such that it appears difficult to identify arrival directions on Earth from a given extragalactic direction. The JF12 field exhibits several pronounced features which appear to be specific to the JF12 field parameterization. Such effects are not visible in the PT11 parameterization where  $\langle r_{50} \rangle$  appears to increase continuously with reduced rigidity up to  $70^\circ$ .

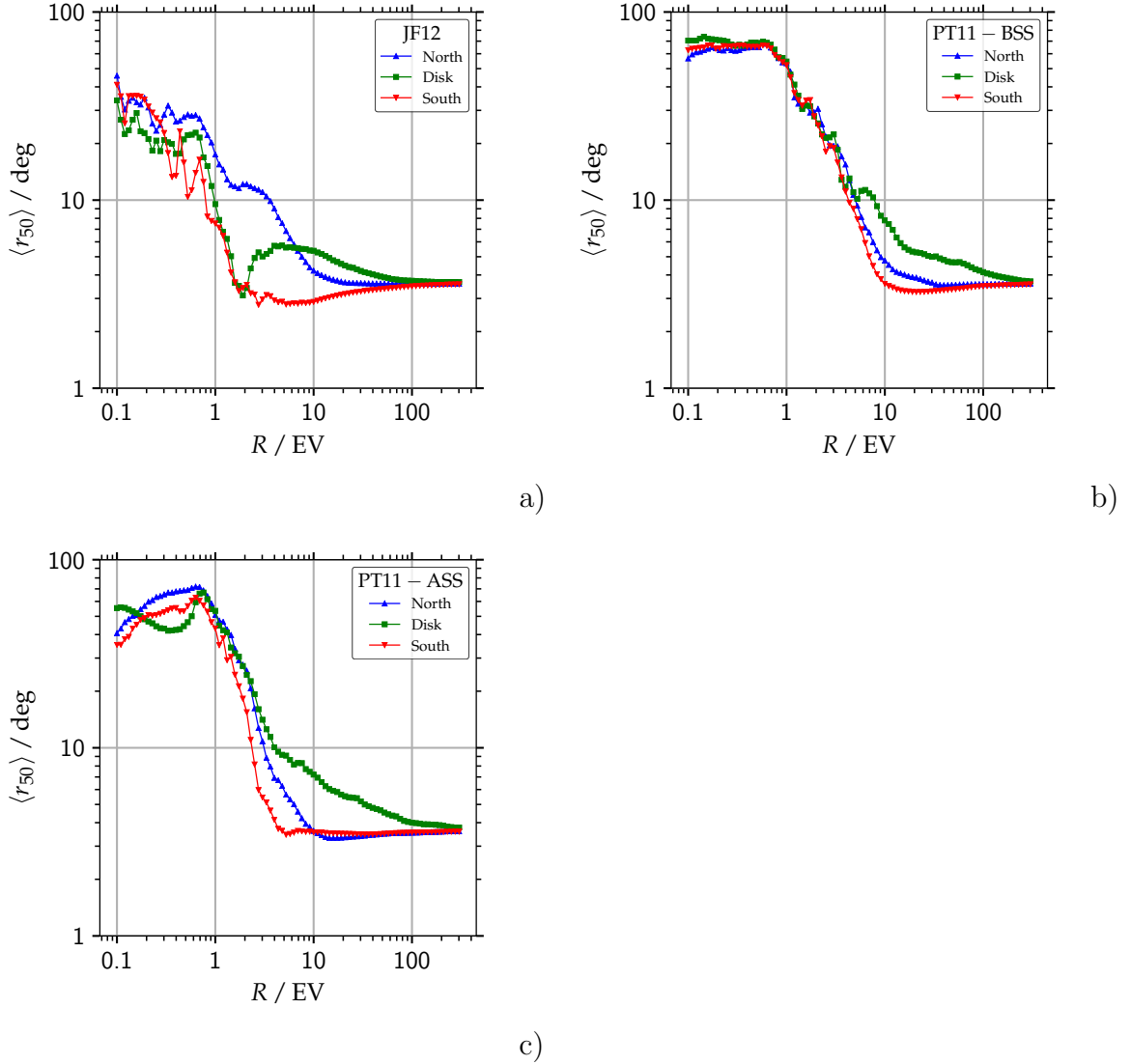


Figure 5.6: Average extent  $\langle r_{50} \rangle$  of arrival probability distributions on Earth resulting from cosmic rays incoming to our galaxy with a fixed Gaussian width of  $3^\circ$  in three regions separated by galactic latitudes  $\pm 19.5^\circ$  as a function of rigidity  $R$ , a) JF12, b) PT11-BSS and c) PT11-ASS. For the exact definition of  $r_{50}$  refer to the text.

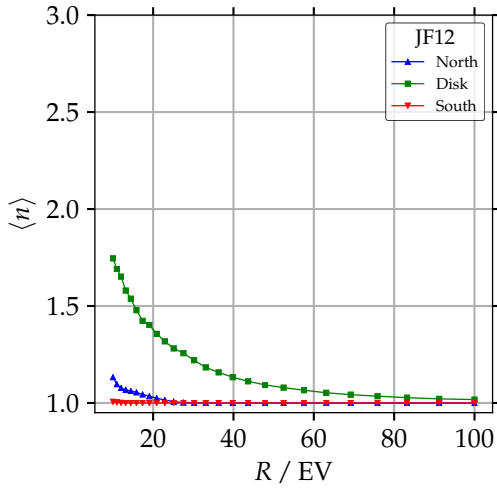
Above  $R = 6$  EV both parameterizations lead to similar results with a dispersion effect in the disk region (square symbols), and dispersion and focusing effects in the southern region (downward-pointing triangles). The largest extent of the probability region is found for the PT11 field corresponding to a dispersion of the initial probability distribution by a factor of 3 at  $R = 6$  EV, which may still be acceptable for an analysis of cosmic ray arrival directions.

### 5.2.3 Multiple Images

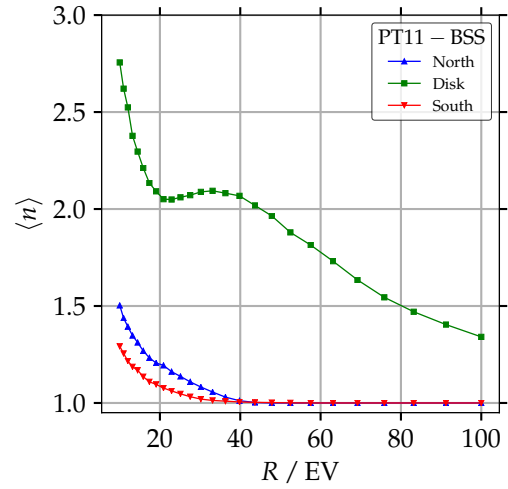
Extending the above study of dispersion, multiple images arising in cosmic ray arrival distributions on Earth are investigated. Again cosmic rays from an incoming

direction are Fisher-distributed with a Gaussian width of  $3^\circ$ . For some incoming directions, the small angular deviations within this distribution are sufficient to change the arrival direction on Earth substantially, leading to distinct maxima in the arrival distributions. Examples for such multiple images are denoted in figure 5.5 by the red symbols.

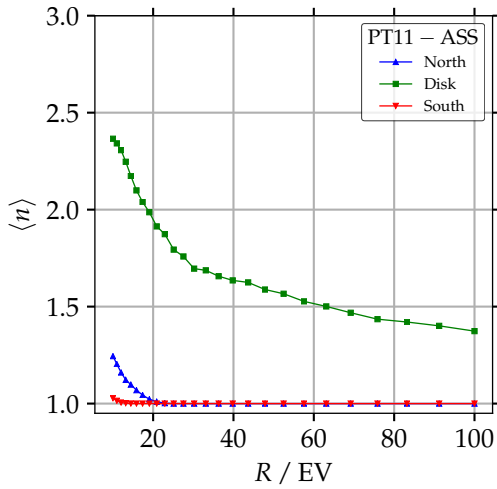
The number of arrival images is counted by searching for connected areas of arbitrary shape in-between which the probability falls below a pre-defined threshold. For this the HEALPix resolution in the arrival distribution is coarsened from originally  $1^\circ$  to  $4^\circ$  and require each pixel to carry at least 20% of the pixel with the maximum arrival



a)



b)



c)

Figure 5.7: Mean multiplicity  $\langle n \rangle$  of images in the arrival probability distributions on Earth resulting from cosmic rays incoming to our galaxy with a Gaussian width of  $3^\circ$  in three regions separated by galactic latitudes  $\pm 19.5^\circ$  as a function of rigidity  $R$ , a) JF12, b) PT11-BSS and c) PT11-ASS. For the image definition refer to the text.

probability. The image multiplicity then arises from counting connected areas that are separated from one another by at least one pixel below the pre-defined threshold.

In figure 5.7 the average multiplicity  $\langle n \rangle$  of arrival images is shown as a function of cosmic ray rigidity  $R$  in the three regions of the galactic sphere separated by galactic latitudes  $\pm 19.5^\circ$ . Overall, the image multiplicity decreases with increasing rigidity. The multiplicity arising from the PT11 parameterization (figures 5.7b and c) appears to exceed that of the JF12 parameterization (figure 5.7a).

For directions in the northern and southern regions, typically one image of the arrival direction arises. In the disk region, however, multiple images appear even for cosmic rays with large rigidity. Here the image multiplicity is especially large for the PT11 parameterization (figures 5.7b and c, square symbols) which is related to the pronounced halo field visualized in figure 5.1b.

Multiple images reduce the predictive power of cosmic ray arrival directions and may require additional selection depending on the individual analysis. As criteria to reduce image multiplicity both cosmic ray rigidity and a selection of incoming directions away from the galactic disk region are relevant.

## 5.2.4 Field Transparency

Related to the above study on dispersion, extragalactic directions causing a relatively enhanced flux of cosmic rays on Earth [194] and directions for which the arrival probability disappears as no simulated trajectory leads to Earth are investigated. These effects have a direct impact on the visibility of a source by cosmic ray messengers, and the luminosity required for observation on Earth. Examples of varying transparency of the field depending on the incoming directions are shown in figure 5.5.

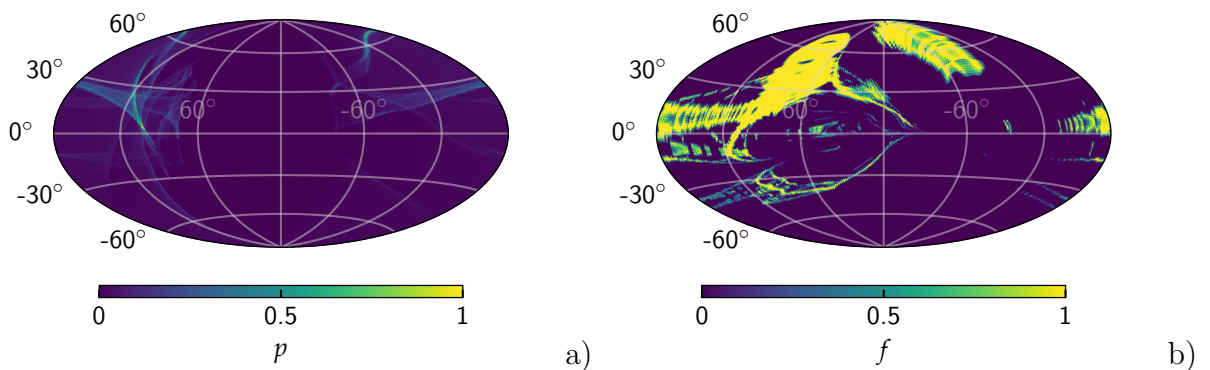


Figure 5.8: a) Probability  $p$  of observing a cosmic ray with rigidity  $R = 6$  EV on Earth as a function of the incoming direction to our galaxy (JF12). b) Flux  $f$  on Earth originating from the 1%-percentile of the directions with the largest arrival probabilities in figure a).

To demonstrate the enhanced flux of a few extragalactic directions, the probability  $p$  of arriving on Earth is shown coded in color in figure 5.8a for incoming cosmic rays with rigidity  $R = 6$  EV. The lightly colored regions indicate incoming cosmic ray directions with a high probability of observation on Earth.

In order to quantify the flux enhancement, the incoming directions are organized (binned in  $N_{pix} = 49,152$  pixels of  $1^\circ$ ) according to their arrival probabilities  $p_j$  on Earth and select the leading  $k$  directions. These incoming directions cover a solid angular region of  $\Omega = (k/N_{pix}) \cdot 4\pi$  and provide a relative flux contribution of  $F(k) = \sum_{j=1}^k p_j / \sum_{j=1}^{N_{pix}} p_j$ .

Figure 5.8b displays for the above example the observed flux  $f$  of cosmic rays originating from the 1% incoming directions with the highest probabilities indicated in figure 5.8a, when assuming an isotropic extragalactic flux. These few incoming directions cause a wide spread distribution and contribute  $F = 30\%$  to the observed flux.

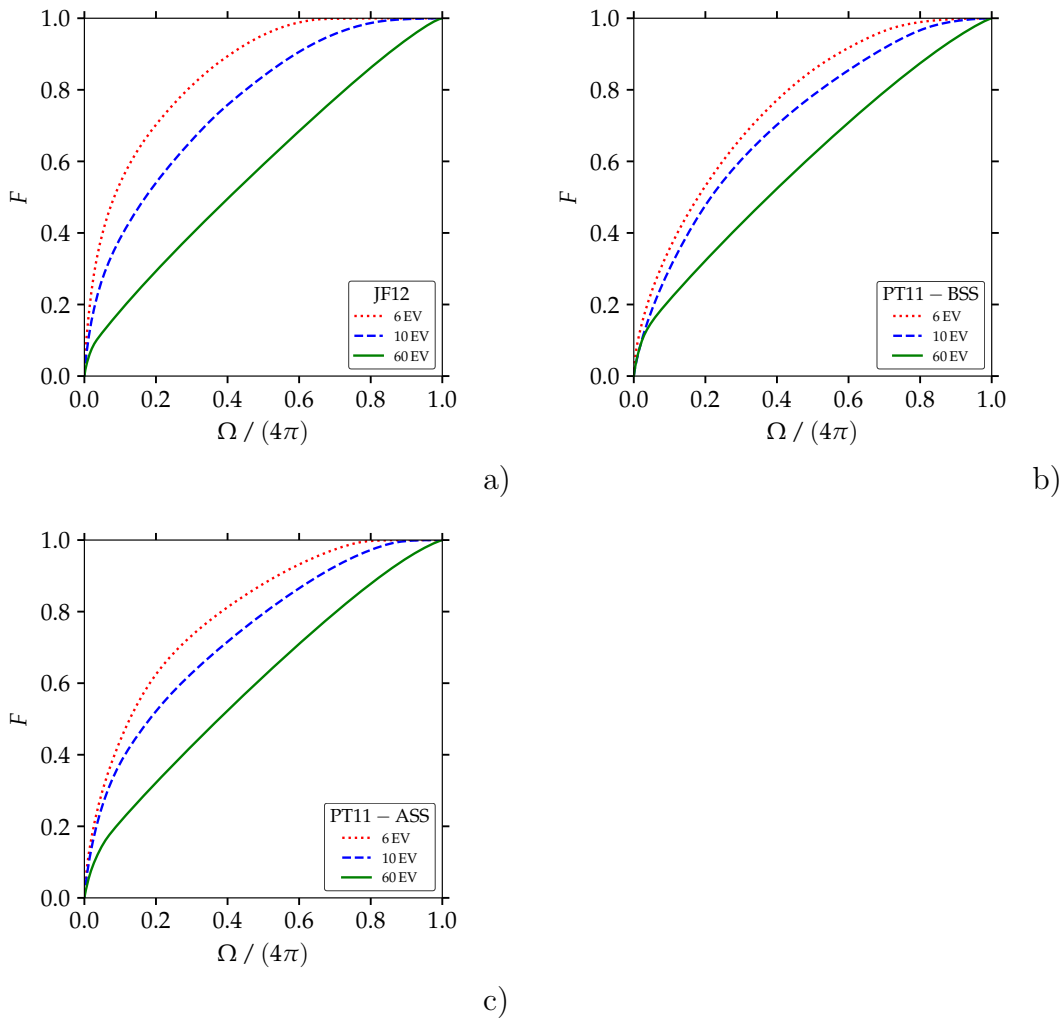


Figure 5.9: Integrated relative flux  $F$  of observed cosmic rays originating from the incoming directions with the highest arrival probabilities covering  $\Omega/(4\pi)$  of the sky, a) JF12, b) PT11-BSS and c) PT11-ASS.

In a more general approach in figure 5.9 the relative flux  $F$  of observed cosmic rays is shown as a function of the solid angular region  $\Omega/(4\pi)$  covered by the incoming directions with the highest arrival probabilities. At low rigidity  $R = 6$  EV in the JF12 parameterization 95% of the cosmic ray flux on Earth is caused by about 50% of the extragalactic directions (figure 5.9a). With increasing rigidity all extragalactic directions contribute equally to the flux on Earth. The PT11 parameterization yields similar results as shown in figure 5.9b and c, however, with less inhomogeneity at low rigidity  $R$ .

In contrast, the flux from certain extragalactic directions is not only suppressed but can even disappear, as no path leads to observation on Earth. As an example figure 5.10 displays example trajectories of cosmic antimatter with rigidity  $R = 60$  EV from the same extragalactic direction traversing a thin slice of  $\pm 500$  pc around the  $x$ - $z$ -plane in the galactic coordinate system. The trajectories are expected to miss the solar environment (marked by the yellow star). To enable this demonstration for antimatter a separate set of lenses is produced by backtracking matter particles in the JF12 field.

In general, both matter and antimatter particles entering the galaxy exhibit directions with a negligible arrival probability on Earth. In figure 5.11 the fraction of the sky is shown in terms of solid angles  $\Omega_B$ , where none of 100 simulated cosmic rays reached Earth as a function of their rigidity  $R$ . For antimatter trajectories in the JF12 field, invisible directions appear at small and large rigidities (dashed curve).

For matter particles of rigidity  $R = 6$  EV traversing the JF12 field, the invisible sky fraction is about 20% and disappears above  $R \sim 10$  EV (blue curve). In contrast, for the PT11 field the invisible fraction of the sky for matter particles appears to be generally small (red curve).

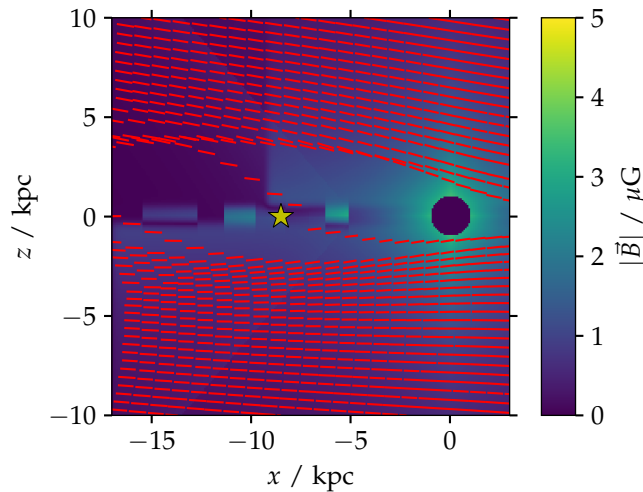


Figure 5.10: Example trajectories of cosmic antimatter with rigidity  $R = 60$  EV incoming to the JF12 field from the same direction that miss the solar system (yellow star). The trajectories are shown in a thin slice of  $\pm 500$  pc around the  $x$ - $z$ -plane.

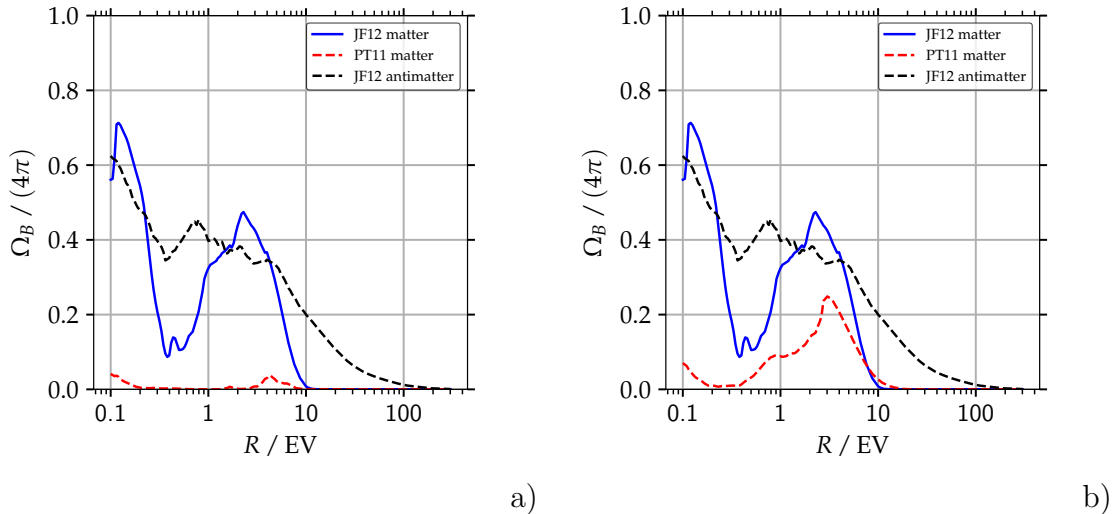


Figure 5.11: Directions with unobserved cosmic matter (full curves) and antimatter (dashed curve) in terms of covered solid angle  $\Omega_B$  as a function of rigidity  $R$  (blue curve JF12, red curve PT11-BSS (a) / PT11-ASS (b)).

At cosmic ray rigidities of  $R = 6$  EV, variations in the field transparency from specific extragalactic directions lead to relative suppression and enhancement effects which may eventually require corrections in individual arrival direction analyses. The variations are strongly reduced with increasing cosmic ray rigidity.

### 5.2.5 Small-scale Random Field

Beyond the regular large-scale component, recent galactic magnetic field models also contain small-scale random structures which are motivated e.g. by supernovae [199, 200, 201]. Such local disturbances are expected to cause a randomly oriented field component which introduces uncertainties in the predicted arrival directions of extragalactic cosmic rays. This impact is expected to be small, since the direction of the random component changes on a scale that is substantially smaller than the gyroradius of cosmic rays constrained in the galaxy.

To investigate the influence of such random fields two different realizations of the so-called striated and turbulent random components are compared as described in [200] with a coherence length of  $\lambda = 60$  pc. Cosmic rays are then deflected in both the regular JF12 and the first random field realization, and in the regular JF12 and the second random field, respectively.

The lensing technique is used to investigate the influence of the random fields on arrival directions. To obtain the most probable arrival direction on Earth the same techniques described above when studying the dispersion of the probability distribution (section 5.2.2) are used. The radius  $r_{50}$  containing 50% of the arrival probabilities is calculated, and use the center of the pixel with the smallest radius  $r_{50}$  as the expected arrival direction.

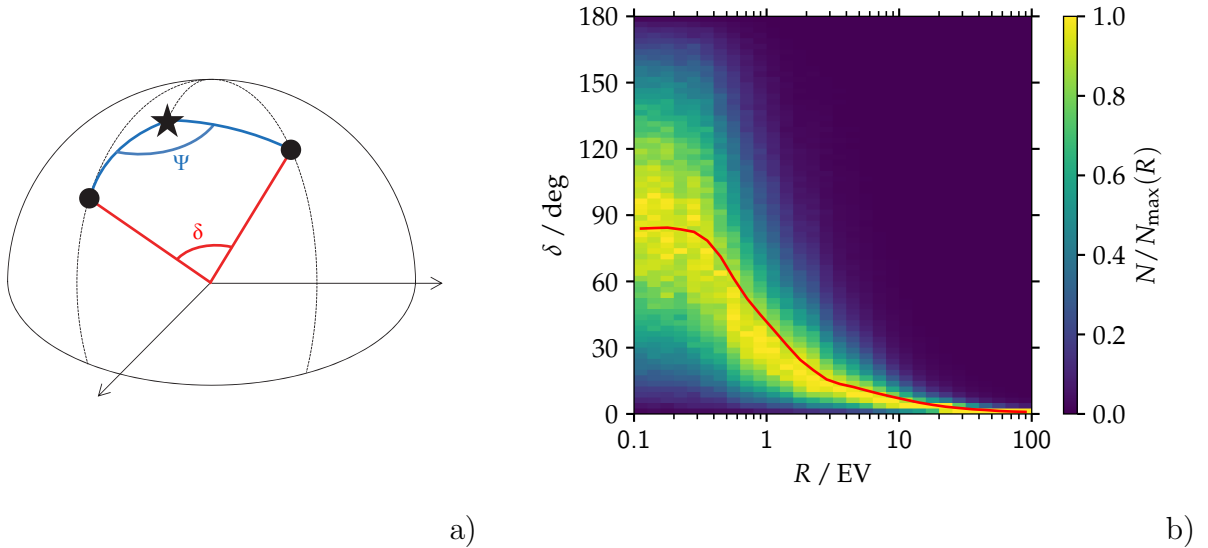


Figure 5.12: a) Angular distance  $\delta$  between two cosmic ray arrival directions (circular symbols) from an incoming direction (star symbol), and directional difference  $\Psi$  of the deflections (tangential to the sphere) resulting from different magnetic field orientations. b) Angular distances  $\delta$  between the arrival directions using two different realizations of the striated and turbulent random components in addition to the regular JF12 field parameterization as a function of rigidity  $R$ . The median is depicted by the curve.

In figure 5.12a the angular distance  $\delta$  between the arrival directions resulting from the two random field realizations is sketched. Here the incoming cosmic ray direction to the galaxy is indicated by the star symbol, and the two alternative arrival directions are denoted by the circular symbols.

Figure 5.12b displays the angular distances  $\delta$  between the arrival directions on Earth using the two realizations of the random fields as a function of cosmic ray rigidity  $R$ . The red curve indicates the median values. For rigidity  $R = 6$  EV the uncertainty in the arrival directions is below  $10^\circ$  for 50% of the cosmic rays, and rarely extends to more than  $90^\circ$ .

As expected, the impact of the random field is significantly smaller compared to the deflections of the cosmic rays arising from the regular galactic field (figure 5.4). However, the uncertainties generated by such random deflections are sufficiently sizable to consider optimization of the rigidity threshold for individual arrival direction analyses.

In order to work in a phase space region in which cosmic ray deflections can be controlled at least in a probabilistic way a minimum cosmic ray rigidity of  $R = 6$  EV is recommended. This value results from avoiding deflections leading to a bend of  $90^\circ$  which overlaps with cosmic ray diffusion. All other distributions presented above on the dispersion of arrival probability distributions and multiple images,

variance in field transparency, and uncertainties due to random field components are in accordance with this minimal rigidity value.

For a typical large-scale analysis the  $R = 6$  EV rigidity threshold may be sufficient. However, depending on individual analysis requirements, the above key distributions may help to determine whether the rigidity threshold needs to be adjusted to larger values, or whether restrictions to incoming directions aside the galactic disk region need to be introduced.

## 5.3 Influences of Field Uncertainties on Cosmic Ray Arrival

For a typical point source search, the reliability of galactic field corrections are of utmost importance. As a first step the cosmic ray deflections resulting from the two field parameterizations PT11 and JF12 are directly compared.

In order to exemplify the impact of these differences on point source searches a typical corresponding analysis is simulated. The discovery potential is determined when the true galactic field is known, and the reduced discovery potential quantified when taking into account the different deflections of the two field parameterizations.

### 5.3.1 Comparison of Deflection Angles

Uncertainties in the current knowledge of the galactic field can be obtained to some extent from the different arrival distributions of the two field parameterizations PT11 and JF12. Note that their fields are not completely independent regarding the overlap in the measurements constraining their fits, and usage of similar electron density distributions. However, the two parameterizations follow different ansatzes and include disjoint measurements, such that a direct comparison of cosmic ray deflections at least gives an idea of limited knowledge in the magnetic field.

For cosmic rays originating from the identical extragalactic direction  $(l, b)$  the different deflections resulting from the two field parameterizations are investigated. The above-mentioned lensing technique is used to deliver arrival probability distributions. As outlined in section 5.2.5, the most probable arrival direction on Earth are calculated by using the center of the pixel with the smallest radius  $r_{50}$  containing 50% of the arrival probabilities. This gives the expected arrival directions  $(l', b')$  for the JF12 parameterization and for the PT11 parameterization, respectively.

Firstly, the different directions of cosmic ray deflections are studied by their azimuthal angular distance  $\Psi$  which is measured tangentially to the sphere (see figure 5.12a). These directional differences reflect different field orientations of the two parameterizations.

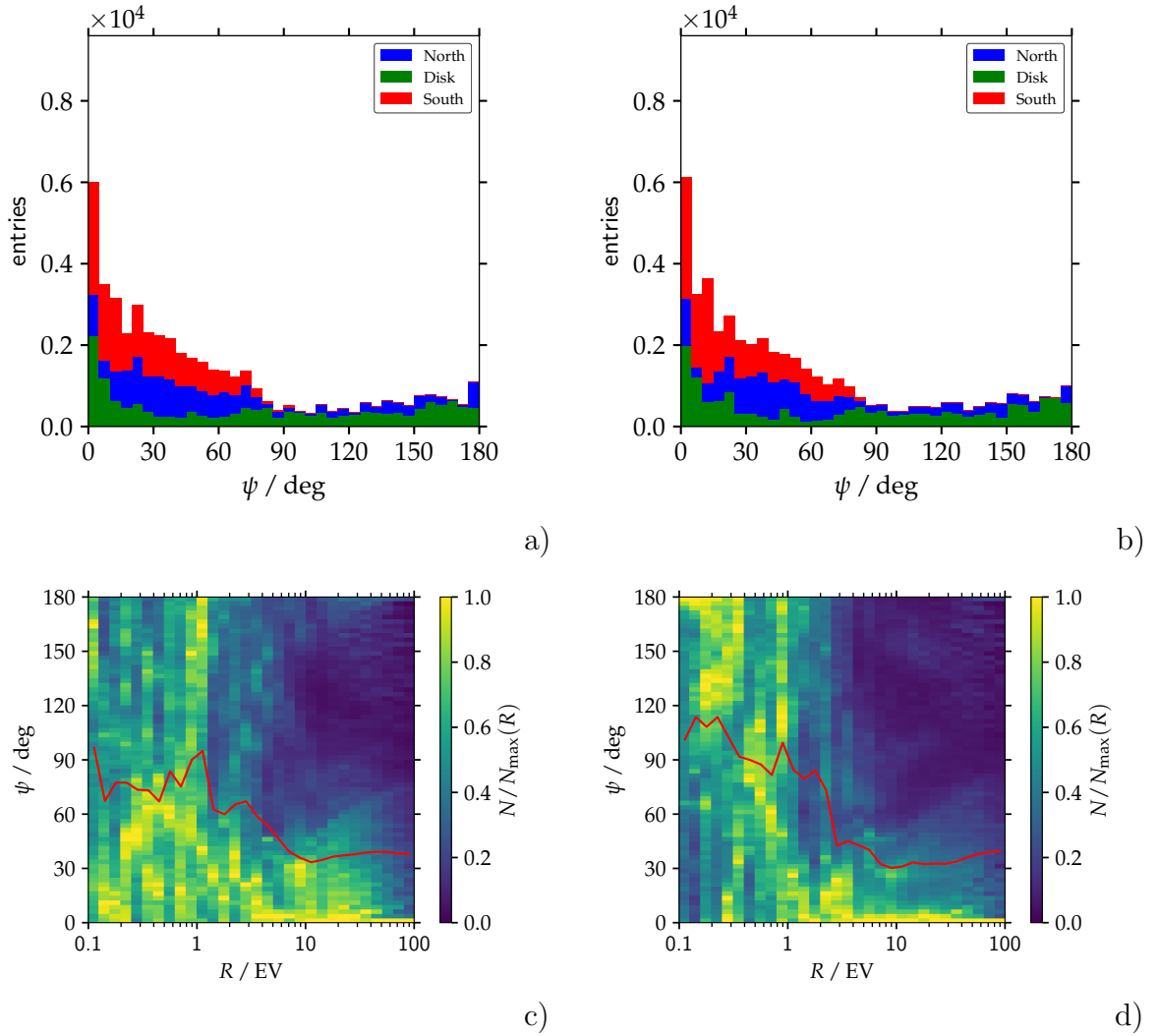


Figure 5.13: Difference  $\Psi$  in the directions of the deflections between JF12 and PT11-BSS (left) / PT11-ASS (right), a) and b) for rigidity  $R = 60 \text{ EV}$  in the three regions separated by galactic latitudes  $\pm 19.5^\circ$ , c) and d) as a function of rigidity. The curve depicts the median values.

In figure 5.13a the directional difference  $\Psi$  for cosmic ray rigidity  $R = 60 \text{ EV}$  are shown for the three regions separated by galactic latitudes  $\pm 19.5^\circ$ . For the southern region almost all directions of the deflections are within  $90^\circ$  (red histogram). In the northern region most of the incoming directions show  $\Psi < 90^\circ$  (blue histogram). About  $1/5$  of the incoming directions exhibit  $\Psi > 90^\circ$ , i.e. here the directions are nearly opposite.

In the disk region the differences between the two fields are large as half of the incoming directions are within  $90^\circ$ , and the other half has directional differences above  $90^\circ$  (green histogram).

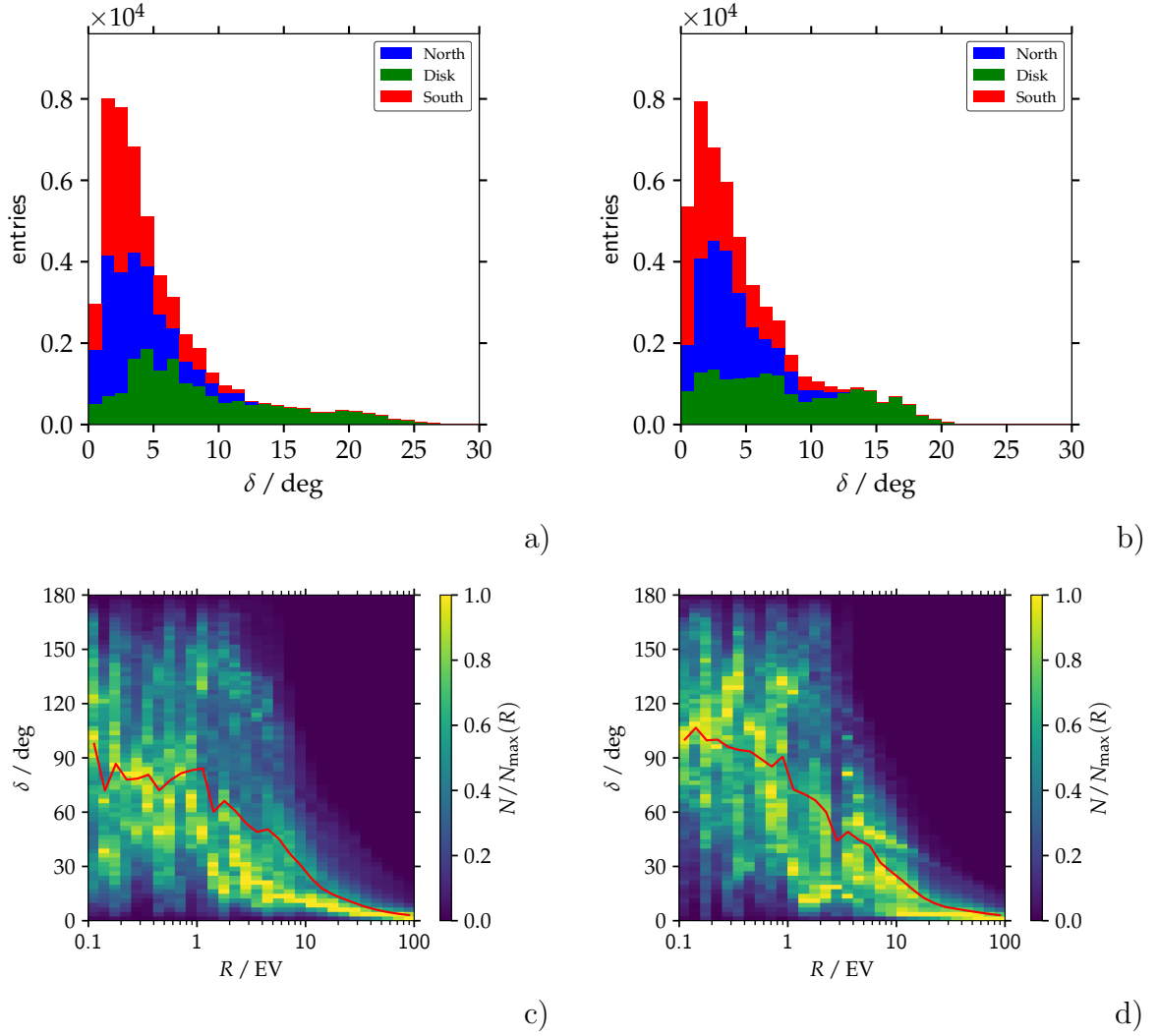


Figure 5.14: Angular distance  $\delta$  of cosmic rays after deflections in JF12 and PT11-BSS (left) / PT11-ASS (right), a) and b) for rigidity  $R = 60$  EV in the three regions separated by galactic latitudes  $\pm 19.5^\circ$ , c) and d) as a function of rigidity. The curve depicts the median values.

Figures 5.13b and c display the rigidity dependence of the directional difference  $\Psi$  for all regions where the curve represents the median values. For all rigidities above  $R = 6$  EV, the most likely differences in the directions of the deflections are below  $10^\circ$ , and for 50% of the cosmic rays the field directions are within  $40^\circ$ .

The second important aspect of the field differences is the absolute angular distance in the arrival directions resulting from the PT11 and JF12 parameterizations which are denoted by  $\delta$  (see figure 5.12a).

Figure 5.14a displays the angular distance  $\delta$  for cosmic rays with rigidity  $R = 60$  EV for the three regions separated by galactic latitudes  $\pm 19.5^\circ$ . For the northern and southern regions the angular distance between the two parameterizations is below  $\delta = 5^\circ$  for 3/4 of the incoming directions (blue, red histograms).

In the disk region, only 1/3 of the arrival directions show angular distances below  $\delta = 5^\circ$ , while the majority of incoming directions have larger angular distances up to  $\delta = 30^\circ$ .

Figures 5.14b and c display the angular distance  $\delta$  for all regions as a function of cosmic ray rigidity. The curve represents the median values. For cosmic rays with small rigidity  $R = 6$  EV, half of them result at an angular difference below  $30^\circ$ . However, there is a long tail towards large angular distances resulting from the two field parameterizations.

Although sizable differences in the directional characteristics and magnitudes of the two field parameterizations exist, their influence is sufficiently reduced at large cosmic ray rigidity. For example, at  $R = 60$  EV, the absolute deflection angles  $\beta$  as well as the angular distances  $\delta$  arising from the two fields become consistently small for most incoming directions. Further studies show that in the northern and southern regions the median ratio of the angular distance  $\delta$  and the averaged deflection  $(\beta(\text{JF12}) + \beta(\text{PT11}))/2$  remains approximately flat for rigidities  $R > 10$  EV.

### 5.3.2 Comparison of Arrival Directions

In figure 5.15 example arrival distributions of cosmic rays with rigidity a)  $R = 20$  EV, b)  $R = 60$  EV originating from ten sources are shown. The directions of the sources are denoted by the star symbols. The initial cosmic ray distributions followed the Fisher distribution with a Gaussian width of  $3^\circ$ .

Indicated by the dark (light) red regions are the 68% (95%) arrival probability distributions of the cosmic ray after deflections by the PT11 field. The blue regions give the corresponding arrival probability distributions from the JF12 field.

At cosmic ray rigidity  $R = 20$  EV (figures 5.15a and b) at least half of the arrival probability distributions exhibit substantial overlap for the PT11 and JF12 fields. With increasing rigidity (figures 5.15c and d,  $R = 60$  EV) the overlap increases as expected. The number of images is also reduced at larger rigidity.

This implies that, at large rigidities, the agreement of the two field parameterizations is sufficiently large to investigate the impact of the field uncertainties on a point source search which are presented in the following section.

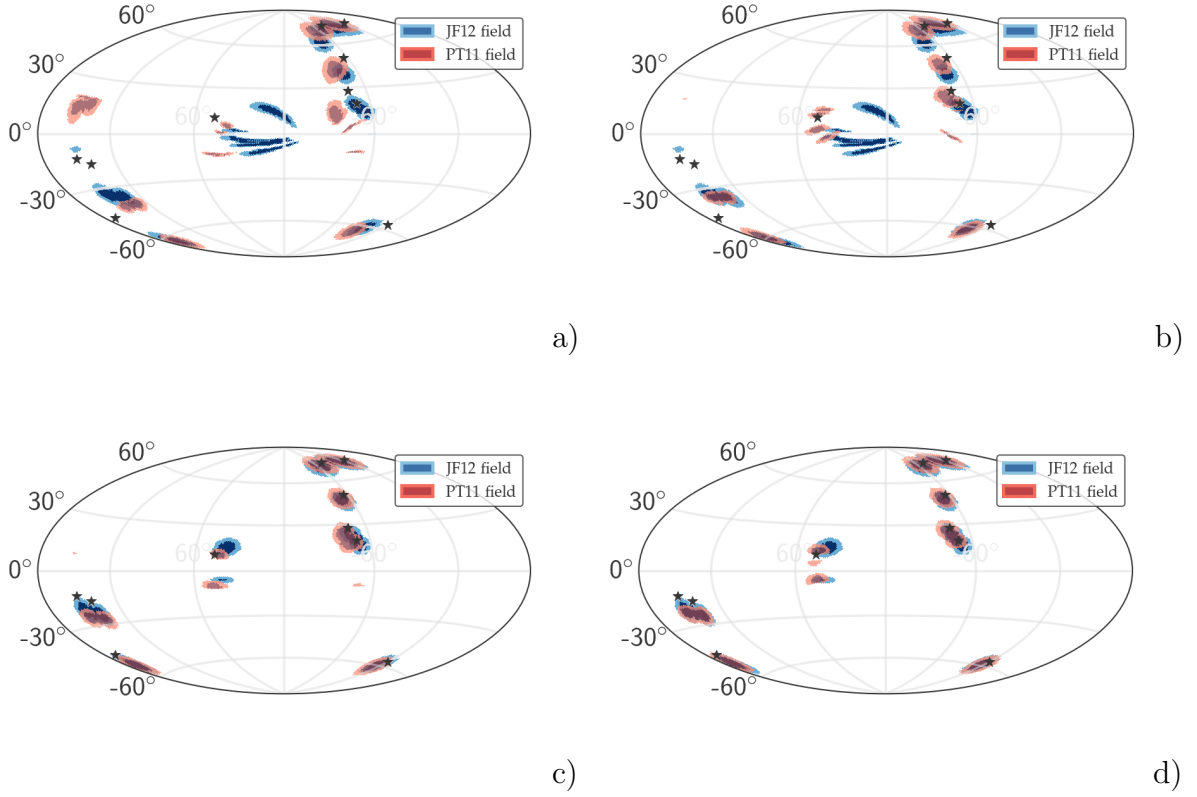


Figure 5.15: Probability density functions reflecting arrival distributions of cosmic rays after traversing the PT11-BSS (left) / PT11-ASS (right) galactic magnetic field (red contours) or the JF12 field (blue contours), respectively. The contours denote 68% and 95% levels. The incoming cosmic ray distributions were centered at the directions denoted by the star symbols and Fisher distributed with a Gaussian width of  $3^\circ$ ; rigidity a and b)  $R = 20$  EV, c and d)  $R = 60$  EV.

### 5.3.3 Simulated Point Source Search

For the simulated search for origins of cosmic rays, the sources in the three regions of the galaxy (latitude  $\pm 19.5^\circ$ ) are studied separately. In each region ten sources are repeatedly simulated and the cosmic rays are required to follow a Fisher probability distribution with a Gaussian width of  $3^\circ$ .

Isotropically distributed cosmic rays with full sky coverage are also simulated as a background contribution. In the following multiple analyses are performed with sets of 500 cosmic rays for which the contribution of signal cosmic rays is varied, i.e. cosmic rays arriving from the ten sources, between signal fraction  $f_s = 0\%$  and  $f_s = 100\%$ .

To quantify the analysis sensitivity the log-likelihood function is used:

$$\ln L(a) = \sum_{i=1}^N \ln [a P(R_i, l'_i, b'_i) + (1 - a) B] \quad (5.2)$$

The sum refers to all simulated  $N = 500$  cosmic rays. Parameter  $a$  denotes the anticipated fraction of signal cosmic rays from the sources when analyzing the data, and the isotropically distributed cosmic rays are assumed to contribute with  $(1 - a)$  correspondingly. The probabilities  $P(R, l', b')$  represent the anticipated arrival probability distributions for cosmic rays with rigidity  $R$  which originate from the sources and are expected to be observed in directions  $(l', b')$  on Earth. They were obtained using the lensing techniques. The background probability  $B$  corresponds to the inverse number of pixels for which the above  $N_{pix} = 49,152$  pixels of approximately one degree are used.

As test statistics the likelihood ratio

$$t = 2 \ln \frac{L(a)}{L(a=0)} \quad (5.3)$$

is used which approximately follows a  $\chi^2$  distribution with one degree of freedom [202]. For each anticipated signal fraction  $a$  the simulation of cosmic ray sets is repeated 1000 times and determine the average maximum  $t_{max}$ . The significance by which isotropic arrival distributions can be excluded is then estimated by converting the integral  $\int_{t_{max}}^{\infty} \chi^2 dt$  above  $t_{max}$  to Gaussian standard deviations  $\sigma$ .

In the analysis, the JF12 arrival probability distributions  $P(R, l', b')$  are used as the simulated scenario to describe cosmic ray deflections. To obtain a benchmark for a best-case scenario, where the field and the cosmic ray rigidities are perfectly known, first cosmic rays with rigidity  $R = 20$  EV are analyzed by using the JF12 field, here representing the true field. Note that this scenario returns optimistic results as deflections in the small-scale random field are neglected and sources are demanded to be located in one of the three galactic regions exclusively.

Figures 5.16a and b display the significance  $\sigma$  as a function of the signal fraction  $f_s$  of the simulated sample. With perfect knowledge of the galactic field a signal fraction of  $f_s = 5\%$  is sufficient for a  $5\sigma$  discovery (full curves).

To take into account uncertainties in the galactic field as encoded in the two different parameterizations, the analysis is then performed with the PT11 arrival probability distributions instead of the true JF12 probability distributions. As the results are slightly dependent on the exact directions of the sources, the analyses are repeated nine times in each region and the average resulting values are presented.

In figures 5.16a and b the significance  $\sigma$  of a deviation from isotropic arrival distributions are shown as a function of the average signal fraction  $f_s$  for the three regions (dashed curves). A signal fraction of  $f_s = 14\%$  is sufficient for a  $5\sigma$  discovery for the northern and southern regions, and slightly larger for the disk region ( $f_s = 18\%$ ). When compared to the above best-case scenario, the field uncertainties require the signal fraction for discovery to increase substantially by a factor of 3 – 4.

In figures 5.16c and d the required signal fraction  $f_s(5\sigma)$  for discovery is presented as a function of cosmic ray rigidity  $R$ . The full curves represent the required signal fraction for the benchmark scenario having perfect knowledge of the galactic magnetic field. The required signal fraction  $f_s(5\sigma)$  when including field uncertainties are shown by the dashed curves.

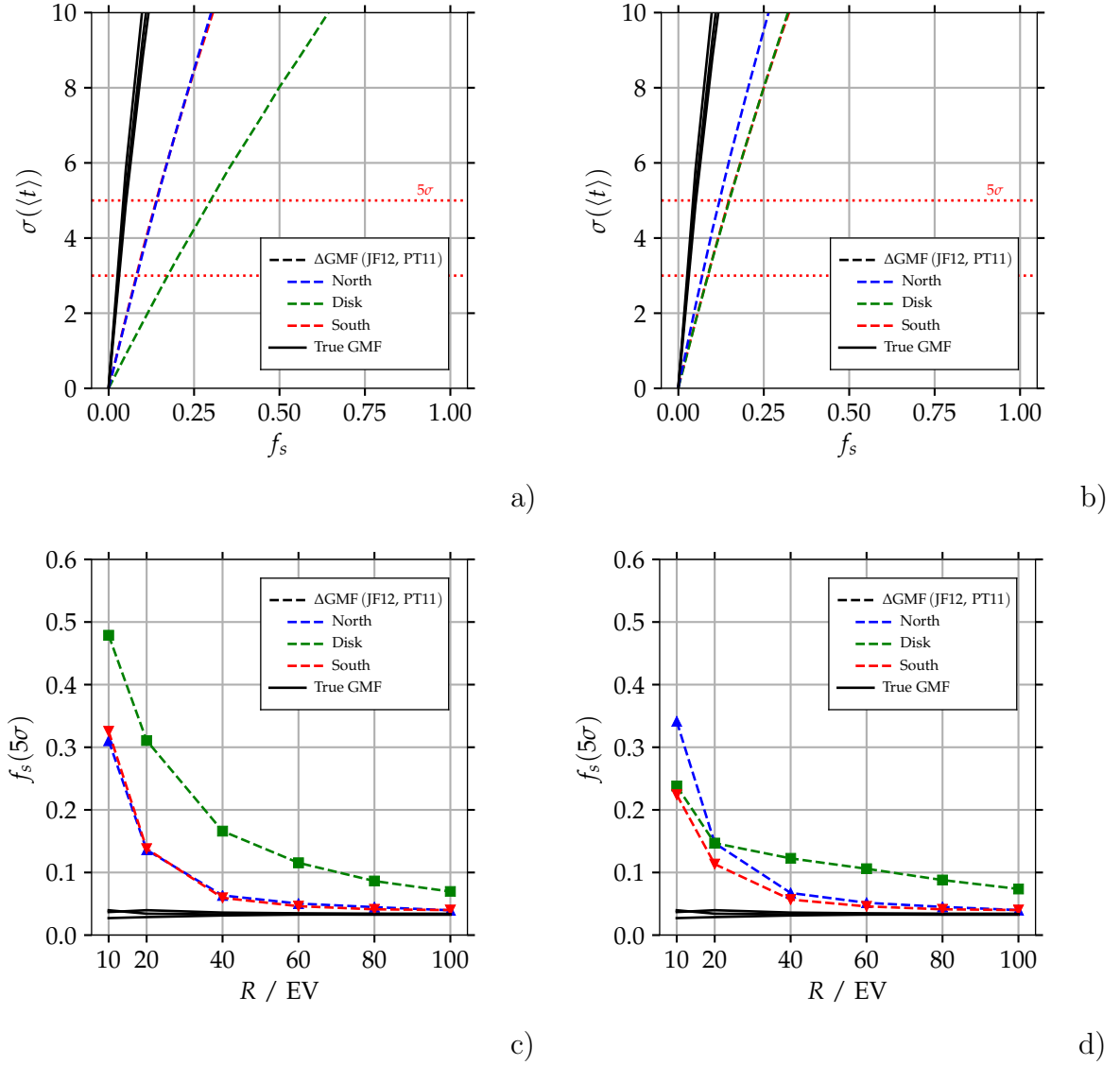


Figure 5.16: Simulated point source search with ten sources located in one of the three regions separated by galactic latitudes  $\pm 19.5^\circ$  and sets of 500 cosmic rays with fraction  $f_s$  originating from the sources and  $(1 - f_s)$  from isotropic background with full sky coverage. The left plots use the PT11-BSS field, the right ones PT11-ASS. a) and b) Significances for deviation from isotropic arrival distributions at  $R = 20$  EV using the true galactic field (full curves) for the anticipated arrival probability  $P$  in equation (5.2), and the other field alternatively (dashed curves). c) and d) Required signal fraction for a  $5\sigma$  deviation from isotropic arrival directions using the true field (full curves) compared to using the other field (dashed curves) as a function of rigidity  $R$ .

It is interesting to note that, although deflections are on average twice as large in the southern region compared to the northern region, their sensitivities are of similar value above rigidity  $R = 20$  EV. In the disk region the different characteristics of

the two parameterizations have a large impact on the point source search. Here the required signal fraction almost doubles irrespective of rigidity.

As expected, the sensitivity of the point source search improves consistently with increasing cosmic ray rigidity. Again comparing with the above best-case scenario, cosmic rays with  $R = 60$  EV entering the galaxy in the northern or southern regions require a moderate 20% increase in the required signal fraction for discovery owing to field uncertainties. In contrast, incoming directions at the disk region need a 2.5-fold larger signal fraction.

In view of the current knowledge of the galactic field, for analyses which aim at selected source directions and require corresponding galactic field corrections a cosmic ray rigidity of at least  $R = 20$  EV is recommended. In the simulated search, the required signal fraction for a  $5\sigma$  discovery remains below 20% [at least outside the disk region].

### 5.3.4 Summary of the Influence of Field Uncertainties on Cosmic Ray Arrival

The direct comparisons of cosmic ray deflections in the two field parameterizations provide some information on the actual knowledge of the entire field map. For cosmic ray rigidity  $R = 6$  EV, the angular distance after deflections in the two fields is within  $\delta = 30^\circ$  for 50% of the directions incoming to our galaxy. This value is much smaller at  $R = 60$  EV rigidity, where the differences are below  $\delta = 5^\circ$  for 60% of the directions incoming to our galaxy.

To study the influence of uncertainties in the field on searches for cosmic ray origins, simulated astrophysical scenarios were analyzed using a log-likelihood method. The method includes the anticipated probability distributions for cosmic ray arrival after traversing the galactic field, and quantifies deviations from isotropic arrival distributions.

The influence of field uncertainties is estimated by using one field parameterization in the simulation of the scenario, and by applying the other field parameterization in the log-likelihood analysis. For cosmic rays with rigidity  $R = 60$  EV arriving from sources within galactic latitudes  $\pm 19.5^\circ$  (disk region) it is found that the field uncertainties increase the required signal fraction for a  $5\sigma$  discovery substantially by more than a factor of two. However, for sources in the northern and southern regions emitting cosmic rays with  $R = 60$  EV, the field uncertainties are relatively small and increase the required signal fraction for a  $5\sigma$  discovery by 20% only.

## 5.4 Conclusion

Corrections for deflections in the galactic magnetic field using the two parameterizations PT11 and JF12 can be meaningfully considered for cosmic ray rigidities above  $R > 6$  EV. Above this rigidity, deflections can be distinguished from diffusive random walk. This has strong implications for analyses using cosmic ray data with mixed composition. For protons this rigidity corresponds to energies above

$E = 6$  EeV. However, when analyzing, e.g., Neon nuclei with charge  $Z = 10$ , meaningful corrections can be performed for energies above  $E = 60$  EeV only.

When quantifying uncertainties in the galactic field from comparisons of the two field parameterizations PT11 and JF12, the rigidity threshold needs to be raised substantially. Then both fields give similar predictions for cosmic ray deflections in the northern and southern regions with galactic latitudes  $|l| > 19.5^\circ$ . In the disk region  $|l| < 19.5^\circ$ , however, the differences in the predictions remain large. Consequently, in the simulated search for cosmic ray origins the arising uncertainties are substantial for sources near the galactic disk, and may be considered acceptable for sources aside the disk emitting cosmic rays with rigidities  $R \geq 20$  EV.

The PT11-ASS parameterization describes the measurement of rotation measurements better than the PT11-BSS model [187]. Furthermore, the axialsymmetric model shows overall more similarities to the JF12 parameterization than the bisymmetric parameterization. This manifests itself in figure 5.16 where at the lowest energies a smaller signal fraction is required to achieve a significance of  $5\sigma$ . It is also visible in the exemplary distributions in figure 5.15 where the overlap between the JF12 and PT11-ASS parameterization is larger than to PT11-BSS.



# 6. Experimental Setup

This section describes all steps from recording to the selection required to obtain a precise data set of ultra-high energy cosmic rays for anisotropy studies. First, the different triggers are presented before showing how energy and shower axis are reconstructed. Finally, various distributions of the data selected by different quality cuts are shown.

## 6.1 Trigger Definitions

When a cosmic ray hits the atmosphere an extensive air shower containing many secondary particles evolves in the atmosphere. Secondary particles reaching ground can be measured by the photomultiplier tubes (PMT) in a surface detector (SD) station. To distinguish a cosmic ray event from a background event, different triggers must be fulfilled till the event is finally recorded. These triggers are set up in a hierarchical way, the first two triggers T1 and T2 are implemented at station level, the next level T3 in the central data acquisition system (CDAS) followed by a physics trigger T4 and a fiducial trigger T5. The following discussion is based on the fully detailed description in [203].

**T1 and T2:** The main purpose of the station triggers is to reduce the event rate on a single station level by mainly removing background events. Both triggers have two modes: “Threshold” (TH) and “Time-over-Threshold” (ToT). The TH trigger is a classical trigger sensitive to large signals coincidentally measured in all photomultipliers (PMT) whereas the ToT trigger requires a small increase in the signal over background ratio for more than 325 ns within a sliding window of 3  $\mu$ s accounting for a dispersed signal e.g. for stations not close to the shower core. Each station with a T1 trigger stores the measured time traces for each PMT. The second level T2 is the same for the ToT-T1 case and requires a signal about twice as high as in the TH-T1 case. All stations measuring a T2 trigger autonomously send the measured timetraces to the CDAS via the communication antenna.

**T3:** This trigger initially requires at least 3 ToT-T2 (4 TH-T2) triggers and then looks for geometry and time correlations of the signal taking into account all stations and their respective location that had at least a T1 trigger within 30  $\mu$ s of the T3. It has different requirements that must be fulfilled depending on the T2 type, e.g. the compactness of the array of triggered stations; for precise numbers see [203].

**T4:** This trigger considers the physical properties of the event by fitting a plane shower front to the arrival times of the individual stations. It has an efficiency of

more than 98% to correctly identify a cosmic ray event with a zenith angle below  $60^\circ$  [203, 204]. Furthermore, it allows to identify accidentally triggered stations, e.g. by a cosmic muon, and to remove them for further reconstruction.

*The remaining description in this section 6.1 is part of the the publication “Observer Data Set for Anisotropy Studies including 4T5 events”[205]. Within this thesis the implementation concept for active triangles as an extension of the T5 trigger has been developed for the analysis and reconstruction framework “Auger Offline”. Furthermore, the new routines were crosschecked by an independent implementation. Additionally, the text of the publication [205] was essentially written by the author of this thesis.*

**T5:** The fiducial trigger (T5) counts the number of active stations around the station with the highest signal which is called hottest station. It ensures that the showers are contained inside a valid detector hexagon and is used to cut events where a part of the stations is missing either as they are not operating properly or because the event is measured at the edge of the array. For these events the core position and consequently the energy might be misreconstructed [203].

However, a proper reconstruction of energy and direction is still possible when the shower core falls into either an equilateral or an isosceles triangle of active stations where the hottest station is at one corner, see also [86].

### 6.1.1 Active and Non-Rejected Stations

The T5 trigger, as well as the calculation of active triangles, take only active and non-rejected stations into account. A station is considered active when it regularly sends a T2 trigger to CDAS.

A rejection status is assigned to each station individually for each event. Typical rejection reasons are lightning or station specific problems like broken PMTs or a bad calibration. A station with a rejection status is not taken into account for the reconstruction. But the following rejection statuses mean that the station is in principle operating, and thus they are considered to be acceptable for the fiducial trigger:

- station is out of time (timing deviates from plane shower front)
- station triggered on random trigger (muon buffers)
- triggered station is lonely, i.e. with large distance to other stations
- the station has only the new triggers ToTd and MoPS [39]

Additionally, a station might be flagged during the reconstruction with the rejection status *bad silent* when it is close enough to the shower core but did not observe a signal. Due to this flag it is distinguished between the T5 triggers before and after reconstruction. The number  $N$  of active stations around the station with the highest signal is added as label, i.e.  $NT5$  trigger. So, if all stations around the hottest station are active its name is  $6T5$  and similar  $5T5$  if one station is missing.

### 6.1.2 Active Triangles

An active triangle consists of three neighboring and active stations in the hexagonal grid of the surface detector. It has been shown that energy and direction of the cosmic ray are properly reconstructed if the shower core falls into an active triangle [86]. The calculation to determine whether the shower core falls into an active triangle is separated into three steps. First, all possible triangles, either equilateral or iso-sceles both including the hottest station as one point, are calculated. Due to the slightly different altitudes of the stations each triangle spans its own plane. In the next step, the shower core is projected alongside the shower axis into these planes. Afterwards, it is checked if the core is contained inside the triangle by calculating for all three corners if the vector  $\vec{p}_2$  from a corner of the triangle to the shower core lies between the vectors from this corner to the remaining two corners. An example of the calculation is shown in figure 6.1.

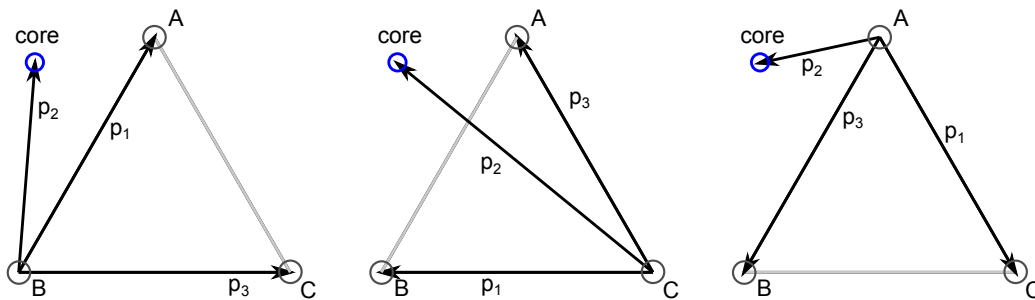


Figure 6.1: Calculation of the active triangle. In this case the core is outside the triangle. To prove this mathematically the result of the product (6.1) has to be calculated for all three corners. This requires each time to redefine the vectors  $\vec{p}_{1,2,3}$ . Note that  $\vec{p}_1$  and  $\vec{p}_3$  are defined clockwise. The outcome of equation (6.1) is negative (left), positive (middle) and positive (right). Only in cases when the point is inside the triangle all corners return a positive result.

Equation (6.1) is larger than zero if the vector  $\vec{p}_2$  from a corner to the shower core lies on the same side as  $\vec{p}_3$  with respect to the line described by  $\vec{p}_1$ . Thus a point  $\vec{p}_2$  lies within the triangle if the outcome of equation (6.1) is positive for all combinations of corners showed in figure 6.1.

$$(\vec{p}_1 \times \vec{p}_2) \cdot (\vec{p}_1 \times \vec{p}_3) \geq 0 \quad (6.1)$$

Note that the shower core is not contained inside the hexagon for 0.2% of all 6T5 posterior events .

### 6.1.3 Implementations of the Fiducial Trigger and the Active Triangles

The following functions are newly implemented in the `SDEvent` class in `Offline` and available via the ‘‘Advanced Data Summary Tree’’ (ADST) interface.

- `unsigned int GetT5PriorActiveNeighbors()` returns the number of active and non rejected stations prior to the reconstruction.
- `unsigned int GetT5PostActiveNeighbors()` behaves similar to the prior function but takes into account *bad silent* stations.
- `unsigned int GetT5PostCoreTriangle()` calculates in which triangle type the shower core lies. It returns
  - 0, when the shower core does not fall into a triangle,
  - 1, for the equilateral triangle,
  - 2, for the isosceles triangle and
  - 3 for both.

In figure 6.2 the different possibilities are sketched for four exemplary events. The majority of the events has a shower core close to the hottest station and is thus contained inside both triangle types (case 3). If there is a bad station in the hexagon around the hottest station, the shower core typically falls into an isosceles triangle (case 2). In some cases the core is close the border of the outer hexagon either close to a working station (case 1) or close to a bad station (case 0).

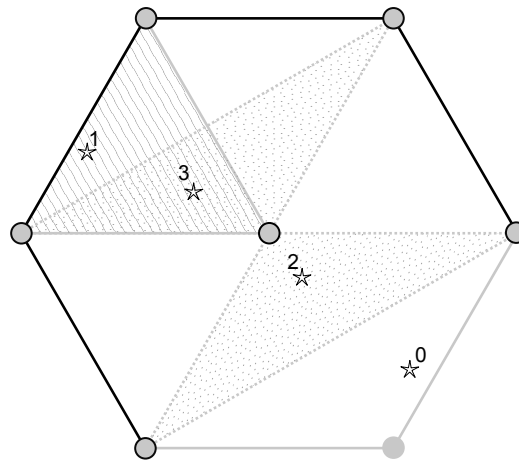


Figure 6.2: Exemplary triangle classification for 4 events. The circles denote the SD stations around the hottest station in the center. The station at the lower right is marked as bad station. The dashed triangle is an equilateral triangle and the dotted areas denote two different isosceles triangles. The stars show four different event types and the numbers indicate the return value of the `GetT5PostCoreTriangle()` function.

All functions have been tested by a second, independent implementation. The trigger logic is available since Offline revision 31568.

## 6.2 Event Reconstruction

After an event has been accepted as physics event (T4 trigger), it is stored on hard disk and the properties of the primary cosmic ray are reconstructed. These are primarily energy and direction; mass and charge are also of interest but can not be measured directly. However, the atmospheric depth of the shower maximum is related to the mass number. It is directly measured by the fluorescence detector (FD), for the surface detector novel techniques are investigated [93, 95], some also include machine learning methods [96, 206].

In this analysis a data set consisting of events measured by the SD is used as anisotropy studies strongly depend on the number of events and the FD has a lower statistics due to an uptime of 13% [44]. In the following, the directional reconstruction and afterwards the energy reconstruction are presented.

### Directional reconstruction

The directional reconstruction is based on both, the timing and the signal strength of the stations and executed in multiple stages incorporating more and more details. The full description can be found in [39, 207].

- The shower geometry is reconstructed by assuming a spherical shower front. However, for configurations where not enough stations have triggered a planar front is assumed. The following description concentrates on the spherical fit as this is the predominant case for energies above 8 EeV and zenith angles  $\theta < 60^\circ$ . The evolution of the sphere with the speed of light  $c$  can be described by a virtual starting time  $t_0$  and origin  $\vec{x}_0$  and the times  $t_i$  and positions  $\vec{x}_i$  of the individual stations:

$$c \cdot (t_0 - t_i) = \|\vec{x}_0 - \vec{x}_i\| \quad (6.2)$$

- The impact point on ground  $\vec{x}_{\text{gr}}$  is obtained by using the previous result and a fit of a lateral distribution function (LDF) to the signal strengths  $S$  measured in the individual stations with distance  $r$ . The utilized LDF is a modification of the parameterizations by Nishimura, Kamata and Greisen (NKG) [26, 27], see equation (6.3) [32]. Here,  $S_{1000}$  is the fitted signal strength at 1000 m and  $\gamma$  corresponds to the initial exponent, whereas  $\beta$  contains a correction depending on the zenith angle  $\theta$  and the shower size. The unit of  $S_{1000}$  is vertical equivalent muon (VEM) defined as the detector response to a muon traveling vertically through the center of a SD station [63].

$$S(r) = S_{1000} \left( \frac{r}{1000 \text{ m}} \right) \cdot \left( \frac{r + 700 \text{ m}}{1700 \text{ m}} \right)^{\beta + \gamma} \quad (6.3)$$

- Stations that should hypothetically observe a signal but stayed silent are included in the fit using a likelihood method. An exemplary fit is shown in figure 6.3 for Event 39819479. The signal response function of the PMTs has been parameterized which allows to recover saturated stations by an extrapolation of the signal [208].

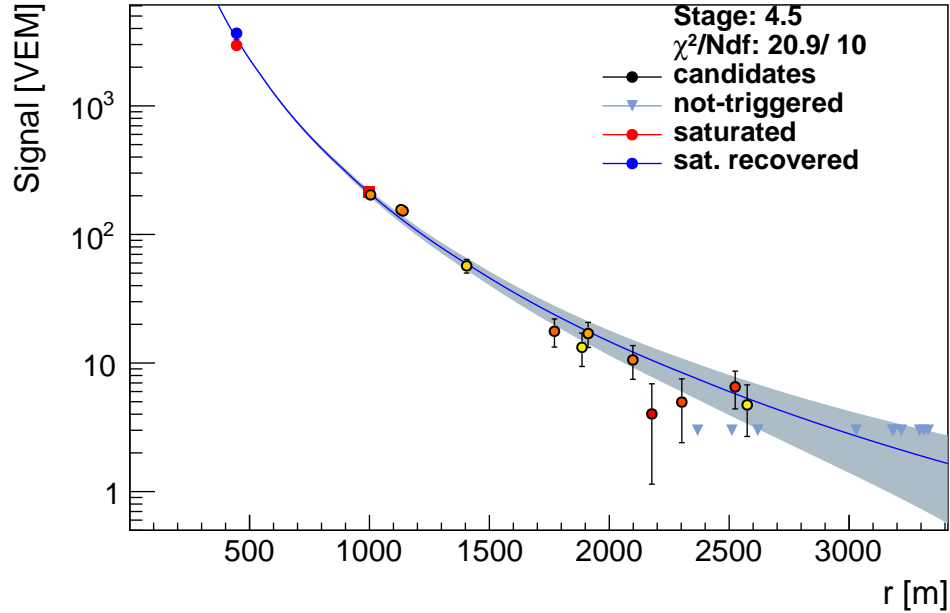


Figure 6.3: Measured VEM signal as a function of the distance to the reconstructed shower core. Saturated stations close to the shower core are recovered by extrapolating the PMT traces. The signal at around 2500 m distance from the shower is around 3 VEM where the stations have a 50% trigger chance [203].

- The shower axis and, correspondingly, the direction calculates to

$$\vec{a} = \frac{\vec{x}_0 - \vec{x}_{\text{gr}}}{\|\vec{x}_0 - \vec{x}_{\text{gr}}\|}. \quad (6.4)$$

The precision of the reconstruction depends on three aspects:

- the statistical effect of measuring only a limited number of particles of the shower,
- assumptions made in the LDF, especially the parameterizations of  $\beta$  and  $\gamma$  and
- the individual clock precision of the stations and the fluctuations when the first particle arrives (shower to shower fluctuations). This effect has been parameterized in a time variance model [209].

Combining all effects, the angular resolution for events with energies above 10 EeV is better than  $0.9^\circ$  and highly depends on the number of stations, see figure 6.4 [210].

### Energy reconstruction

The Pierre Auger Observatory has three methods to measure the energy of the cosmic rays. First, the most recent method is based on the radio emission of an extensive air shower, fundamental calculations of electrodynamics and the fact that the

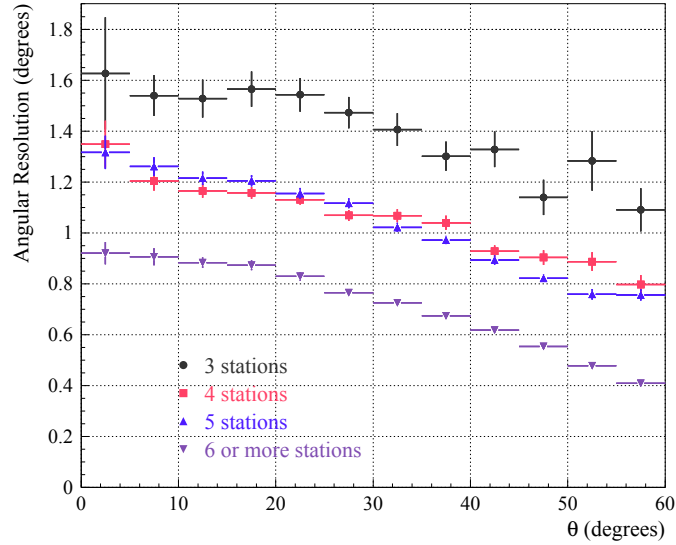


Figure 6.4: Angular resolution for events with more than 3 EeV and different multiplicities of triggered stations. A multiplicity of 3 corresponds to  $E < 4$  EeV, multiplicities of 4 and 5 are in an intermediate range of  $3 \text{ EeV} < E < 10 \text{ EeV}$  and 6 or more corresponds to  $E > 10 \text{ EeV}$ , taken from [209].

atmosphere is transparent to radio emission [36]. Second, the fluorescence telescopes allow a direct measurement of the energy  $E_{\text{FD}}$  by integrating the Gaisser-Hillas function describing the longitudinal profile of an air shower [25, 211] and correcting for different effects, e.g. attenuation due to aerosols, missing energies due to the muonic and neutrino component and Cherenkov radiation [212, 213]. Third, the energy measurement with the surface detector could in principle be achieved by the integration of the modified NKG-LDF. However, the lateral distribution is only sampled at discrete positions where SD stations are placed resulting in high fluctuations in the integral. To avoid this statistical effect, the signal strength  $S_{1000}$  is used to reconstruct the energy [214].

To further remove the effect of  $S_{1000}$  decreasing with the zenith angle  $\theta$  a constant integral intensity cut method [215] is applied, see equation (6.5) with  $x = \cos^2 \theta - \cos \theta$  and  $\theta = 38^\circ$  [39].

$$f_{\text{CIC}} = 1 + [0.980 \pm 0.004] \cdot x + [-1.68 \pm 0.01] \cdot x^2 + [-1.30 \pm 0.45] \cdot x^3 \quad (6.5)$$

It allows to calculate the hypothetical signal  $S_{38}$  at a zenith angle of  $\theta = 38^\circ$  and a distance  $r = 1000 \text{ m}$ . In figure 6.5 the correlation between the SD energy estimator  $S_{38}$  and the energy measured by the FD is shown for 11155 selected hybrid events with zenith angle  $\theta \leq 60^\circ$  [216]. The distance is the best choice from simulations and the zenith angle is the median measured value at the Pierre Auger observatory.

From the correlation  $E_{\text{FD}} = A \cdot (S_{38}/\text{VEM})^B$  and equation (6.5) the energy measured by the surface detector is calculated, see equation (6.6). The best fit values are  $A = (1.90 \pm 0.05) \cdot 10^{17} \text{ eV}$  and  $B = 1.025 \pm 0.007$ . This calibration of the energy measured

by the SD with the calorimetric energy from the FD allows a model independent measurement.

$$E_{\text{SD}} = A \cdot (S_{1000}/f_{\text{CIC}}(\theta)/\text{VEM})^B \quad (6.6)$$

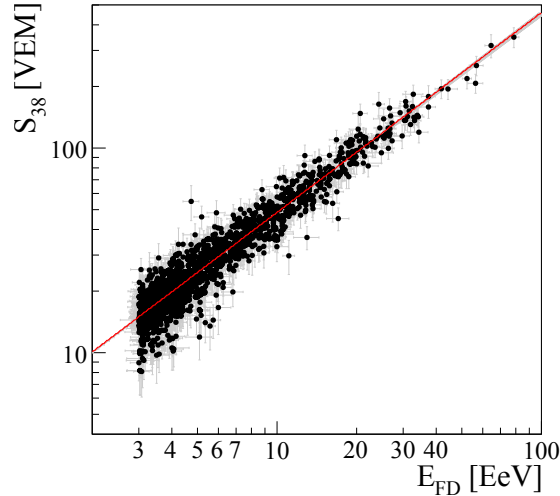


Figure 6.5: Correlation between  $S_{38}$  and  $E_{\text{FD}}$  for a selected set of hybrid events measured by FD and the SD array with a spacing of 1500 m. All events have a zenith angle  $\theta$  below  $60^\circ$ . The red line denotes the fitted function from equation (6.6), taken from [39].

The statistical uncertainty of the energy is defined as the fit error of the LDF, whereas the systematic uncertainty is dominated by the assumptions made in the LDF. Above 10 EeV the combined relative uncertainty is better than 10% and decreases with energy [63, 210].

In this thesis only vertical events are used which correspond to a zenith angle between  $0^\circ$  and  $60^\circ$ . For the energy reconstruction of horizontal events with zenith angles above  $60^\circ$  refer to [217, 218].

### 6.3 Data Selection

The final step after recording and reconstructing data is to select a data set suitable for the analysis one wants to perform. Anisotropy analyses typically depend strongly on the number of events and thus, use slightly more relaxed selection criteria as e.g. the measurement of the energy spectrum. Additionally, the analysis presented in the next two chapters uses simulations to adjust free parameters and to estimate its performance which makes a prior knowledge of the data set size essential.

*The remaining description in this section is part of the the publication “Observer Data Set for Anisotropy Studies including 4T5 events”[205]. Within the scope of this work, the event selection was verified by applying the individual selection cuts and checking the obtained distributions for consistency. Furthermore, the data set*

was compared to the set used in [5]. Additionally, the text of the above publication was essentially written by the author of this thesis.

We use data measured by the Pierre Auger Observatory from 1 January 2004 to 26 June 2017 (ICRC2017 data, v12r3) and reconstructed with the `Offline` software. In this period 5724946  $T4$  events have been recorded by the surface detector. To restrict the deflection in the galactic magnetic field to the ballistic regime, cosmic rays with energies above 6 EeV are taken into account, see [169].

The main two reasons for this constraint are on the one hand that the uncertainties in the coherent deflections of different galactic magnetic field models increase with decreasing rigidity. On the other hand, the average of the deflections increases up to  $90^\circ$  at the lowest rigidities which corresponds to a random walk.

Furthermore, we require that all events do not fall into a bad period and are not in coincidence with a lightning measured by the weather stations at the Observatory. Excluding bad periods is different to already published anisotropy studies [86, 219, 5]. There, it was argued that the number of triggered SD stations is large for events with energies above 20 EeV and thus a missing station does not have an impact on the reconstructed energy and direction. However, we select events above  $E_{\min} = 6$  EeV and consequently remove events measured during a bad period as missing stations affect the reconstruction at the lowest energies.

As the surface detector is fully efficient at energies above 3 EeV and zenith angles  $\theta < 60^\circ$  we further restrict the data set to this zenith range to avoid any biases in the exposure, see [203, 86]. The numbers of events passing the different cuts are summarized in table 6.1.

Cut	Number of events
$E_{\min} > 6$ EeV	77537
Not in bad period	75907
Not tagged as lightning	75896
$\theta < 60^\circ$	53308

Table 6.1: Number of events passing different quality cuts.

Additionally, we require that there are either 6 active stations in the hexagon around the hottest station after reconstruction (6T5) or more than 4 active stations and that the shower core falls into an active triangle (4T5 +  $\Delta$  or 5T5 +  $\Delta$ ). In the case of 4 and 5 active stations, the triangle condition has to be considered additionally to the number of active stations and is denoted by  $\Delta$ . Note that in previous analyses [5, 39, 219] events with only a 6T5 trigger prior to the reconstruction were taken into account. To avoid issues with bad silent stations we decided to use the trigger after the reconstruction which leads to a difference of 2 events.

Finally, the total number of events is  $36126$  (6T5) +  $7138$  (5T5 +  $\Delta$ ) +  $2713$  (4T5 +  $\Delta$ ). They are composed of 42326 events where the shower core is inside both triangles types, 2636 events with the shower core inside the isosceles triangles, 1008 events

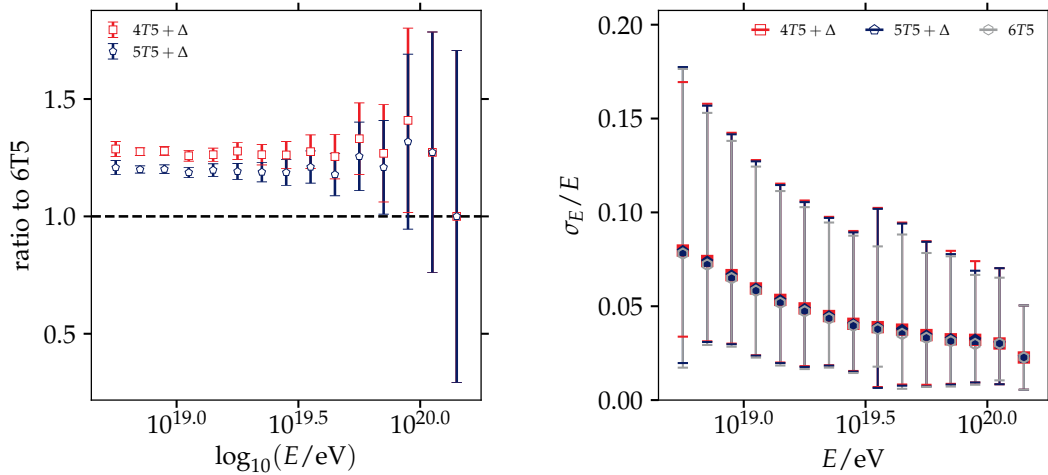


Figure 6.6: (left) Increase of the event numbers with respect to 6T5 events by adding 5T5 +  $\Delta$  (blue) or 5T5 +  $\Delta$  and 4T5 +  $\Delta$  events to the set. (right) Relative energy uncertainty where the markers denote the median of the data set and the error bars the most probable 68% quantile. In both figures the markers labeled by 4T5 +  $\Delta$  include all 6T5 and 5T5 +  $\Delta$ .

with the shower core inside the equilateral triangle and 7 events where the shower core is not contained in the hexagon. These events are 6T5 events where the shower core is just outside the hexagon around the hottest station. The gain of events is independent of the energy and shown in the left panel in figure 6.6.

The relative uncertainty on the energy is also unbiased as shown in the right panel of figure 6.6. The medians of the distributions lie on top of each other and the most probable 68% quantiles have the same size. The average of the relative energy uncertainty decreases from 8% at 6 EeV to 2% at 100 EeV.

In figure 6.7 the measured azimuth and zenith angles of the data set are shown as stacked histograms for the three different T5 trigger combinations. For both distributions no dependency on the T5 trigger is visible. Note that the zenith distribution is not proportional to  $\sin \theta$  as the detection efficiency depends on energy and  $\sin^2 \theta$  [219].

The distributions of galactic longitude  $\ell$  and latitude  $b$  are obtained by using the time information of the event additionally to the locally measured angles, see figure 6.8. The latitude distribution is not uniform as the the Pierre Auger Observatory is located in the southern hemisphere on Earth and thus can not observe events from the northern hemisphere as the galactic plane is tilted with respect to the equatorial plane. As the events categorized by the different triggers have the same dependencies on angles and energy we conclude that including 5T5 +  $\Delta$  and 4T5 +  $\Delta$  events does not lead to a bias in the data set.

Figure 6.9 shows the integral number of events above a given energy  $E_{\min}$ . The top  $x$  axis shows the maximum charge number  $Z_{\max}$  which can be used in an aniso-

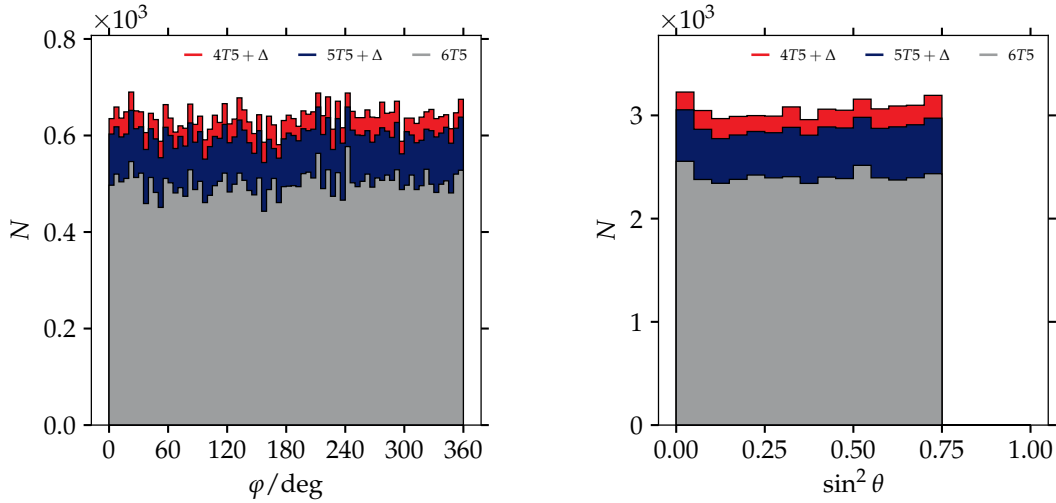


Figure 6.7: Stacked histograms of (left) azimuth and (right) zenith angles.

tropy analysis on small and intermediate scales including deflections in the galactic magnetic field [169]. The total number of selected events is 45977 and composed of events classified by different T5 triggers as described above.

The data set used for the comparison of arrival directions with those of selected starburst galaxies [5] was reconstructed with the Herald code and has 4396 events from 1 January 2004 to 30 April 2017 and contains events with energies above 20 EeV. In the same time period our selection has 4355 events of which 4116 are identical with the Herald reconstruction. The differences can be explained by the inclusion of bad periods in the Herald data set (90 events) and slightly different energy and directional reconstructions of both reconstruction codes.

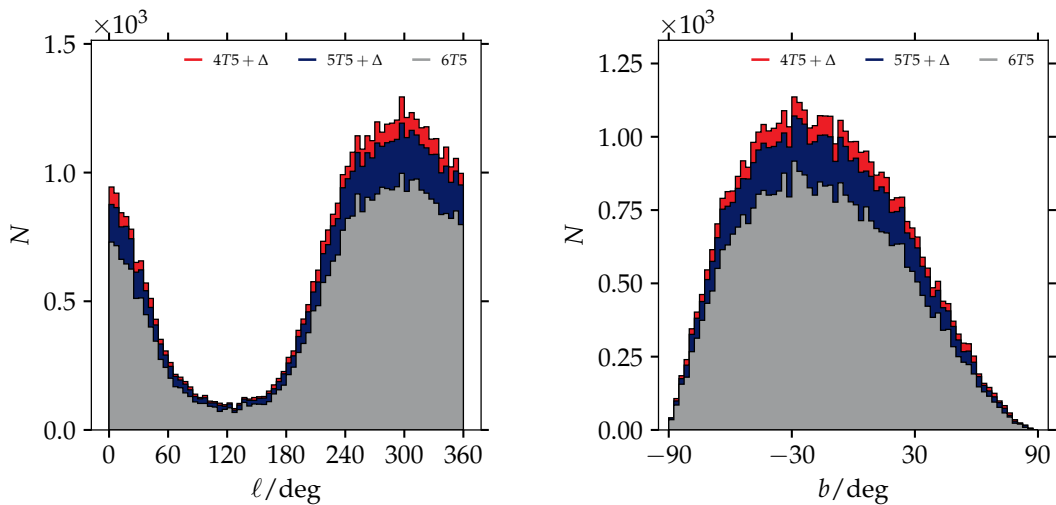


Figure 6.8: Stacked histograms of (left) longitude and (right) latitude angles.

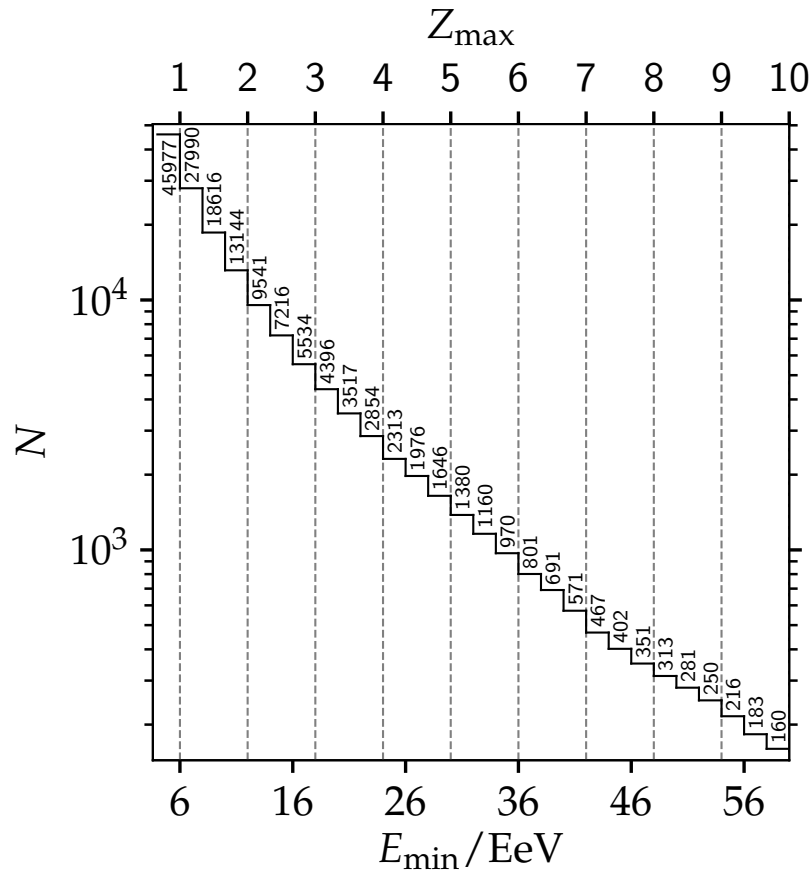


Figure 6.9: Integral number of events above different energies. The top axis denotes the maximum charge number usable in analyses taking into account models of the galactic magnetic field as they are not reliable below a rigidity  $R = E/Z = 6 \text{ EeV}$ , for more details see chapter 5.

# 7. Method of Searching for Local Structures in the Arrival Directions of Cosmic Rays

*The descriptions of this chapter are based on the prepublication with the title “A method of Searching for Origins of Cosmic Rays” presented on the International Cosmic Ray Conference (ICRC2017) [220] and the internal analysis publication of the Pierre Auger Collaboration with the title “Search for Local Structures in the Arrival Directions of Cosmic Rays using an Extragalactic Directional Filter Method” [221]. Especially the description of the filter in this introductory paragraphs and the section presenting the dependency on magnetic field uncertainties are partly direct citations (denoted by “[...]”), however more information was added to achieve a more detailed description. Additionally, some sentences were rephrased from writing in the “we-form” to a passive sentence structure, e.g. from “we investigated the distribution” to “The distribution was investigated”.*

This chapter describes an extragalactic filter method that allows to search for local structures in arrival directions of ultra-high energy cosmic rays (UHECRs). In chapter 5 it was shown that deflections in the galactic magnetic field (GMF) can be considered as the dominant effect in the propagation of UHECRs in our galaxy. Therefore, the natural frame for the search of local structures in the arrival directions of UHECRs is the direction before they are affected by the GMF.

The principle is first explained in a simplified way as it resembles a frequency filter applied between two Fourier transformations. This is depicted in the next paragraphs using the example of a radio trace  $r(t)$  containing a beacon signal.

“[...] The radio time trace contains various frequencies resulting from the beacon, galactic radio emissions etc, and thus appears to be a complicated looking superposition of many contributions. Obviously, the natural phase space for analysis is frequency. Fourier transformation of the radio trace as a function of time gives the frequency spectrum which exhibits the prominent signal of the beacon:

$$F(\omega) = \frac{1}{\sqrt{2\pi}} \int e^{-i\omega t} r(t) dt$$

When selecting a narrow frequency interval around the maximum - the beacon signal always stands out - we can perform the inverse Fourier transformation to receive the cleaned beacon signal in the time domain:

$$r_{\text{beacon}}(t) = \int e^{i\omega t} F(\omega_a < \omega < \omega_b) d\omega$$

The method of consecutive application of a Fourier transformation, a selection cut on a frequency regime which is followed by the inverse Fourier transformation represents the procedure of a frequency filter.

Note here two further aspects which will also be essential in the new directional filter method described below. Even if the frequency  $\omega$  used in the Fourier transformations above is detuned by, e.g.,  $\omega' = a\omega + b$  the resulting beacon trace  $r_{\text{beacon}}(t)$  in the time domain will not be greatly affected. This is a consequence of applying both the transformation and its inverse. Errors arising in the first transformation will be compensated when applying the inverse transformation.

Furthermore, if all relevant sources are turned off and only random noise remains in the radio time trace, no outstanding frequency can be filtered which can be quantified by performing corresponding statistical tests [...] [221].

In the analysis developed in this thesis, the measured cosmic rays are first transformed to the edge of the galaxy before applying a filter to identify high density regions as a second step. Here, the edge of the galaxy means a distance of 20 kpc from the galactic center where the influence of the galactic magnetic field is negligible. Finally, the predicted arrival directions of these regions on Earth are compared in a log-likelihood method to the measured UHECRs. The combination of backward- and forward transformation partly compensates the uncertainties analogous to the Fourier transformation between frequency and time domain.

This chapter is structured as follows. First, the simulation setup (section 7.1) is presented before explaining the different analysis steps from the backward transformation (section 7.2) over the search of outstanding directions (section 7.3) and the forward transformation (section 7.4) to the likelihood analysis (section 7.5). Afterwards, a grid search is performed to optimize free parameters (section 7.6) followed by a sensitivity estimation (section 7.7). Finally, the dependency on magnetic field uncertainties is investigated (section 7.8) and some technical details presented (section 7.9).

## 7.1 Simulation of astrophysical scenarios

The development of an analysis with multiple steps and parameters requires a carefully designed simulation setup that tries to represent the measured cosmic rays as close as possible. Here, the general picture consists of some amount of cosmic rays coming from some close by sources whereas the majority originates far away or from isotropically distributed sources and consequently forms a background. Consequently, such a Monte Carlo engine requires various different settings; the most important ones are shown in the following enumeration.

- The **energy spectrum**  $J(E)$  belongs to the best measured observables in astroparticle physics. It has been parameterized by a power law  $J(E) = J_0 (E/E_{\text{ankle}})^{-\gamma_1}$  below the ankle at  $E_{\text{ankle}} = 4.82 \text{ EeV}$  and a second power law modified by a suppression function [222].

$$J(E) = J_0 \left( \frac{E}{E_{\text{ankle}}} \right)^{\gamma_2} \left[ 1 + \left( \frac{E_{\text{ankle}}}{E_s} \right)^{\Delta\gamma} \right] \left[ 1 + \left( \frac{E}{E_s} \right)^{\Delta\gamma} \right]^{-1} \quad (7.1)$$

The different spectral indexes are by  $\gamma_1$  and  $\gamma_2$  and  $\Delta\gamma$  is responsible for an additional steepening of the spectrum after the suppression region. The normalization is denoted by  $J_0$  and at  $E_s$  the differential flux has fallen off “to one-half of the value of the power law extrapolation from the intermediate region” [222]. An alternative method consists of shuffling the measured energies and assigning them to the simulated cosmic rays. Using the same energy spectrum for the sources and background instead of the expected harder spectrum for the cosmic rays coming from the nearby sources is conservative approach which does not allow to identify the sources by their energy spectrum in the simulation. Note that the uncertainties on the energies of the individual cosmic rays are negligible compared to those of the galactic magnetic field.

- The **zenith angle** distribution is chosen according to the geometrical exposure of the Pierre Auger Observatory with a maximum zenith angle of  $60^\circ$  [204]. Some analyses looking for anisotropies in the arrival directions of cosmic rays use zenith angles up to  $80^\circ$  but for higher zenith angles a different modified lateral distribution function has to be used for the reconstruction of events, see also section 6.3.
- In general, the  $X_{\text{max}}$  measurements suggest an energy dependence of the **composition**, but these measurements are performed at lower energies with the fluorescence detector. At the highest energies the event rates are low and a reliable and unbiased reconstruction of  $X_{\text{max}}$  using the surface detector is currently under development. However, the composition of the simulated cosmic rays can be estimated by approximating the measured spectrum [97] with 15 % protons, 45 % helium and the remaining 40 % by an equal mixture of the carbon-nitrogen-oxygen (CNO) group [223], which is also used here.
- For the **galactic magnetic field** (GMF) the model from Pshirkov and Tinyakov with an axialsymmetric spiral field (PT11-ASS) was chosen. It is preferred over the bisymmetric (PT11-BSS) field as it better fits the rotation measurements. An alternative could be the model by Jansson and Farrar (JF12) but as the analysis method depends on a magnetic field model using two different fields allows to simulate uncertainties in the knowledge of the GMF. The idea of swapping both fields was discarded as it is preferred to perform the analysis with the currently best available model, the JF12 field model. The galactic magnetic field is used via magnetic field lenses described in section 5.2.2. They use the HEALPix pixelisation scheme with a resolution of  $1 \text{ deg}^2$ . This covers already the uncertainties on the measured latitude and longitude as they are

typically below  $1^\circ$ . The usage of the lenses allows to perform a parameterized simulation which is faster than propagating the individual cosmic rays with corresponding software, e.g. CRPropa3 [175].

- The **minimal energy** constrains the **number of events**, see also figure 6.9. It is a free parameter which is typically scanned in anisotropy analyses to achieve the best significance. In this work, however, it will be fixed during a performance scan as the analysis is restricted to limitations in the assumed galactic magnetic field model.
- The **number of sources** and their individual **angular uncertainties** arising from deflections in extragalactic magnetic fields and turbulent deflections in the galactic magnetic field are free parameters as no sources have been detected yet. In the following, different numbers of sources in the range from 2 to 10 in steps of 2 are tested. Additionally,  $3^\circ$ ,  $6^\circ$  and  $9^\circ$  will be used for the smearing angle independent of the rigidity. For more details we refer to section 4.2 and chapter 5.
- There are two possibilities for the choice of the **sources**. Either they can be selected from a catalog of candidates or distributed randomly on the sky. In the simulation study supporting this analysis the latter is preferred to reduce the directional bias.
- The **signal fraction** denotes the fraction of cosmic rays originating from the close by sources. It is a model parameter and can not directly derived from measurements. However, within this thesis a method has been developed to approximate the signal fraction from applications of the two-point autocorrelation to simulated cosmic ray data which is explained in the following paragraphs.

### Two-point autocorrelation

The two-point autocorrelation observable counts the number of cosmic ray pairs as a function of their distances  $\theta_{i,j} = \angle(\vec{x}_i, \vec{x}_j)$ . The comparison of the distribution as a function of the separation angle to isotropic simulations allows to detect if the arrival directions of cosmic rays have overdensities on local angular scales. Thus, on the one hand the observable allows to discover anisotropies at different scales and on the other hand is independent from any propagation model and additionally does also not require any catalog for comparison which makes its results robust. Consequently, the two-point autocorrelation and also some modifications have been used over several years within the Pierre Auger collaboration [198, 224, 225, 226, 227] but did never yield a significant deviation from the isotropic expectation. Figure 7.1 shows the most recent results with a deviation at the  $2.8\sigma$  level of local significance at  $5^\circ$  which corresponds to a p-value of  $2.5 \cdot 10^{-3}$ . For details on this analysis see the figure caption and [198].

Here, this deviation is used to adjust the signal fraction as a function of the minimal energy  $E_{\min}$ , the number of sources and their smearing. First, for a fixed number of

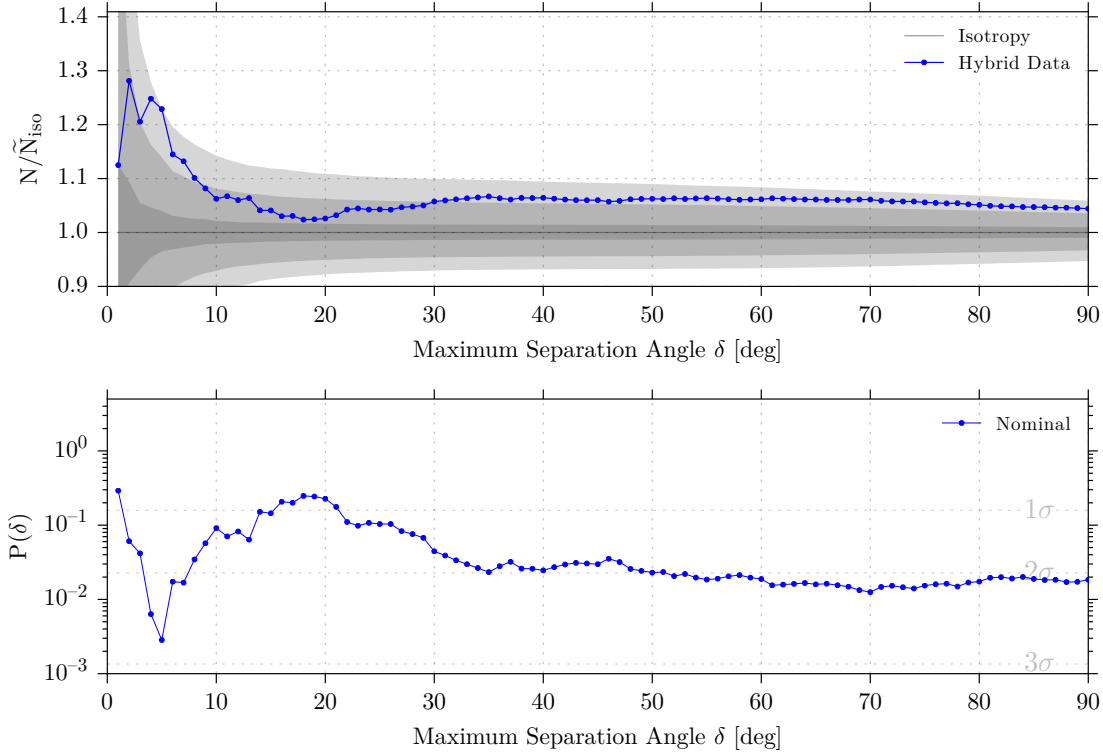


Figure 7.1: Two-point autocorrelation on hybrid data with energy  $E_{\text{min}} \geq 10$  EeV and an energy dependent cut on the slant atmospheric depth to select proton like events:  $X_{\text{max}} > 690 \text{ g/cm}^2 + 55 \text{ g/cm}^2 \cdot \log_{10}(E/\text{EeV})$ . (top) Number of correlating pairs as a function of the maximum separation angle normalized to the median value from  $10^5$  isotropic simulations. The gray bands denote the  $1\sigma$ ,  $2\sigma$  and  $3\sigma$  contours from the isotropic simulations. (bottom) Deviation from isotropic simulations as a function of the separation angle. The minimal p-value at  $\delta = 5^\circ$  corresponds to a standard deviation of  $2.8\sigma$ , taken from [198].

sources and different signal fractions and energies the median p-value is calculated for 100 simulations. An example with four signal fractions and four sources is shown on the left of figure 7.2. To estimate the value where the curves cross the  $2.8\sigma$  line for each energy the closest point below and above is selected. They are shown by the gray markers on the right of figure 7.2 whereas the black markers are constructed by a linear interpolation between those two values.

In a next step the logistic function from equation (7.2) is assumed to describe the signal fraction. It is motivated by the assumption that the transition between a signal fraction of almost 0 and in maximum 1 is smooth and has only one inflection point.

$$f_{\text{sig}} = \frac{1}{1 + e^{-k(E_{\text{min}} - x_0)}} \quad (7.2)$$

The function has two parameters, the steepness  $k$  and the inflection point  $x_0$  which denotes the energy where the signal fraction is equal to 0.5. The fit results are shown

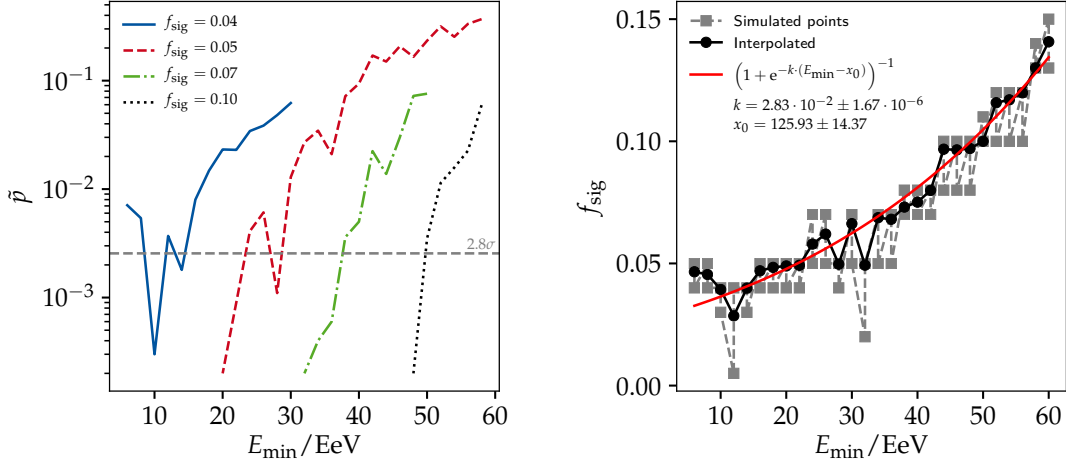


Figure 7.2: Demonstration for the construction of the signal fraction in this example for 4 sources with a smearing of  $3^\circ$ . (left) Median  $p$  value as a function of the threshold energy  $E_{\min}$  for different signal fractions. (right) Fit of the signal fraction to achieve a median significance in the two-point auto-correlation of  $2.8\sigma$ . For details see the corresponding description in the text.

for  $E_{\min} = 12 \text{ EeV}$  in figure 7.3 and for various simulation configurations table 7.1. In general a higher smearing of the source distribution allows for a larger signal fraction which manifests itself in the fact that the inflection point is found at lower energies and consequently the slope is slightly steeper in most cases. The uncertainty  $\sigma_{x_0}$  is dominating which is caused by the fact that  $x_0$  lies outside the simulated range. The same reason holds also for the fact, that  $\sigma_{x_0}$  becomes smaller the closer  $x_0$  gets to the simulated energy range. A further simplification by fitting the parameters as a function of the number of sources and their smearing was refrained from in order not to further increase the overall uncertainty on the signal fraction.

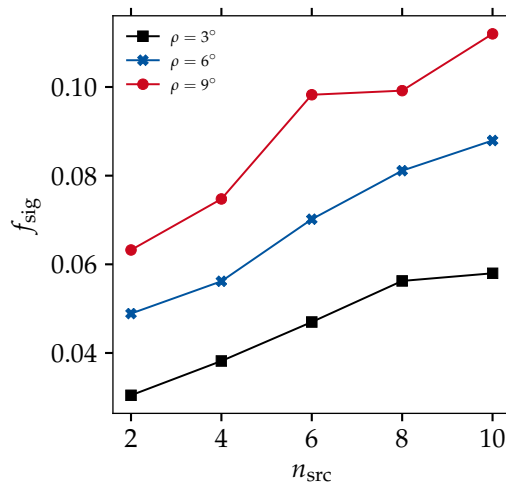


Figure 7.3: Signal fractions at  $E_{\min} = 12 \text{ EeV}$  as function of the numbers of sources.

		$(x_0 \pm \sigma_{x_0})/\text{EeV}$	$(k \pm \sigma_k)/10^{-2}$
2 sources	$\rho = 3^\circ$	$133 \pm 41$	$2.86 \pm 4 \cdot 10^{-4}$
	$\rho = 6^\circ$	$124 \pm 58$	$2.65 \pm 6 \cdot 10^{-4}$
	$\rho = 9^\circ$	$104 \pm 44$	$2.93 \pm 1 \cdot 10^{-3}$
4 sources	$\rho = 3^\circ$	$126 \pm 14$	$2.83 \pm 2 \cdot 10^{-4}$
	$\rho = 6^\circ$	$107 \pm 38$	$2.97 \pm 4 \cdot 10^{-4}$
	$\rho = 9^\circ$	$86 \pm 4$	$3.40 \pm 2 \cdot 10^{-4}$
6 sources	$\rho = 3^\circ$	$113 \pm 10$	$2.98 \pm 2 \cdot 10^{-4}$
	$\rho = 6^\circ$	$92 \pm 5$	$3.23 \pm 2 \cdot 10^{-4}$
	$\rho = 9^\circ$	$80 \pm 8$	$3.26 \pm 5 \cdot 10^{-4}$
8 sources	$\rho = 3^\circ$	$106 \pm 16$	$3.00 \pm 4 \cdot 10^{-4}$
	$\rho = 6^\circ$	$86 \pm 4$	$3.28 \pm 2 \cdot 10^{-4}$
	$\rho = 9^\circ$	$68 \pm 3$	$3.94 \pm 5 \cdot 10^{-4}$
10 sources	$\rho = 3^\circ$	$97 \pm 12$	$3.28 \pm 5 \cdot 10^{-4}$
	$\rho = 6^\circ$	$80 \pm 4$	$3.44 \pm 3 \cdot 10^{-4}$
	$\rho = 9^\circ$	$63 \pm 1$	$4.06 \pm 3 \cdot 10^{-4}$

Table 7.1: Best fit parameters of the signal fraction parameterizations by a logistic function. The inflection point  $x_0$  decreases with both the number of sources and the smearing of the sources. Both uncertainties show the fit uncertainty.

### Exemplary simulation setup

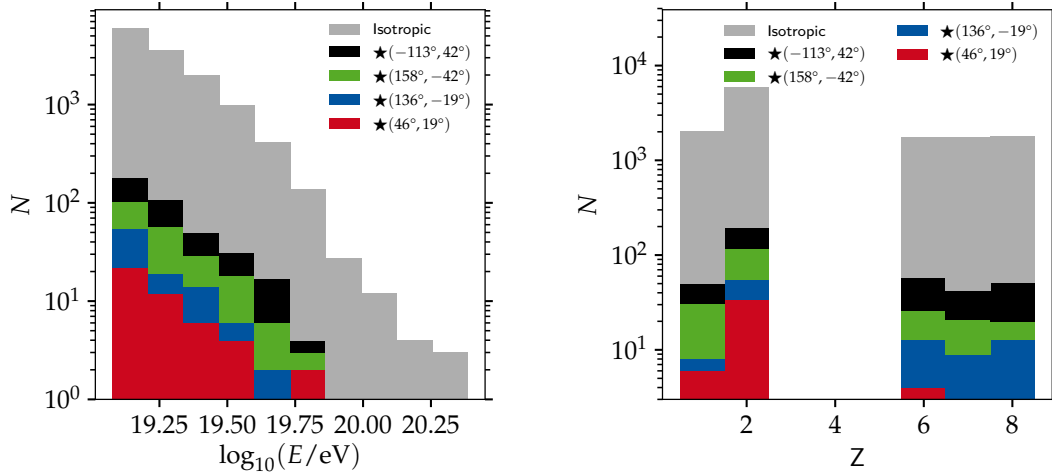


Figure 7.4: Simulated energy and charge spectra in stacked histograms. The minimal energy is set to 12 EeV and the energy spectrum follows equation (7.1). The colored histograms describe the 500 ( $f_{\text{sig}} = 3.8\%$ ) cosmic rays coming from the sources whereas the gray histogram denotes the dominating background. The coordinates  $(l, b)$  of the sources are also given in the legend.

Figures 7.4 and 7.5 show an exemplary set of simulated cosmic rays with 4 sources smeared by  $3^\circ$ , a minimal energy  $E_{\min} = 12 \text{ EeV}$  corresponding to 13144 events, see 6.9 and a signal fraction of 3.8% calculated with equation (7.2). The energy spectrum is shown on the left of figure 7.4 as a stacked histogram. In this simulation, the highest energetic events are only background events which is a difference to the usual assumed model that those particles point back to the sources as their deflection angles are small [228]. As already mentioned before, this approach is conservative, as the sources do not already stand out because of their energy spectrum. Furthermore, it is assumed that all near sources exhibit the same spectrum which would mean that their acceleration processes are the same [87].

The charge distribution is shown on the right of figure 7.4 as a stacked histogram. Here, a similar model as for the energy spectra is chosen as all cosmic rays share the same charge distribution. Note, the minimal simulated rigidity for this simulation is  $R_{\min} = E_{\min}/Z_{\max} = 12 \text{ EeV}/8e = 1.5 \text{ EV}$ .

The star symbols in figure 7.5 denote the directions of the sources in galactic coordinates and the circular markers the directions of the simulated cosmic rays. Here, a gray marker indicates a background cosmic ray, whereas the color code indicates the rigidity of the signal particles. Although one source is placed outside the exposure of the Pierre Auger Observatory, its cosmic rays are visible due to their large deflections. Most of the sources have elongated deflection patterns ranging over more than  $50^\circ$  and cosmic rays at the lowest rigidities are typically observed with the largest angular distance to their source.

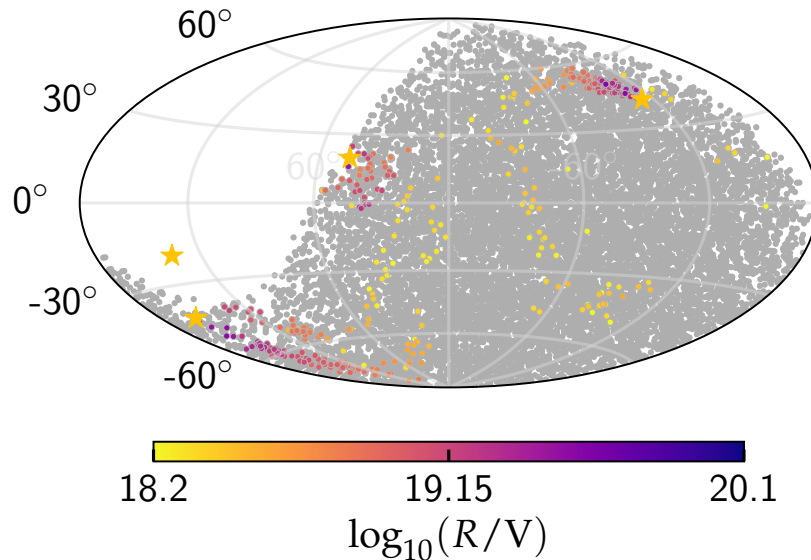


Figure 7.5: Simulated arrival directions for the exemplary set with 4 sources,  $f_{\text{sig}} = 3.8\%$  and  $E_{\min} = 12 \text{ EeV}$ . The color code indicates the rigidity of the signal cosmic rays.

## 7.2 Backward Transformation of Cosmic Rays through the Galactic Magnetic Field

The first step of the presented method consists of transforming the arrival directions of cosmic rays back to the edge of the galaxy. This is achieved by using magnetic field lenses [175, 195] derived from the regular field of the JF12 parameterization [79], see also subsection 5.2.2. They describe deflections of cosmic rays with energy  $E$ , charge  $Z$  combined to the rigidity  $R = E/Z$  and arrival direction  $l', b'$  at the edge of the galaxy on their path to Earth by transformations

$$g(l', b', E/Z). \quad (7.3)$$

This can be written in vector notation with  $\vec{m}_{\text{Earth}}$  and  $\vec{m}_{\text{gal}}$  being the arrival directions on Earth and the edge of the galaxy respectively, see equation (7.4). Here,  $n_{\text{pix}} = 49152$  is the number of pixels in the HEALPix [196] pixelisation scheme which is used to subdivide the surface of a sphere into equal areas. In this case each pixel has a size of  $\sim 1 \text{ deg}^2$ .

$$\vec{m}_{\text{Earth}} = \begin{pmatrix} g_{1,1} & \cdots & g_{1,n_{\text{pix}}} \\ \vdots & & \vdots \\ g_{n_{\text{pix}},1} & \cdots & g_{n_{\text{pix}},n_{\text{pix}}} \end{pmatrix} \cdot \vec{m}_{\text{gal}} \quad (7.4)$$

By construction these matrices describe the probability to observe a cosmic ray with extragalactic direction  $l', b'$  on Earth at direction  $l, b$ . In general, the matrices cannot be inverted, which also results from the fact that there are extragalactic directions that cannot be observed, see figure 5.11. Mathematically, this means that the matrix has a zero row and therefore does not have a full rank, which is a prerequisite for invertibility. However, a backward transformation can be performed by transposing equation (7.3) which describes the probability that a cosmic ray observed at a direction  $l, b$  on Earth originates from a direction  $l', b'$  at the edge of the galaxy:  $g^T(l, b, E/Z)$ .

Charges of the cosmic rays can not be measured directly, in a best case they could be estimated from the slant atmospheric depth  $X_{\text{max}}$  but current methods are affected by huge uncertainties [223]. Therefore, the charges of the UHECRs are assumed to be uniformly distributed between “[...]  $1 \leq Z \leq Z_{\text{max}}$  with  $Z \in \mathbb{R}$  in this analysis, so that each particle induces a corridor of probable directions in the map outside our Galaxy [as shown in figure 7.6]. The value  $Z_{\text{max}}$  depends on the cosmic-ray energy and ensures ballistic deflections in the galactic field. For this, cosmic-ray rigidities need to be above  $R = E/Z = 6 \cdot 10^{18} \text{ eV}$  [169]. Note that deflections in the magnetic field depend on rigidity  $R$ . Owing to the inverse relation of rigidity and charge, the choice of a uniform distribution in composition, respective charge  $Z$ , corresponds to a non-uniform distribution in rigidity  $R$ . Thus, this influences the density distributions in extragalactic directions. [...]” [221] Note that the analysis method allows a flexible choice of the probability density  $p_i(Z)$  for each cosmic ray and thus provides opportunities to include improved measurement results after a

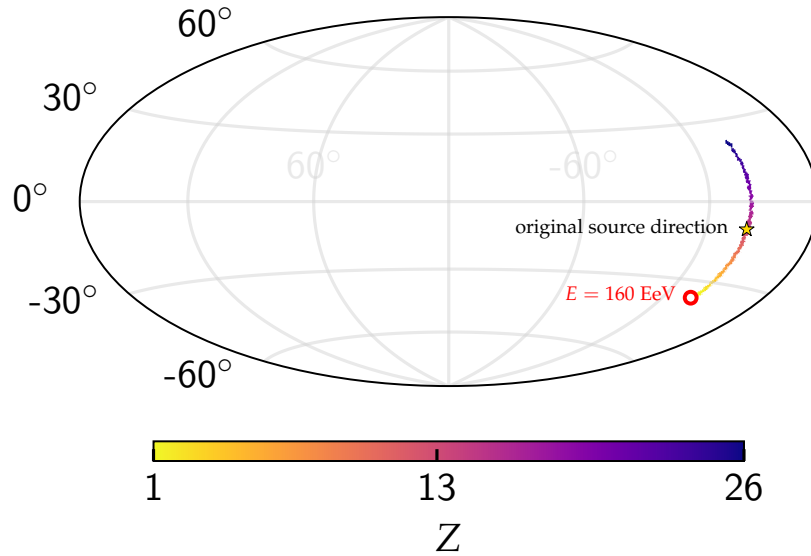


Figure 7.6: Backward transformation of a cosmic ray with  $E = 160$  EeV in the JF12 field model. The original source direction is denoted by the yellow star, the directions at the edge of the galaxy are color coded as a function of the assumed continuous charge.

detector upgrade of the Pierre Auger Observatory [49]. Due to the binning of the magnetic field lenses the probability density is also binned and it holds  $\sum p_i Z = 1$ .

The map at the top part of figure 7.7 shows the superposition of all corridors for all cosmic rays and all rigidities  $\sum_R x_{\text{data}}(R)$ . Here,  $x_{\text{data}}(R)$  denotes the values of all cosmic rays from the signal set in a given direction after the back transformation in contrast to the later used  $x(R)$  which is applied to an isotropic set. Throughout this and the following sections, the analysis is applied to the same scenario as described before e.g. in figures 7.4 and 7.5. Note that the rigidities are binned with a bin width of  $\Delta \log_{10}(R/V) = 0.02$  due to the usage of magnetic field lenses. The white areas in the northern hemisphere denote regions where the probability is exactly zero as these regions can not be reached by any cosmic ray. The clear maxima in the distribution are due to the variations of the galactic magnetic field. Both fields are also visible for the back transformation of isotropic arrival directions from the exposure of the Pierre Auger Observatory.

“[...] In order to filter extragalactic directions beyond trivial expectations, [...] the expected distribution from transformations  $g^T$  of isotropic arrival scenarios on Earth is determined in every pixel. All simulations of isotropic scenarios follow the exposure and the measured energy spectrum of the Pierre Auger observatory. [...]” [221] as described in section 7.1. Two exemplary distributions are shown in the lower part of figure 7.7 for 100 isotropic simulations. The distribution on the left describes the situation for a typical pixel where the distribution of the simulated data set is compatible with the background expectation. At the right hand side the difference between the isotropic expectation and the found value is clearly visible. Comparing

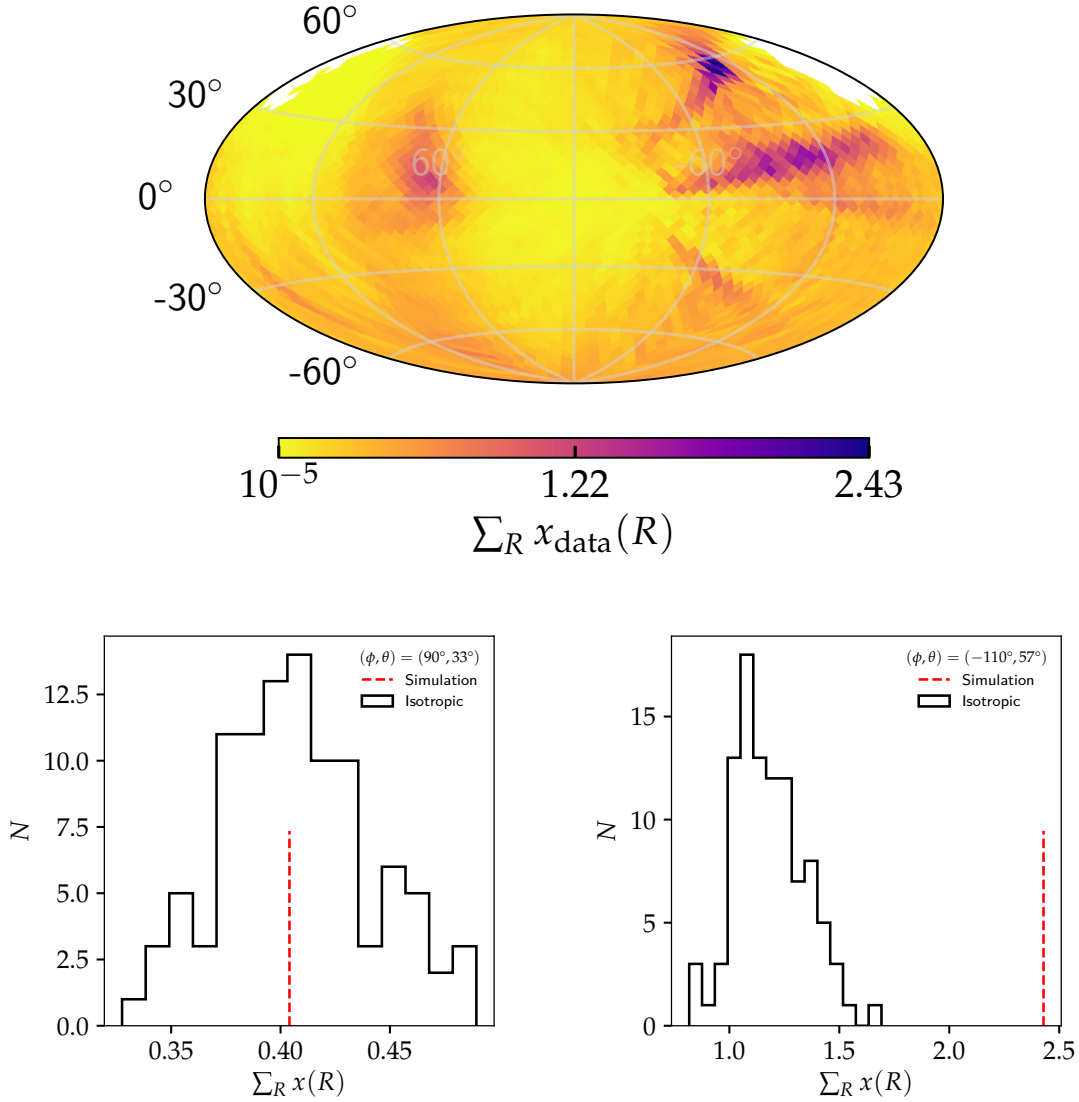


Figure 7.7: Backward transformation through the galactic magnetic field. (Top) superimposed corridors of all cosmic rays and all rigidities corresponding to the simulated astrophysical scenario in figure 7.5. (lower figures) Probability distributions at two directions given by the corresponding HEALPix pixels of 100 backward transformed isotropic simulations. The red line denotes the value of the simulated astrophysical scenario. For a detailed description refer to the text.

both distributions, it becomes apparent that the comparison to the isotropic expectation is required in each individual HEALPix cell as both distributions have different shapes and maxima. This does also not allow a parameterized approach using e.g. a multinomial distribution and requires the simulation of isotropic sets. In order to keep the simulation expense under control the angular resolution was decreased to  $8.4^\circ)^2$ . This corresponds to 3072 pixels with a maximum radius of 0.07 rad.

### 7.3 Search for Outstanding Extragalactic Directions

The method presented here aims at finding regions spreading over several pixels that show a significant deviation from the isotropic expectation. This deviation is estimated using the survival function of the simulated isotropic distributions for each pixel as exemplary shown in the lower part of figure 7.7. Note, that in cases where no value of the isotropic distribution exceeds the simulation, e.g. on the right side in figure 7.7, the p-value is set to 0.01 which corresponds to a deviation of  $2.33\sigma$  as there were only 100 isotropic sets simulated to reduce the computational expense.

Figure 7.8 shows the deviation as a function of the different extragalactic search regions. Pixels with a p-value above 0.5 are removed as they do not show an increased signal but on the contrary an underfluctuation which is not expected by the presence of a source. To further suppress isotropic upward fluctuations, a signal is required to exceed the 90 % quantile of the isotropic distribution; pixels below this value are shown in gray. The yellow circular markers represent the centers of clusters found by the DBSCAN (Density Based Spatial Clustering of Applications with Noise) algorithm [229].

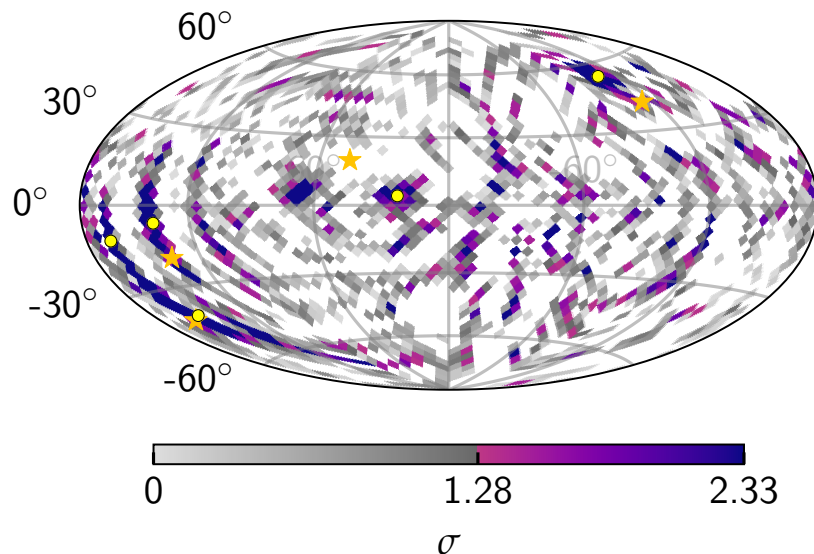


Figure 7.8: Outstanding directions filtered by the DBSCAN algorithm applied to the significance map produced by comparing with 100 isotropic sets. The underlying scenario is the same as in section 7.1.

The algorithm was selected as it meets all the requirements for the search of clusters.

- The search must be fully automatic and it should provide the same results independent of the order of the input.

- The algorithm must be capable of finding outstanding regions without knowing the number of regions. This excludes many hierarchical clustering algorithms and also methods based on the famous K-Means algorithm [230, 231], e.g. spectral clustering [232, 233].
- The shapes of the outstanding regions are not known on beforehand, thus all algorithms using predefined shapes can not be used.
- Not all directions correspond to an outstanding direction as visible in figure 7.8. Consequently, the algorithm must be able to handle noise.
- Typically, clustering methods require a distance measure which must be in this case the haversine metrics describing the great circle distance between two points on a unit sphere. This excludes most of the algorithms used in high energy physics to find jets in a detector signature. The only method in the normally used FastJet library [234] supporting the haversine metrics is the SISConc algorithm [235]. However, this algorithm is tuned to find jets vertical to the beam axis and does not perform well close to the beam axis which translates to the poles in this case.

The DBSCAN algorithm has two hyperparameters used to classify all points either as core point, directly reachable point or not reachable point as shown in figure 7.9.

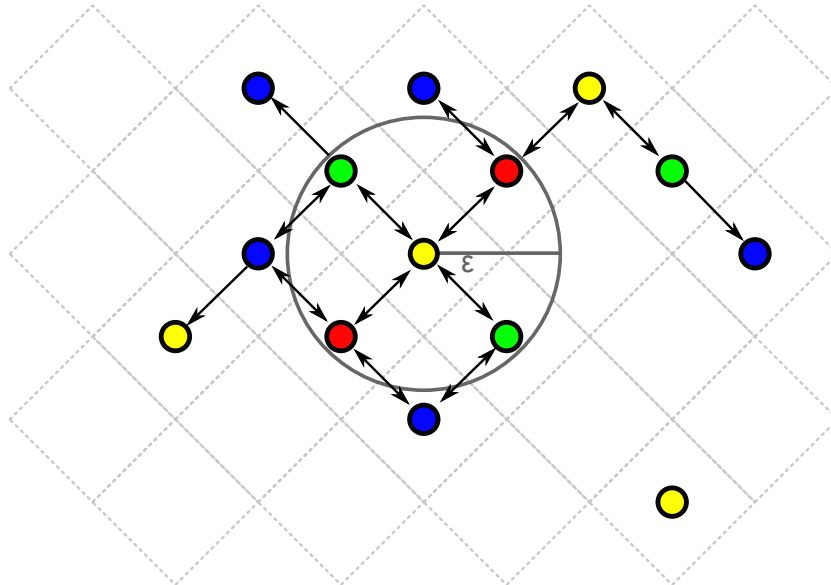


Figure 7.9: Schematic view of the DBSCAN algorithm. The gray squares in the background denote the shape of the pixels, the colored dots are the respective pixel centers. The colors blue, green, yellow and red correspond to pixel values of  $1\sigma$  to  $4\sigma$ . The circle marks the size of the  $\varepsilon$  environment around a point, the arrows with a single head point to a reachable point, the arrows with two heads denote cluster center points assuming a required sum of  $\Sigma\sigma = 5$ . The point in the bottom right is an unreachable point.

This figure shows a zoom into a back transformed map with pixels denoted as squares and their respective values denoted by the color code. The first parameter  $\epsilon$  defines the neighborhood of each point whereas the second parameter  $\Sigma\sigma$  is the minimal weight which must be contained inside the  $\epsilon$ -environment around a point to classify it as core point. Points that are within an  $\epsilon$  environment of a core point but are not themselves a core point are reachable points. The category of not reachable points describes noise points. In the construction of clusters neighboring core points are connected to each other as denoted by the arrows with two heads in figure 7.9. Thus, large values of  $\epsilon$  lead to few or in worst case only a single cluster whereas small values might result in many small clusters or no clusters depending on the choice of  $\Sigma\sigma$ . Larger values of  $\Sigma\sigma$  are better suited to suppress background, but have the disadvantage that eventually no clusters could be found. Note that the implementation of the DBSCAN within the software library scikit-learn is used [236].

In a next step the centers of mass of all filtered clusters are used as source candidates, they will further be denoted by  $\mathcal{F}$ . Note that if “[...] the cosmic rays are matter particles with positive charges, the source direction may rather be close to one of the edges of the elongated cluster and not in the cluster center. Thus with the choice of the cluster center, no bias is introduced concerning either the field direction or cosmic matter and antimatter.[...]” [221] Both particle type hypotheses can be tested with the corresponding choice of the magnetic field lenses which are either constructed for matter or antimatter.

In figure 7.8 it becomes apparent that the algorithm is capable of finding the correct source directions, however it typically filters thread like structures around the simulated direction. Additionally, the back transformed map is affected from the differences in the galactic magnetic field models used for simulation and analysis.

## 7.4 Forward Transformation through the Galactic Magnetic Field

“[...]The above-explained cleaning for trivial contributions in the extragalactic directional distribution, and selecting directions with overdensities was the step which corresponds to the frequency filtering of the Fourier transformation example. In the following we use only the filtered directions  $\mathcal{F}$  to evaluate regions of local structures on Earth by forward transformations with the field lens  $g(l', b', E/Z)$ . [...]” [221] The complete transformation also includes the exposure  $\mathcal{E}$  of the Pierre Auger observatory, see equation (7.5). Additionally, a Gaussian smearing around the filtered extragalactic directions  $\mathcal{F}$  with parameter  $\delta$  is introduced. The value of  $\delta$  is fitted analogous to [5] using the likelihood method described in section 7.5.

$$S_\delta(l, b, E/Z) = \mathcal{E} \times g(l, b, E/Z) \times \mathcal{F}(\delta) \quad (7.5)$$

Figure 7.10 shows the forward transformed signal distributions  $S_\delta(l, b, E, Z)$  for two different rigidities and a smearing of  $\delta = 3^\circ$ . At the lower rigidity of  $R = 6$  EV the transformations have a large angular distance to the initially filtered extragalactic

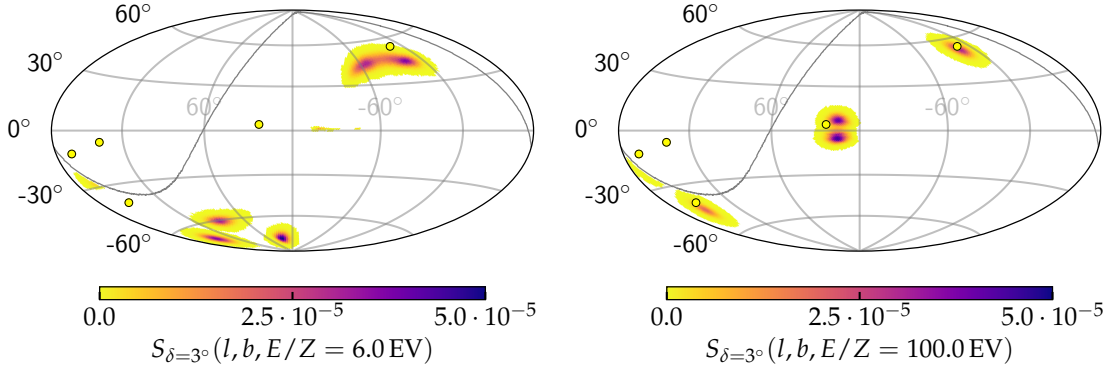


Figure 7.10: Forward transformed signal contribution for a rigidity of (left)  $R = 6$  EeV and (right)  $R = 100$  EeV. The gray line denotes the transition where the exposure of the Pierre Auger Observatory drops to zero.

directions  $F(\delta)$ . For  $R = 100$  EV the distributions have a smaller angular distance, however structures like multiple images are clearly visible. One source candidate barely contributes to  $S_\delta(l, b, E, Z)$  since the exposure strongly suppresses it or acts like a cut.

## 7.5 Likelihood Test of Corridors in the Cosmic Ray Arrival Directions on Earth

To evaluate the key question “[...]how well can the observed cosmic rays be described when forward tracking cosmic rays through the galactic magnetic field from these filtered directions[...]” [221] a standard log-likelihood method is used. The log-likelihood  $\ln \mathcal{L}$  sums over all cosmic rays  $i$  with measured arrival directions  $l_i, b_i$  and energies  $E_i$ , see equation (7.6). Furthermore, the initially assumed probability distribution  $p_i(Z)$  for the continuous charges  $Z \in \mathbb{R}$  has to be taken into account for each cosmic ray, see also section 7.2. Note that the charge probability distribution  $p_i(Z)$  is binned due to the rigidity binning of the lenses allowing to use the discrete sum  $\sum_{Z_j=1}^{Z_{\max,i}} p_i(Z_j) = 1$  instead of the continuous integral  $\int_{Z_j=1}^{Z_{\max,i}} \frac{dp_i(z)}{dz} dz = 1$ .

$$\ln \mathcal{L} = \sum_{i \in \text{CRs}} \left[ f \left( \sum_{Z_j=1}^{Z_{\max,i}} S_\delta(l_i, b_i, E_i/Z_j) \cdot p_i(Z_j) \right) + (1-f)B(l_i, b_i) \right] \quad (7.6)$$

“[...] Here,  $f$  denotes the relative proportion of the measured particles assigned to the extragalactic cluster directions.  $B$  denotes the trivial directions that follow the exposure of the Pierre Auger Observatory. [...]” [221] Note, the upper charge limit  $Z_{\max,i}$  is set individually for each cosmic ray to restrict cosmic-ray rigidities to be above  $R = 6$  EeV to ensure ballistic deflections.

Figure 7.11 shows the distribution of the test statistic  $t = \ln \mathcal{L} - \ln \mathcal{L}(f = 0)$  as a function of the two free parameters  $f$  and  $\delta$  for the simulation from section 7.1.

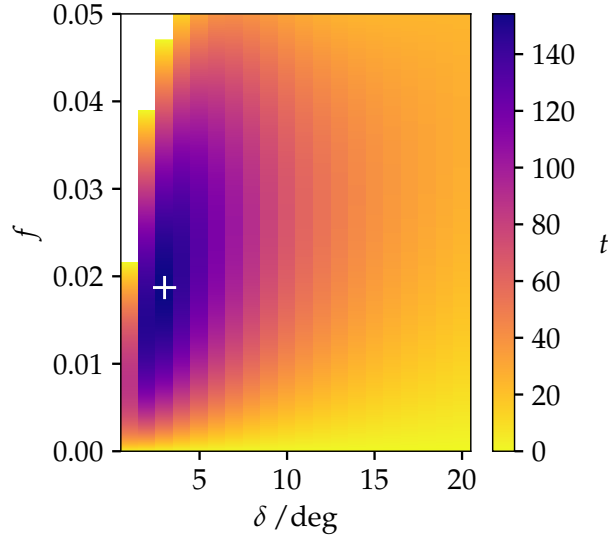


Figure 7.11: Test statistic  $t = \ln \mathcal{L} - \ln \mathcal{L}(f = 0)$  as function of the parameters of the likelihood fit with the likelihood from equation (7.6). For details refer to the text.

The white cross represents the best fit values with a smearing of  $\delta_{\text{bf}} = 3^\circ$  and an anticipated signal fraction of  $f_{\text{bf}} = 1.9\%$ . The initial smearing of the simulation is fitted perfectly, however the signal fraction is slightly underestimated. This is due to the fact that the difference between the simulated and the applied GMF model does not allow to capture all signal cosmic rays.

“[...]In order to claim local structures in the arrival directions beyond trivial configurations, comparison to simulated isotropic data sets is required[...]” [221] This is also done in the next section to optimize the free parameters of the analysis.

## 7.6 Optimization of Free Parameters

The analysis method has three free parameters that must be optimized on simulation to obtain the best significance to claim local structures in the arrival directions of UHECRs:

- the minimal energy  $E_{\text{min}}$  having the largest impact via the number of events,
- the neighborhood parameter  $\varepsilon$  of the clustering algorithm and
- the minimal weight  $\Sigma\sigma$  defining a core point in the clustering algorithm.

For each minimal energy at least 2000 isotropic and 100 signal sets with various source numbers  $N_{\text{src}} \in [2, \dots, 10]$  are simulated. As no sources have been detected yet for UHECRs the directions of the sources are chosen randomly from the 48 directions of the second lowest HEALPix scheme ( $n_{\text{side}} = 2$ ). The smearing angles

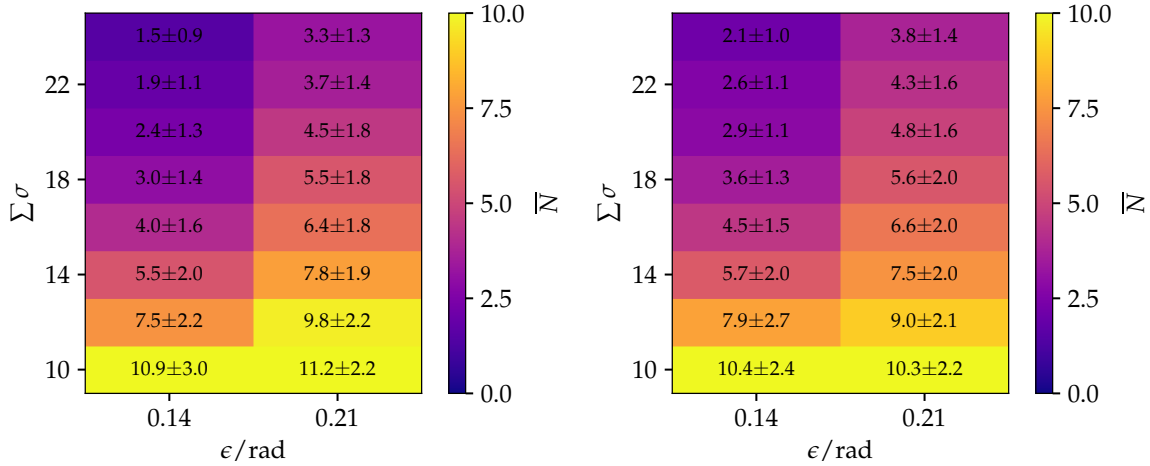


Figure 7.12: Mean number  $\bar{N}$  and its standard deviation of filtered extragalactic regions using different configurations of the cluster algorithm for (left)  $E_{\min} = 6 \text{ EeV}$  and (right)  $E_{\min} = 12 \text{ EeV}$ . The number decreases when the minimal required size  $\Sigma\sigma$  increases as less clusters can fulfill this requirement. For a search radius  $\epsilon = 0.21 \text{ rad}$  the number of filtered regions is slightly higher than for  $\epsilon = 0.14 \text{ rad}$ . The dependency of the number of filtered regions on the energy is negligible compared to the dependency on the parameters of the cluster algorithm.

$3^\circ$ ,  $6^\circ$  and  $9^\circ$  are taken into account for this study. For all figures of this section, the signal simulations contain 4 sources with an initial smearing of  $3^\circ$  before being propagated through the PT11-ASS GMF model. The magnetic field in the analysis for the backward- and forward transformation is always the JF12 GMF model to account for the uncertainties of the GMF.

The influence of the DBSCAN parameters on the mean number of filtered extragalactic regions is shown in figure 7.12 for  $E_{\min} = 6 \text{ EeV}$  and  $E_{\min} = 12 \text{ EeV}$ . The two values of the neighborhood parameter are adjusted to the size of the pixels of the back transformed map. The value  $\epsilon = 0.14 \text{ rad}$  includes the 4 neighboring pixels sharing a pixel border with a central pixel, whereas  $\epsilon = 0.21 \text{ rad}$  includes a complete ring of pixels around the central pixel by additionally considering neighbors defined by touching corners, see also figure 7.9. The use of larger values was omitted, since the covered angle then becomes so large that potentially expected structures can no longer be resolved, see section 4.2. Testing intermediate values does not yield any difference due to the pixelisation of the back transformed map. For the cluster parameter  $\Sigma\sigma$ , a step size of  $\Delta\Sigma\sigma = 2$  was chosen to minimize the simulation effort. A first analysis showed that values  $\Sigma\sigma < 10$  typically accept too much background whereas for values  $\Sigma\sigma > 24$  often no region could be filtered.

The probability to filter no corridor  $P(N_{\text{candidates}} = 0)$  is shown in figure 7.13 for signal and isotropic simulations. The probability is calculated by counting the number of simulations without filtered region out of  $\sim 2000$  simulations for each configuration of the parameters. In the case of isotropic simulations, it raises fast for

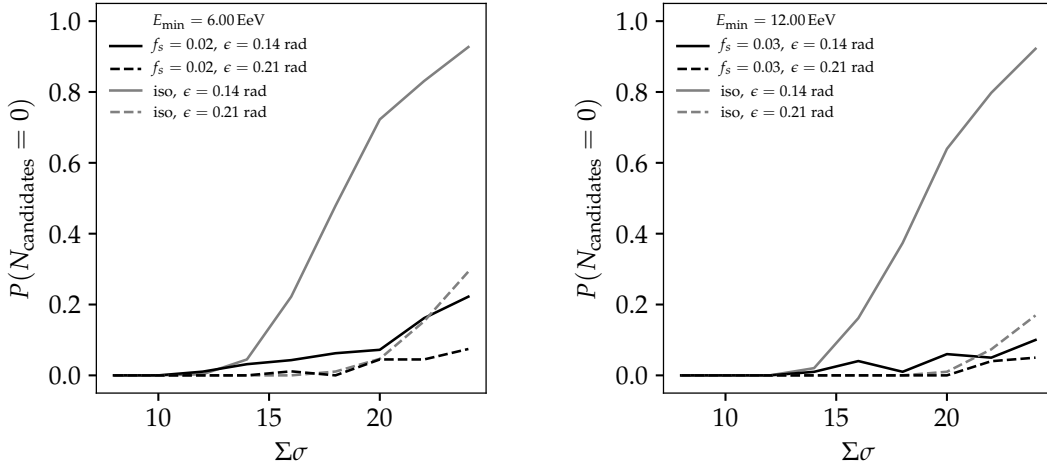


Figure 7.13: Probabilities to detect no outstanding region for (left) 6 EeV and (right) 12 EeV. The values for isotropic simulations raise faster than the corresponding values for signal simulations. The probabilities for the signal simulations are slightly lower for a minimal energy threshold of 12 EeV than for 6 EeV. The results look similar for different signal simulations e.g. incorporating more sources.

$\varepsilon = 0.14$  rad at  $\Sigma\sigma > 14$  and reaches 90% for  $\Sigma\sigma = 24$  and in contrast for the signal simulations, it raises more slowly in the beginning and hardly exceeds 20% for  $\Sigma\sigma = 24$ . This behavior does not change much with energy. Thus, high values of  $\Sigma\sigma$  increase the performance of the analysis by increasing the gap between isotropy and signal simulations, but also the risk of not being able to filter interesting candidates in the data. This gap between signal and isotropic simulations is significantly lower for  $\varepsilon = 0.21$  rad and consequently, the value  $\varepsilon = 0.14$  rad is favored over  $\varepsilon = 0.21$  rad.

To evaluate the performance of the analysis the test statistic  $t$  must be compared to isotropic simulations as shown in figure 7.14 for  $\varepsilon = 0.14$  rad. Note that an identical set of simulations at each energy is used to evaluate the performance as a function of the two cluster parameters  $\Sigma\sigma$  and  $\varepsilon$ . The aforementioned gap in the probability to filter no corridor between isotropic and signal simulation manifests itself here in a shift in the test statistic  $t$  between both distributions for higher values of  $\Sigma\sigma$ . However, the signal distributions show also a greater spread due to their tails to large test statistic values.

The significance of the median test statistic  $\tilde{t}$  is shown in figure 7.15. It is obtained by first calculating the number of test statistic values from the isotropic simulations above the median test statistic of the signal simulations  $N(t_{\text{iso}} \geq \tilde{t}_{\text{signal}})$ . In cases where this number is zero it is conservatively set to one. In a second step the ratio  $N(t_{\text{iso}} \geq \tilde{t}_{\text{signal}})/N_{\text{iso,tot}}$  to the total number of isotropic simulations  $N_{\text{iso,tot}}$  is converted into a Gaussian standard deviations. Cases without filtered corridors are included by setting their test statistic  $t = \ln \mathcal{L} - \ln \mathcal{L}(f = 0)$  to zero which corresponds to setting their signal fraction  $f$  to zero. In the figure it can be seen that the smaller value  $\varepsilon = 0.14$  rad is generally preferred over  $\varepsilon = 0.21$  rad. Higher

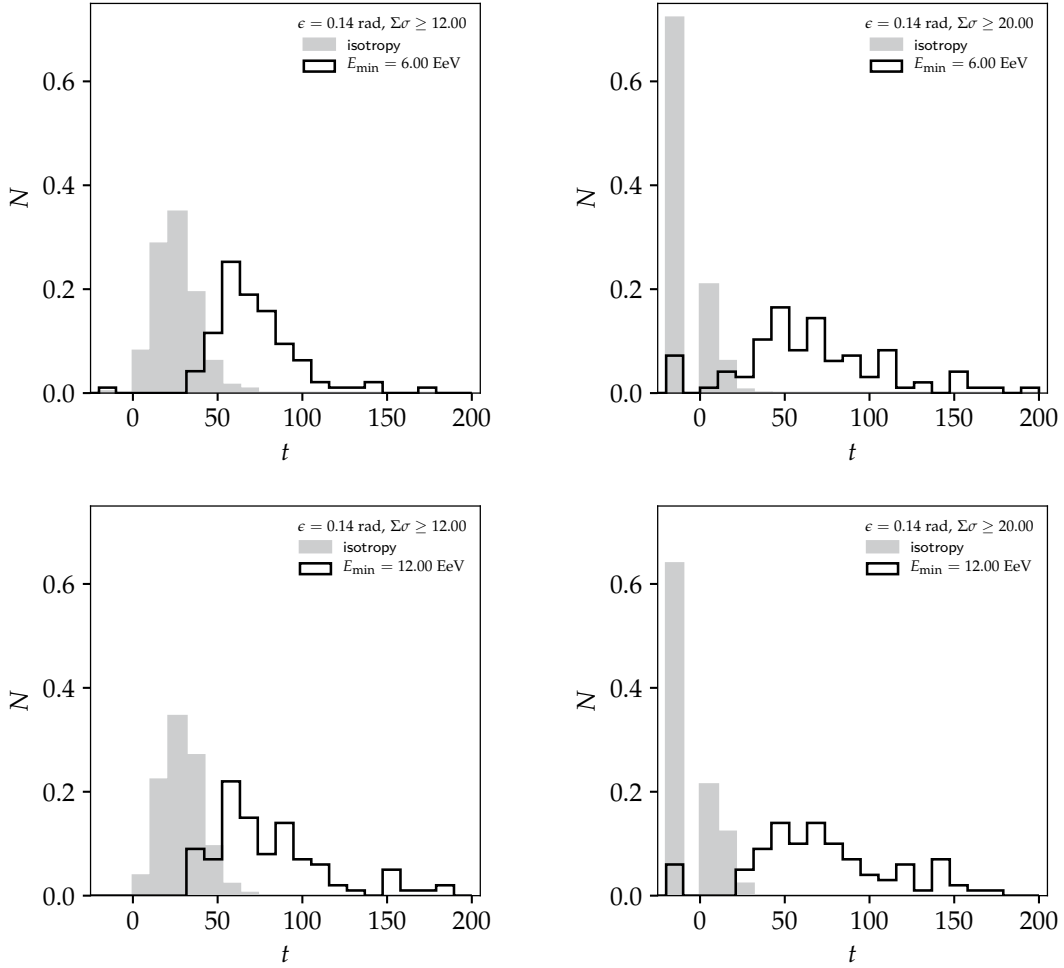


Figure 7.14: Distribution of the test statistic for various sets of parameters: (top) a minimal energy of 6 EeV and signal fraction  $f_{\text{sig}} = 3.2\%$  and (bottom) 12 EeV and  $f_{\text{sig}} = 3.8\%$ , (left)  $\Sigma\sigma = 12$  and (right)  $\Sigma\sigma = 20$ . For all cases the cluster parameter  $\epsilon$  is set to 0.14. The number of simulations where no corridor could be detected is shown with a test statistic  $t < 0$ .

values of  $\Sigma\sigma$  increase the performance of the algorithm, the highest significance is seen for  $\Sigma\sigma = 20$  at  $E_{\min} = 12$  EeV. Increasing  $\Sigma\sigma$  to values above 20 will decrease the performance as the risk of not being able to filter at least one cluster is increased, see figure 7.13.

Generally, the rigidity dependent projections of the filtered corridors on Earth can be used to improve the initial charge hypotheses independent for each cosmic ray. Afterwards the analysis can be repeated with the updated charge distributions. Typically, the size of the corridors shrinks and also the value of the test statistic increases. The same iterative method must also be applied to isotropic simulations in order to assess an improvement in the significance. A ratio  $t_2/t_1$  is calculated individually for each simulation by using the best fit test statistic from the first (second) iteration  $t_1$  ( $t_2$ ). Figure 7.16 shows a typical example of the ratio of the test statistic for both iterations. For signal simulations an improvement of slightly below a factor of two is

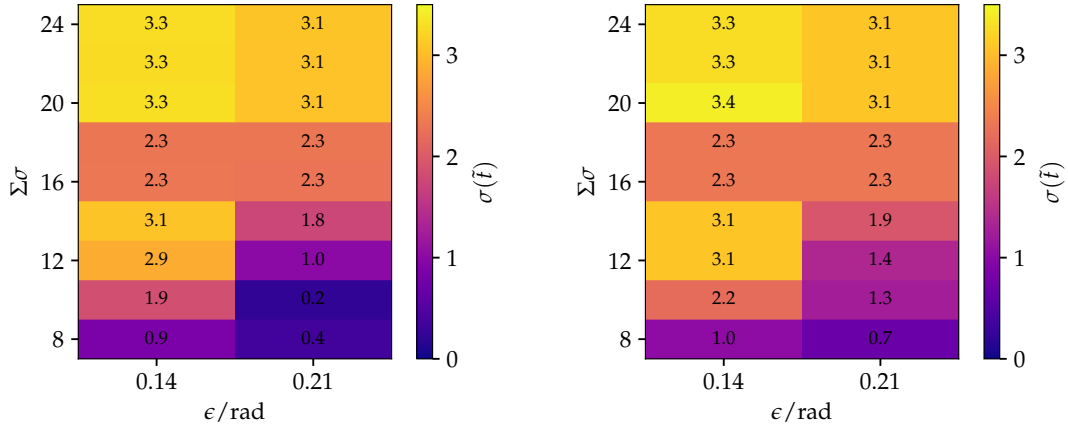


Figure 7.15: Median significance as function of the two parameters of the cluster algorithm for a minimal energy of (left) 6 EeV and (right) 12 EeV.

seen whereas for isotropic simulations the improvement is slightly higher with tails even to very high values above five. Thus, the overall significance to claim local structures in the arrival directions of UHECRs above the ones seen in isotropy does not benefit from a second iteration.

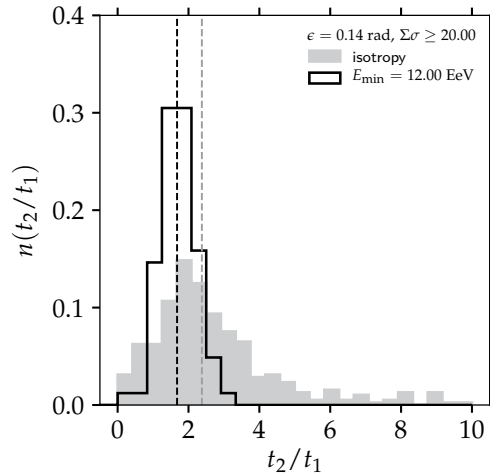


Figure 7.16: Test statistic ratio for two iterations for a minimal energy  $E_{\min} = 6$  EeV, 4 sources with an initial smearing of  $3^\circ$  and using the best cluster parameters  $\epsilon = 0.14$  rad and  $\Sigma\sigma = 20$ . The vertical dashed lines denote the medians of the respective distributions.

## 7.7 Sensitivity to the Detection of Anisotropy

After setting the free parameters to  $\epsilon = 0.14$  rad,  $\Sigma\sigma = 20$  and  $E_{\min} = 12$  EeV the sensitivity of the method can be evaluated. Figure 7.17 shows the median expected significance as function of  $E_{\min}$  and  $\Sigma\sigma$  with a maximum at  $3.4\sigma$ . It is interesting

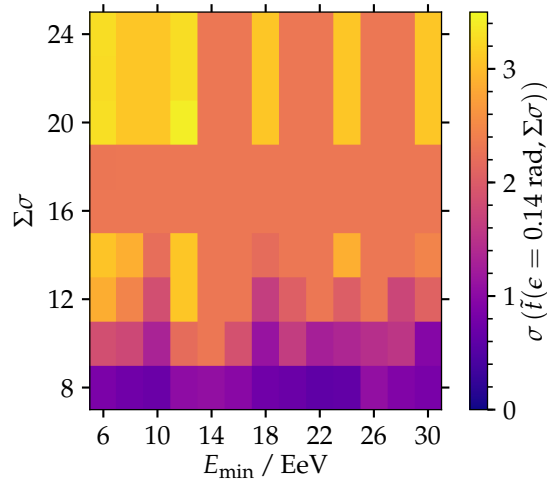


Figure 7.17: Expected sensitivity as function of energy by using  $\varepsilon = 0.14$ . This figure shows the results for 4 sources, however, the results are similar for all numbers of sources.

to observe that the sensitivity has multiple peaks every 6 EeV. To understand this feature one must remember two characteristics of the simulations. On the one hand, the steep energy spectrum ensures that most events are at the lowest permissible energy. On the other hand, a limit of 6 EeV was found above which ballistic deflections take place. Due to these restrictions at  $E_{\min} = 6$  EeV mainly protons can be fitted with a correct charge, at  $E_{\min} = 12$  EeV also helium can be assigned to the UHECRs which also explains the slightly better sensitivity here. For higher energies the same scheme can be continued.

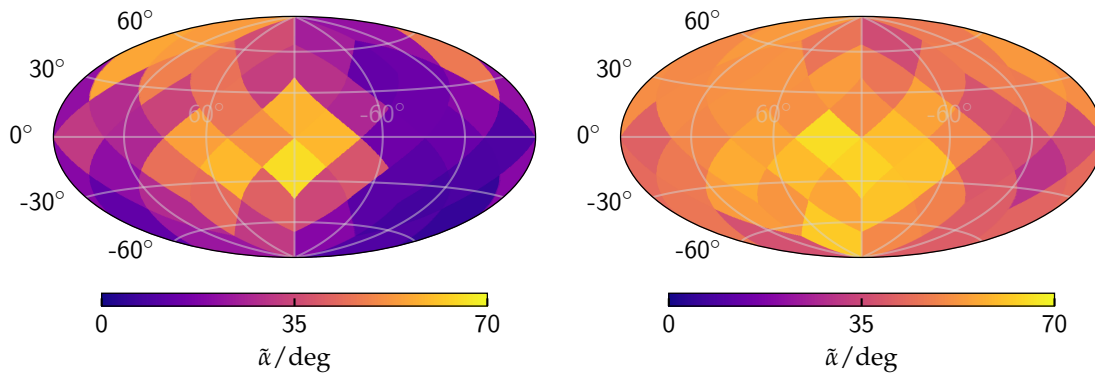


Figure 7.18: (left) Median angular distance of the closest corridor to a source in the direction of a pixel center. The distances are averaged over all numbers of sources ( $n_{\text{src}} \in [2, \dots, 10]$ ) as the number of sources is not known when applying the analysis to data. (right) Similar to the figure on the left but with shuffled directions which can be interpreted as trivial distances.

A typical question in the context of this work is how precise the original source directions can be reproduced by the fit. Figure 7.18 (left) shows the median angular distance  $\tilde{\alpha}$  of the closest corridor to a source in the direction of the pixel by taking into account all simulated numbers of sources. First, the angular difference is mainly below  $35^\circ$  for regions well inside the exposure of the Pierre Auger observatory. Note, this is in the same order of magnitude as the difference  $\delta$  in the deflections shown in figure 5.12. Second, the largest angular difference is close to the direction of the galactic center where the models of the GMF have difficulties to describe the deflections. Third, regions in the northern hemisphere outside of the exposure also have larger angular differences which can be explained by the fact that sources in these regions are typically located at the end of a thread like structure. Figure 7.18 (right) shows the same medium angle alpha but the directions of the filtered regions were distributed randomly on the sphere. This was achieved by shuffling the assignments between the sets of filtered regions and the sets of simulated sources individually for each number of sources. Here, the medium angle  $\tilde{\alpha}$  is typically above  $35^\circ$ .

Figure 7.19 shows the angular difference from two different perspectives. The figure on the left hand side displays the angular distance  $\alpha$  from a simulated source to the closest filtered region and thus ignores that a filtered region might be closer to another source. Thus, this histogram corresponds to figure 7.18. Note that both figures contain all numbers of sources. In contrast, the figure on the right hand side presents the angular difference  $\beta$  between the filtered regions and the closest original

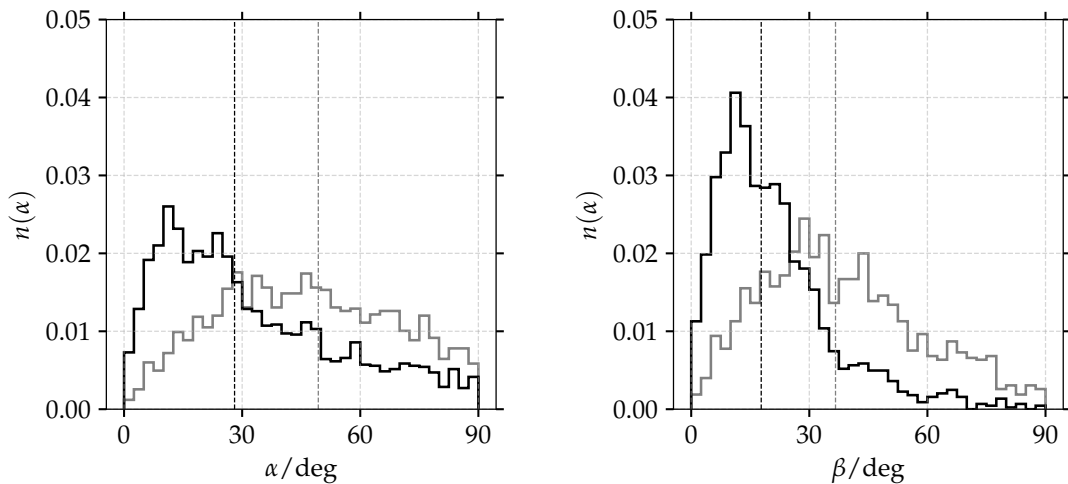


Figure 7.19: Distributions of the angular distance (left) between each simulated source direction and the center of the closest found extragalactic corridor and (right) between the center of each found extragalactic corridor to the closest source. Note, in the left (right) case one corridor (source) is assigned to each source (corridor) which can be the same for multiple sources (corridors). The gray distributions are obtained from shuffling comparing shuffled filtered directions to the sources. The vertical lines mark the corresponding medians. The distributions are averaged over all numbers of sources  $N_{\text{src}} \in [2, \dots, 10]$ .

source neglecting that some sources might not be found. The gray histograms contain the corresponding angle analogous to before by shuffling the assignments between filtered regions and sources. In both cases the analysis results are in average  $\sim 15^\circ$  better than the expectation from trivial directions. These plots suggest that due to the large uncertainties in the GMF models and the challenging measurement of the charges, the analysis typically finds structures in which potential source directions are contained but does not point directly back to the source directions. This can also be understood in the context of the frequency filter. A detuned transformation still allows to improve a signal time trace but does not to identify the correct frequency in the frequency domain.

This can be confirmed by investigating the mean efficiency and the purity displayed in figure 7.20. They are defined for each scenario in equations (7.7) and (7.8) where

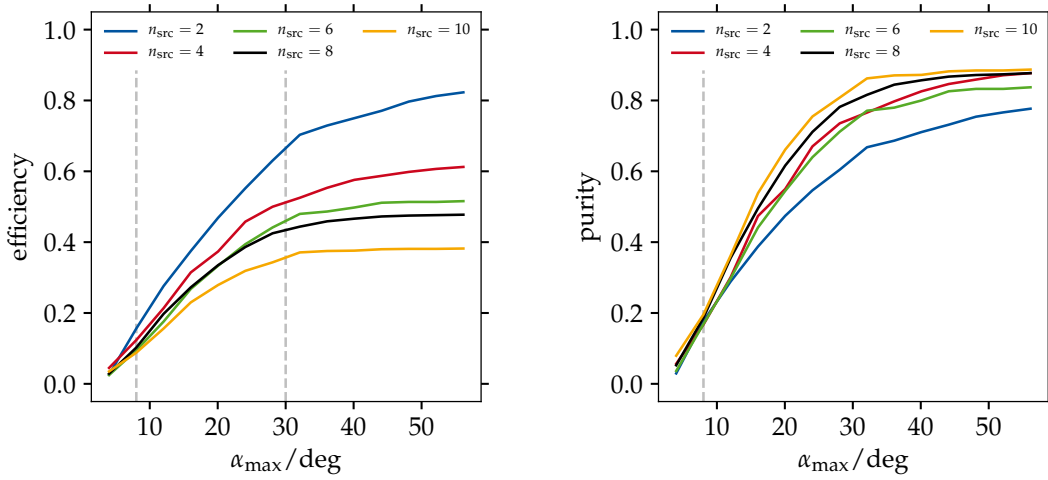


Figure 7.20: Efficiency and purity for different numbers of sources as function of the maximal allowed angle  $\alpha_{\max}$  between the original source and the closest center of a corridor of interest. The vertical gray lines denote  $\alpha_{\max} = 8^\circ$  corresponding to a one pixel ring around the original source using the HEALPix pixelisation scheme at  $n_{\text{side}} = 16$  and  $\alpha_{\max} = 30^\circ$  being the mean angular difference between the PT11 and JF12 parameterizations at 12 EeV.

$N_{\text{total in simulation}}$  is the total number of simulated sources and  $N_{\text{found}}$  the number of filtered regions. The difficult part is the definition of the correctly found sources  $N_{\text{correctly found}}$  as a maximum angle  $\alpha_{\max}$  is required representing the angular difference between a source and the closest filtered regions.

$$\text{efficiency} = \frac{N_{\text{correctly found}}}{N_{\text{total in simulation}}} \quad (7.7)$$

$$\text{purity} = \frac{N_{\text{correctly found}}}{N_{\text{found}}} \quad (7.8)$$

The efficiency depends on the number of input sources and is in the order of 15% when considering only the neighboring pixels around the original source direction and

varies between 35 % and 70 % for  $\alpha_{\max} = 30^\circ$  which is the mean angular difference between the PT11 and JF12 magnetic field parameterizations at  $E = 12 \text{ EeV}$ , see figure 5.12. The purity is also in the order of 15 % but varies between 65 % and 90 % for the same angles as above.

This confirms that if a region is filtered it has a high probability to be related to the original source direction and thus that the number of false positives, where a region is selected from the background, is low. Note that the analysis has been tuned to claim local structures in the arrival directions beyond trivial configurations and not on precisely detecting the direction of sources. The latter might be possible with the detector upgrade ‘‘Auger Prime’’ [49] but certainly requires an improved understanding of the galactic magnetic field and better information about the charge of cosmic rays.

## 7.8 Dependency on Magnetic Field Uncertainties

‘‘[...]To investigate the dependency of the analysis on the direction of the deflection in the galactic magnetic field a simple simulation model for the galactic magnetic field is assumed: The deflection strength is set to  $20^\circ \times \frac{10 \text{ EeV}}{R}$  where  $R$  is the rigidity of the cosmic ray in EV.

Cosmic rays are generated from a single source giving 5% signal fraction with a mixed composition consisting of 15 % protons, 45 % helium and 40 % CNO. The cosmic rays from this source were subjected to the linear deflections of the simple field model only. Multiple sets of cosmic rays are created where the direction of these deflections is fixed, but rotated by an on-plane angle  $\psi$  around the source direction in steps of  $10^\circ$ . [Here, the angle  $\psi$  is zero in the direction of the local spherical unit vector  $\vec{e}_\theta$ .] The expected best agreement between the simple galactic field model and the JF12 field is at  $\psi = 110^\circ$  [...] [221] with a slight dependency on the rigidity. Two exemplary arrival direction sets for  $\psi = 110^\circ$  and  $\psi = -70^\circ$  are shown in figure 7.21.

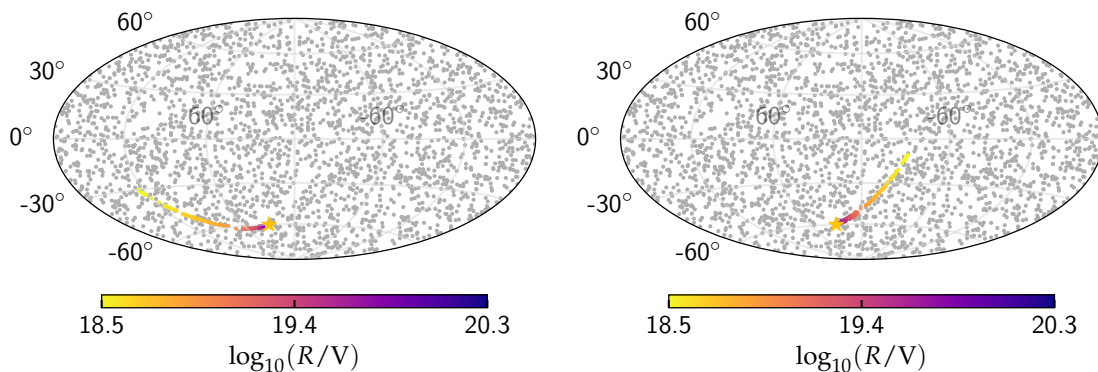


Figure 7.21: Simulation of the directional uncertainty of the GMF by rotating the deflected cosmic rays around the original source direction with (left)  $-70^\circ$  and (right)  $110^\circ$  which has also the best agreement with the JF12 model.

“[...]The minimal energy was set to  $E_{\min} = 24 \text{ EeV}$  which leads to a maximum deflection of  $67^\circ$  which is similar to the value of the JF12 GMF model.[...]” [221] Note that the minimal rigidity in this case is already at 3 EV; below this value non-linear effects in the deflection are strong and can not be approximated by the simple simulation model. “[...]The remaining 95 % cosmic rays are given by an isotropic distribution. The total number of cosmic rays was adjusted to 2854 following data statistics at this energy cut. The analysis is then performed with the JF12 magnetic field model and repeated with 30 simulated data sets for each rotation angle  $\psi$ .

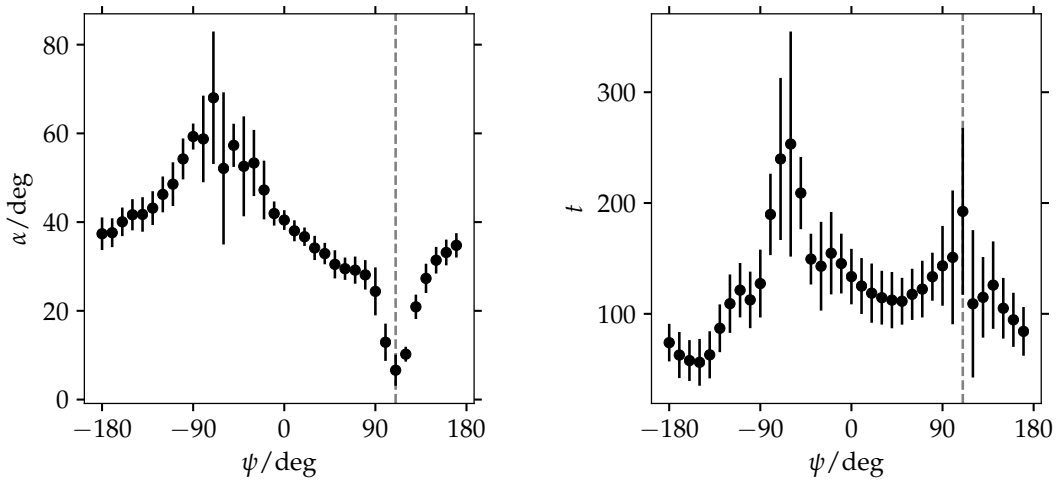


Figure 7.22: (left) Mean angular distance and (right) test statistic of closest filtered extragalactic direction as function of the rotation angle  $\psi$ . The grey dotted line denotes the direction corresponding to the JF12 parameterization. The peaks in the test statistic occur at the rotation angle  $\psi$  which is aligned to the JF12 model and its inverted direction. However, it is not expected that the knowledge of the GMF is wrong by  $180^\circ$ .

Figure 7.22 (left) shows the angular distance  $\alpha$  of the closest filtered extragalactic direction to the simulated source direction. It is found that the distance decreases with the agreement between the simple linear deflection model and the JF12 model. For a fully reversed field ( $\psi = -70^\circ$ ) the distance  $\alpha$  has its maximum.

Figure 7.22 (right) displays the mean test statistic  $t$  and its standard deviation as a function of the rotation angle  $\psi$ . Both, the direction  $\psi = 110^\circ$  with good agreement between the simple model and the inverted direction show a high value of the test statistic. In the first case, the cluster center is close to the true source and picks up cosmic rays with low charges. In the second case, the cluster center is far away from the true source such that cosmic-rays with medium charges contribute. Consequently, the analysis performs best at directions where the alignment between the galactic magnetic field and its model is in the order of  $\pm 10^\circ$ . [...] [221] To improve this behavior it is useful to constrain the charges stronger.

Figure 7.23 shows the average direction of the closest filtered extragalactic region as function of the rotation angle  $\psi$ . The fluctuations can be explained by the small statistics of only 30 simulated sets per rotation angle  $\psi$ .

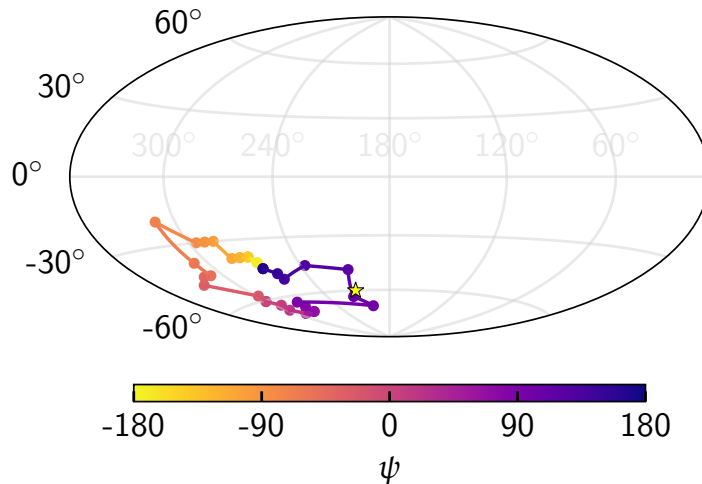


Figure 7.23: Average direction of the closest filtered corridor for rotated GMF. The color code indicates the rotation angle  $\psi$  of the linear GMF model.

## 7.9 Technical Implementation

This section deals with different technical aspects of the analysis and the execution environment. A key development within the scope of this analysis is a flexible data container to store sets of cosmic rays. It is based on NumPy named arrays [237] and can be used similarly which allows a smooth integration into the SciPy ecosystem [238]. The container can be dynamically extended by either adding new cosmic rays or by storing new properties which might be either per cosmic ray, e.g. the energy, or per set of cosmic rays, e.g. the version of the reconstruction software. It is now used in the `astrotools` python package [239] as a basic data type and also extended to store multiple sets at once which allows the parallel application of an analysis to multiple sets as typically required in parameter scans. Furthermore typical plotting functions, e.g. to display the arrival directions, are implemented within this scope using the `matplotlib` graphics environment [240].

The analysis was mainly executed on the VISPA cluster which was set up within the scope of the VISPA project [241] and consists of 208 CPU cores, 21 GPUs and is equipped with more than 150 TB of hard disk. The author played a central role in the development of the cluster starting with the selection of the required software and hardware components. It continues with the development and implementation of various concepts in the areas of network design, data storage, monitoring and security in cooperation with the IT center of the RWTH Aachen University up to the improvement of the uptime, providing physics software and connection of additional services such as a weather station.

Furthermore, the cluster is accessible via the VISPA web platform where the author developed the file browser as a key component. The work within the scope of the VISPA project manifests itself in various publications and conference presentations in the area of computing [242, 243, 244, 245, 246, 247, 248, 249, 250, 251].

# 8. Search for Local Structures in the Arrival Directions of Cosmic Rays

This section presents the results of applying the analysis to the selected cosmic rays presented in section 6.3. The exact procedure of all analysis steps was presented in the previous chapter and only the most important aspects are repeated. The results are described for both, the reference galactic magnetic field from Jansson and Farrar (JF12) and the alternative parameterization from Pshirkov and Tinyakov (PT11). Note that the analysis has been tuned to use the JF12 parameterization and that the use of the PT11 parameterization only serves to investigate the stability of the below presented results.

This chapter is structured as follows, first the outstanding extragalactic directions are introduced (section 8.1). Afterwards, the question “[...]how well can the observed cosmic rays be described when forward tracking cosmic rays through the galactic magnetic field from these filtered directions[...]” [221] is examined (section 8.2). Finally, the cosmic rays in the corridors of arrival directions on Earth are further investigated (section 8.3).

## 8.1 Outstanding Extragalactic Directions

After assigning a uniform charge distribution to all cosmic rays they are back transformed to the edge of the galaxy. Figure 8.1 shows the superimposed maps using the JF12 (the PT11) magnetic field model. It is interesting to observe that both maps have very little in common, only the elongated structure close to the galactic disk shows some similarities although the peak in the PT11 field is much more pronounced. In the northern hemisphere it is visible that correcting for deflections in the PT11 field generally does not increase the field of view as much as the JF12 parameterization does.

However, when requiring each direction of the back transformed maps to be above the 90% quantile of the isotropic expectation the structures look more similar, see figure 8.2. Thread like structures are observed in both maps in similar directions. For the JF12 field parameterizations two directions fulfill the requirements of the cluster algorithm. The directions of the single filtered direction in the case of the PT11 field agrees with one region of JF12 parameterization. This is expected as the angular differences for deflected cosmic rays are small in this area.

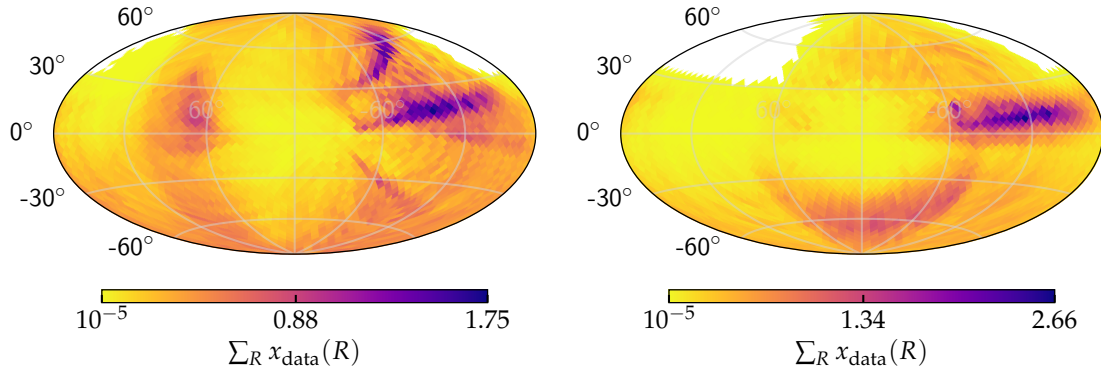


Figure 8.1: Backward transformed measured cosmic rays using (left) the JF12 and (right) the PT11 field model. The distributions of all cosmic rays and rigidities are superimposed.

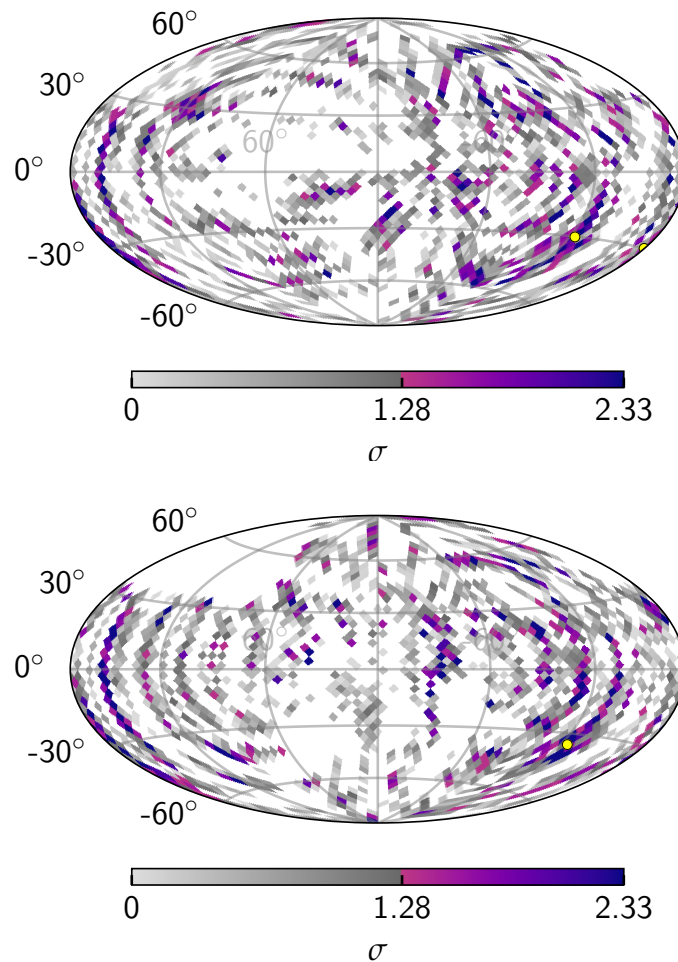


Figure 8.2: Deviation from the isotropic background and outstanding extragalactic regions (yellow markers) for the (left) JF12 and (right) PT11 field model. Two outstanding regions were found in the JF12 case and one in the PT11 case fulfilling the conditions of the cluster algorithm with  $\epsilon = 0.14$  rad and  $\Sigma\sigma = 20$ .

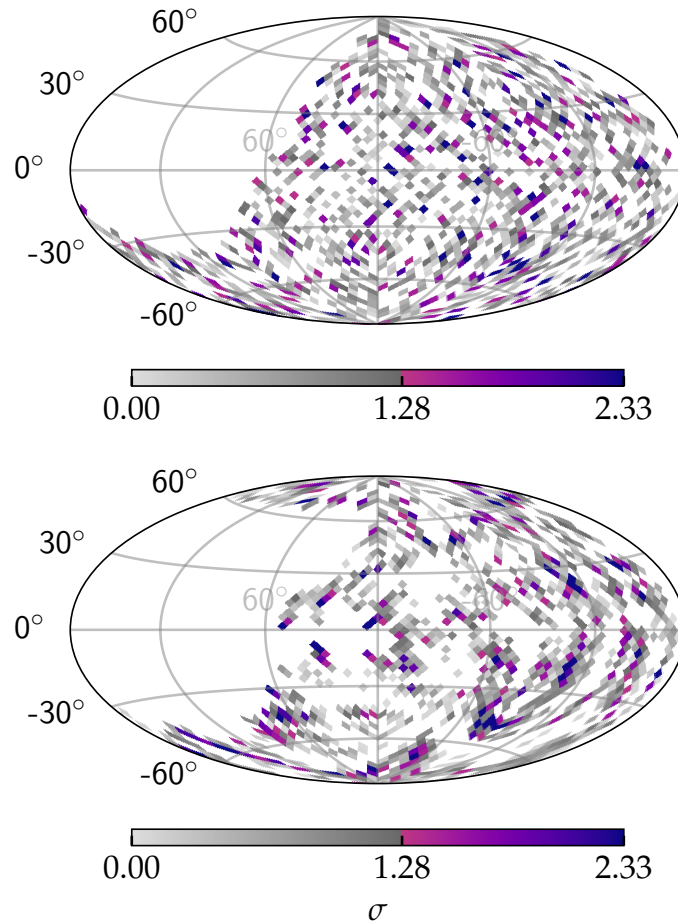


Figure 8.3: Deviation from isotropy assuming (left) neutral particles and (right) anti-particles and the JF12 magnetic field. In both cases no outstanding directions could be filtered.

Figure 8.3 shows the deviation from the isotropic expectation assuming neutral particles on the left side and antimatter on the right side. In both cases no outstanding directions could be filtered out. As neutral particles are not deflected in the galactic magnetic field the field of view is equal to the exposure of the Pierre Auger Observatory and no threadlike structures are visible here. Thus, only significant over-densities in the local arrival directions of the ultra-high energy cosmic rays (UHECRs) could potentially be filtered out. In contrast, for antimatter the distribution looks slightly more structured but no region fulfills the previously tuned requirements of the cluster algorithm.

## 8.2 Results of the Likelihood Test

In this section the question of how well the filtered regions can describe the arrival directions of UHECRs is examined with the help of the test statistic  $t = \ln \mathcal{L} - \ln \mathcal{L}(f = 0)$ , see also equation (7.6).

### Parameters of the Likelihood Fit

The test statistic is shown as a function of its two parameters, the anticipated signal fraction  $f$  and the smearing  $\delta$ , in figure 8.4. In the case of the JF12 field the best fit values  $f^{\text{JF12}} = 1.1\%$  and  $\delta^{\text{JF12}} = 7^\circ$  lead to a test statistic of  $t^{\text{JF12}} = 22.5$ . For the PT11 field the corresponding values are  $f^{\text{PT11}} = 1.7\%$ ,  $\delta^{\text{PT11}} = 20^\circ$  and  $t^{\text{PT11}} = 12.7$ . Here, the method tries to increase the smearing radius up to its maximum scanned value to collect as many cosmic rays as possible. Note that the distribution exhibits a second maximum at a smaller smearing which is by far not as prominent as the global maximum. The large difference in the test statistic can be explained by the fact that the two filtered regions in the JF12 model overall reach more particles.

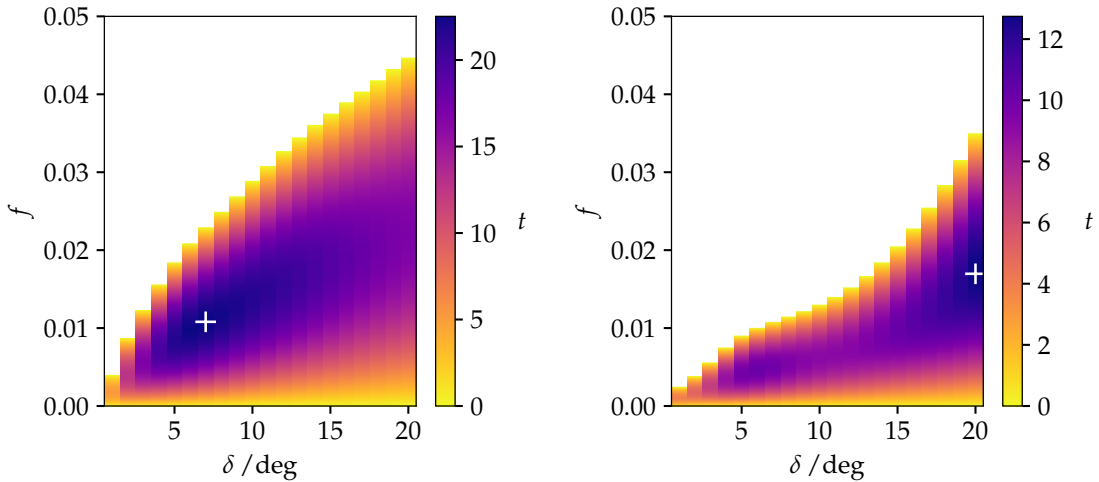


Figure 8.4: Distribution of the test statistic as function of the two fit parameters  $f$  and  $\delta$  for the analysis using the (left) JF12 and (right) PT11 field model.

### Likelihood Ratio Analysis

Figure 8.5 displays the comparison of the best fit test statistic to the isotropic distribution obtained from 50000 simulations. “[...] For 80 % of the isotropic scenarios no filtered extragalactic direction is found [in the case of the reference analysis using the JF12 model]. For the remaining 20 % extragalactic directions were filtered, however, 1.6 % show a greater test statistic than  $t^{\text{JF12}}$  on data.

Thus, the test statistic of the measured data agrees within 2.15 standard deviations with the isotropic scenarios for the JF12 field [and within 1.24 standard deviations for the PT11 field]. A possible explanation for this compatibility could be that the mismatch between the JF12 regular model and the galactic magnetic field realized in nature is greater than the mismatch between the PT11 and JF12 model. The latter were used to investigate the influence of the uncertainty of the galactic magnetic field and to evaluate the sensitivity of the method. Another possibility is that the measured cosmic rays originate from many different sources with each only a small contributing fraction which can not be revealed by this method. [...]” [221] The

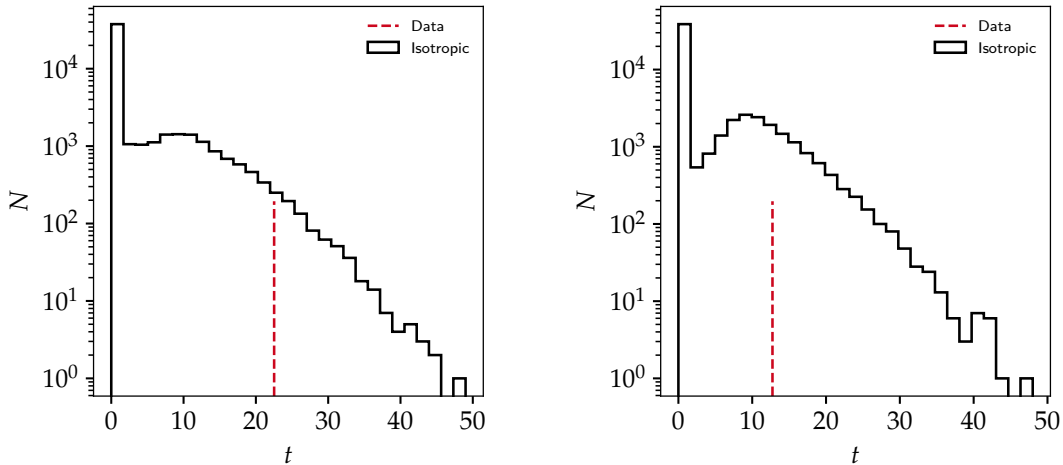


Figure 8.5: Comparison of the test statistic measured in data (red line) to isotropic simulations (black histogram) for (left) the JF12 and (right) PT11 field model.

analysis was tuned to the astrophysical scenario that a few nearby sources account for a few percent of the measured cosmic rays.

### 8.3 Cosmic Rays in Corridors of Arrival Directions on Earth

Although the results show a compatibility with isotropy, the cosmic rays in the filtered corridors of the arrival directions on Earth are further discussed in this section to obtain a final evaluation of the results and a better understanding of the potential of the method. For this purpose a definition for particles correlating with a filtered direction is required. Various properties were tested on a simulation basis and a cut on the maximum value of the signal probability density function (PDF)  $\max S(\log_{10} R) \geq 10^{-3}$  was best able to classify signal events on simulated scenarios. When applying this condition 511 particles are assigned to the filtered extragalactic directions for the JF12 field. However, no particle fulfills this requirement for the alternative PT11 field thus there the threshold is arbitrarily relaxed to  $10^{-4}$  leading to 1766 particles.

#### Energy Spectrum

Figure 8.6 (top) shows the energy of the correlating cosmic rays as a function of their arrival directions and (bottom) the energies of the correlating particles compared to the background particles.

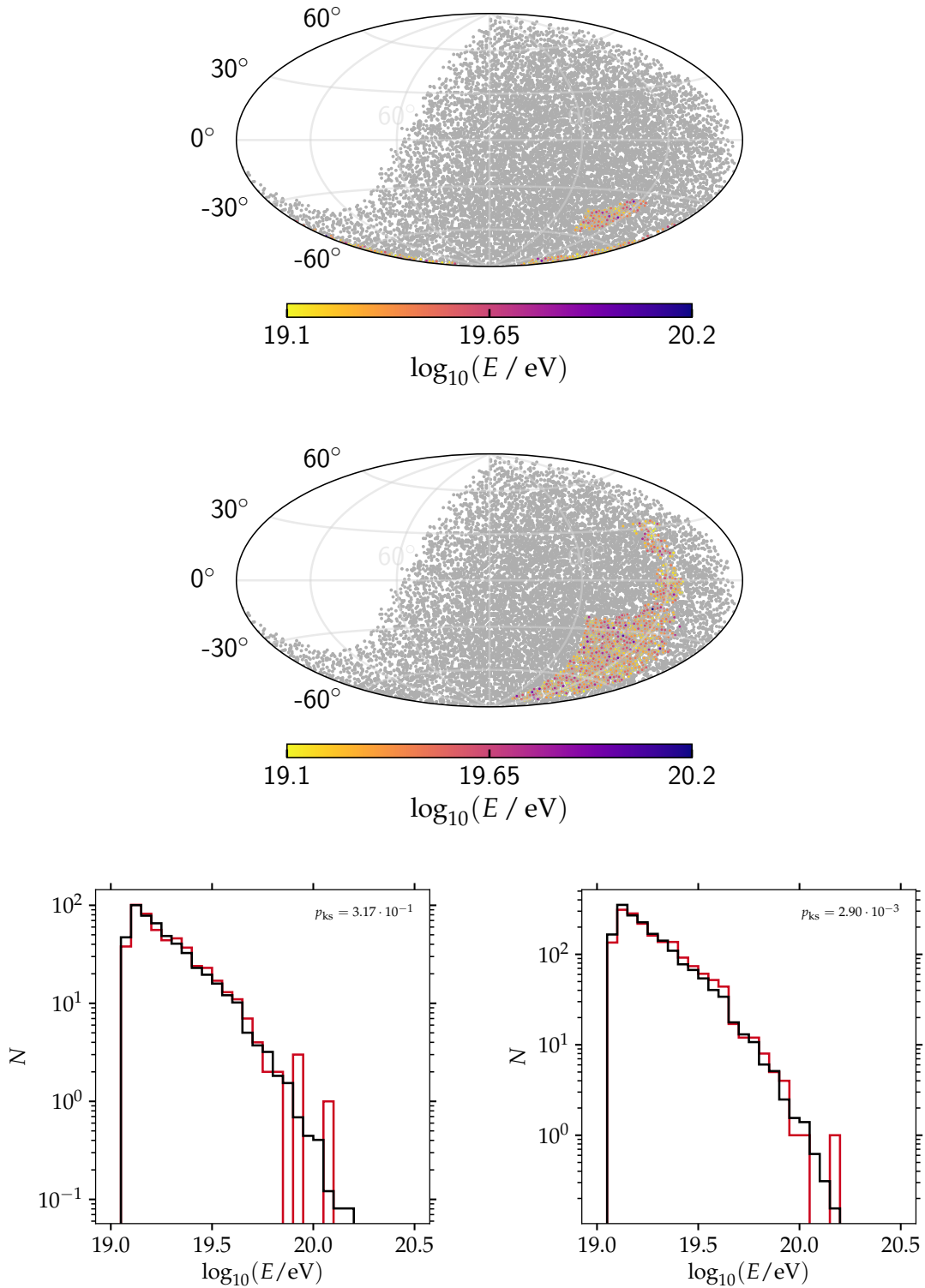


Figure 8.6: Energy distribution of correlating cosmic rays for the (left) JF12 and the (right) PT11 field model. The arrival directions as a function of energy do not show any anomalies. In the bottom row the energy distributions of correlating cosmic rays and the remaining cosmic rays are compared using a Kolmogorov-Smirnov test. Note that the background cosmic rays were weighted with the ratio  $N_{\text{corr}}/N_{\text{background}}$  with  $N_{\text{corr}}$  ( $N_{\text{background}}$ ) being the number of correlating (background) cosmic rays.

In both cases no energy ordering is visible and the distributions are also not centered around the highest energetic particle as typically assumed in analyses depending on a region of interest [228]. The histograms in figure 8.6 (bottom) show the distribution of the energy of correlating particles (red) and the remaining particles. A Kolmogorov-Smirnov test [100, 101] shows that in the case of the JF12 field both distributions are fully compatible to each other, in the case of the PT11 field the agreement is at the level of  $2.8\sigma$ . But here, the arrival directions of correlating cosmic rays are spread over a large angular range which can on one hand be explained by the relaxed cut on  $\max S(\log_{10} R)$ . On the other hand, the large value of the smearing  $\delta^{\text{PT11}} = 20^\circ$  additionally leads to multiple images of the same extragalactic direction. This becomes even more apparent in figure 8.7 showing the most probable rigidity of correlating cosmic rays.

### Rigidity

Here, a rigidity ordering is visible, cosmic rays with a large angular distance to the the respective outstanding direction typically have lower rigidities. Due to the

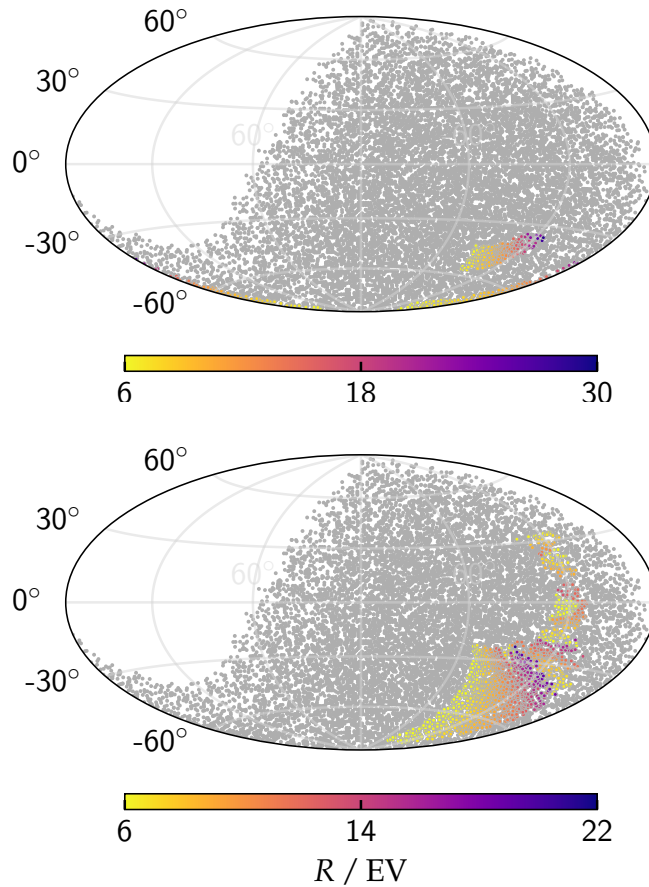


Figure 8.7: Best fitting rigidity of correlating cosmic rays for the (left) JF12 and the (right) PT11 field model. A cosmic ray is called correlating when the maximum of its signal distribution exceeds  $\max S(\log_{10} R) \geq 10^{-3}$  for the JF12 field and  $10^{-4}$  for the PT11 field.

charge assignment, the fit allows to select cosmic rays with a rigidity ordering over a large area in the sky. In the analysis using the JF12 field, cosmic rays have a high rigidity close to filtered extragalactic region which then decreases with the angular distance. For the PT11 field, the more extended distribution consists of multiple regions each exhibiting a clear rigidity ordering. Note, the lower value of 6 EV restricts the propagation of cosmic rays to the ballistic regime, see chapter 5.

### Charges

Figure 8.8 displays the signal distributions  $S(Z)$  as a function of the charge  $Z$  for two cosmic rays. These distributions are obtained by converting the signal distribution as a function of rigidity  $S(R)$  to a function of charge with the use of the measured energy  $E$  and the relation  $Z = E/R$ . The best way to imagine the emergence of this distribution is to imagine how the distribution of the directions of the filtered region as a function of rigidity passes by the measured cosmic ray like in a movie. The left image shows a cosmic ray with a best fitting charge of  $Z = 4$  with a quite narrow width of  $\Delta Z \approx \pm 1$ . The distribution on the right hand side exhibits two peaks with a best agreement for protons and a small probability for helium. This kind of structure is visible only in cases when the rigidity dependent projections of multiple sources can pass by the measured direction of the cosmic ray or in the case of multiple images evolving differently with rigidity. Note that in general the analysis allows to select non integer charges. Consequently, if the sources of cosmic rays were discovered, the method would also provide a completely new method for measuring the charges of UHECRs without being dependent on hadronic interaction models as e.g. the atmospheric depth  $X_{\max}$ .

Figure 8.9 displays the most probable charge of the correlating cosmic rays. For the JF12 field the charges increase with the distance to the filtered region to achieve a lower rigidity as seen in figure 8.7. For the PT11 case protons are dominating the

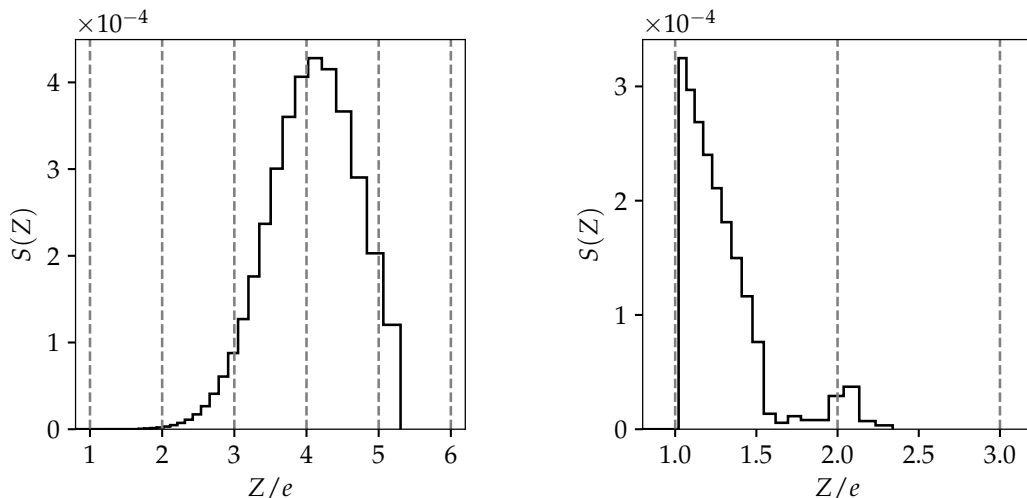


Figure 8.8: Charge distributions for two different cosmic rays for the (left) JF12 and (right) PT11 model.

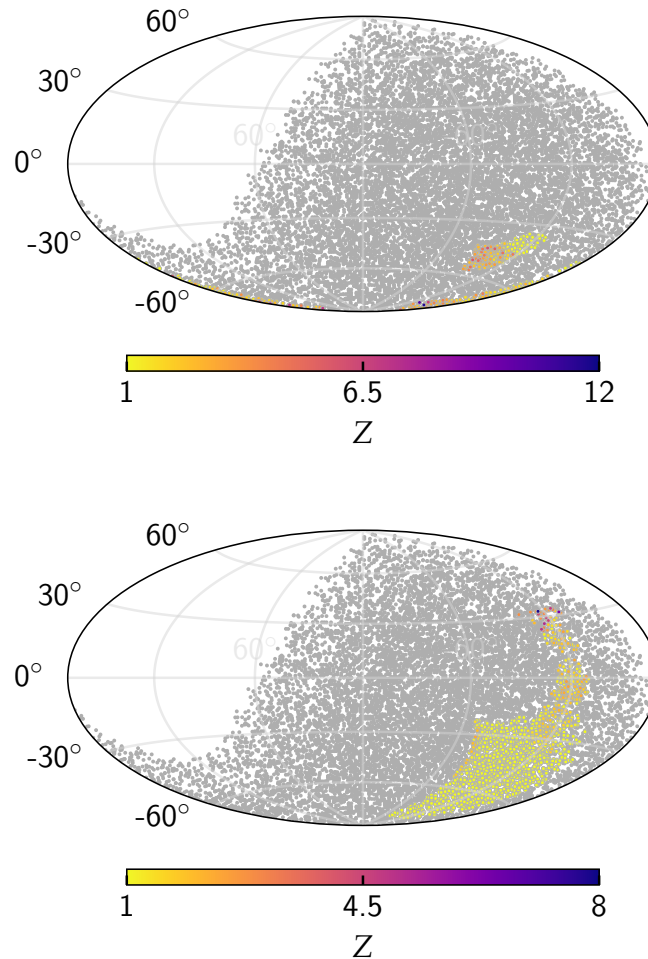


Figure 8.9: Distributions of the best fit charges as a function of the arrival directions for the (left) JF12 and (right) PT11 model.

charge distribution which can be explained by the large best fitting smearing of  $20^\circ$  which is applied to the region.

Typically, analyses search for energy related correlations [83, 228] but information on the charge might be available in the near future e.g. via modern deep learning techniques or detector upgrades or both and thus open a new window to the detection of sources. Improved magnetic field models e.g. by including dust emission data to the fit [252, 253, 254] or by advanced studies of the uncertainties [255] will allow to reduce the differences between simulation and measurement. Analyses that use the galactic magnetic field as a charge spectrometer can achieve higher precision and thus lead the search for cosmic ray sources at least one step further, if not to the detection.



## 9. Conclusion

One of the major questions in astroparticle physics is where and how ultra-high energy cosmic rays (UHECRs) are accelerated to energies far above 1 EeV. The search for the sources is challenging as cosmic rays are deflected by magnetic fields during their propagation to Earth. Consequently, their measured arrival directions do not point directly back to the sources. Typically, it is distinguished between small scale random fields which mainly smear the arrival directions like a widening of an optical beam and structured fields leading to directional deflections depending on the rigidity  $R = E/Z$  of the cosmic rays defined as energy charge ratio. Particularly, the structured part of the galactic magnetic field (GMF) with its high magnetic field strengths of up to 5  $\mu\text{G}$  is responsible for a significant part of the total deflection.

In the first part of this thesis, the deflections in two different galactic magnetic field models are investigated. These models are tuned to measurements of Faraday rotation and synchrotron emission. It was found that the models can meaningfully describe the directional deflections for rigidities above  $R = 6 \text{ EV}$ . Below, the differences between the predictions of the different models are large and additionally both models predict deflections compatible with a random walk. Furthermore, the differences of the models near the galactic disk with latitude  $|l| < 19.5^\circ$  are found to be substantial. Additionally, it was discussed that the GMF has preferred directions with a higher transmission of cosmic rays leading to an inhomogeneous visibility of the extragalactic universe. Finally, it was demonstrated that a single source outside the galaxy can be seen on Earth from different directions which is called multiple images.

The gained knowledge of the magnetic field was used to develop a new filter technique to reveal thread-like patterns in the arrival directions of UHECRs. These patterns are formed by the structured fields when UHECRs with different rigidities are deflected similar to a spectrometer. Here, cosmic rays with high rigidities can typically be observed in the vicinity of the source direction and cosmic rays with low rigidities have large distances to the source direction.

The general idea of this method is first to correct the measured arrival directions of the cosmic rays for their deflections in the GMF, then to filter potential source candidates in this corrected frame and finally to evaluate the filtered directions in a likelihood ratio analysis. With perfect knowledge of the magnetic field, the energies and charges of the cosmic rays, the method would contract the alignment patterns. However, only arrival directions and energies but not the charges of UHECRs can be measured. Thus, the method assumes in a first step a uniform charge distribution

individually for each cosmic ray. This results in multiple magnetic field corrections for each cosmic ray which are combined into the corrected frame by superposition.

The Density Based Spatial Clustering of Applications with Noise (DBSCAN) algorithm is used to filter potential source directions which exceed isotropic expectations. Its parameters were tuned by maximizing the sensitivity of the method to detect anisotropies in simulated astrophysical scenarios. Here, the simulation uses the magnetic field model by Pshirkov and Tinyakov (PT11) whereas the evaluation of the scenarios with the filter method performs the magnetic field corrections with the model by Jansson and Farrar (JF12) to include the uncertainties in the GMF. The likelihood ratio test is based on a model combining a background and a signal distribution via a signal fraction. Here, the signal distribution uses the filtered candidates whereas the background distribution describes the exposure of the Pierre Auger observatory. Finally, the lower energy threshold, which mainly limits the number of events, is also scanned on various simulated astrophysical scenarios to maximize the overall sensitivity to detect an anisotropy. At a lower energy threshold of 12 EeV a sensitivity of more than  $3.4\sigma$  is achieved.

In the final part of the thesis the analysis is applied to a data set containing 13144 cosmic rays above 12 EeV measured by the surface detector array of the Pierre Auger Observatory. For the analysis with the JF12 field two regions were filtered. However, tests with isotropic arrival direction scenarios show that such filtered directions are compatible with isotropy at a level of 2.15 standard deviations. When using the PT11 field, only one region could be filtered leading to a compatibility within 1.24 standard deviations. A possible explanation for the compatibility with isotropic scenarios is that the mismatch between the galactic magnetic field realized in nature and the used models is greater than the mismatch between the PT11 and JF12 model used to tune the analysis. Another option is that the cosmic rays do originate from many different sources each contributing only a small fraction. For future analyses both, better knowledge of the galactic magnetic field and the charges of cosmic rays are required.

# Bibliography

- [1] United Nations Scientific Committee on the Effects of Atomic Radiation, *Sources, Effects and Risks of Ionizing Radiation, United Nations Scientific Committee on the Effects of Atomic Radiation (Unscear) 2017 Report*, United Nations Publications, 2018.
- [2] P. Auger *et al.*, *Extensive Cosmic-Ray Showers*, *Reviews of Modern Physics*, 11 (1939), pp. 288–291.
- [3] W. Kolhörster, I. Matthes, and E. Weber, *Gekoppelte Höhenstrahlen*, *Die Naturwissenschaften*, 26 (1938), pp. 576–576.
- [4] B. Rossi, *Risultati della Missione scientifica in Eritrea per lo studio della radiazione penetrante (Raggi cosmici). Considerazioni teoriche sull'influenza del campo magnetico terrestre e dell'assorbimento atmosferico sopra la distribuzione di intensità della radiazione penetrante*, *La Ricerca Scientifica. Supplemento*, 1(9-10) (1934), pp. 561–574.
- [5] A. Aab *et al.*, *An Indication of Anisotropy in Arrival Directions of Ultra-high-energy Cosmic Rays through Comparison to the Flux Pattern of Extragalactic Gamma-Ray Sources*, *The Astrophysical Journal*, 853 (2018), p. L29.
- [6] A. Aab *et al.*, *Observation of a large-scale anisotropy in the arrival directions of cosmic rays above  $8 \times 10^{18}$  eV*, *Science*, 357 (2017), pp. 1266–1270.
- [7] P. P. Kronberg, *Extragalactic magnetic fields*, *Reports on Progress in Physics*, 57 (1994), pp. 325–382.
- [8] R. Beck, F. A. Aharonian, W. Hofmann, and F. Rieger, *Galactic and Extragalactic Magnetic Fields*, in *Proceedings of the 4th International Meeting on High Energy Gamma-Ray Astronomy*, vol. 1085, American Institute of Physics, 2008, p. 83.
- [9] B. G. Keilhauer, *Investigation of atmospheric effects on the development of extensive air showers and their detection with the Pierre Auger Observatory*, PhD thesis, Karlsruhe, Forschungszentrum, 2004.
- [10] D. Heck *et al.*, *CORSIKA: a Monte Carlo code to simulate extensive air showers.*, Forschungszentrum Karlsruhe GmbH, 1998.
- [11] J. Matthews, *A Heitler model of extensive air showers*, *Astroparticle Physics*, 22 (2005), pp. 387–397.

- [12] T. Bergmann *et al.*, *One-dimensional hybrid approach to extensive air shower simulation*, *Astroparticle Physics*, 26 (2007), pp. 420–432.
- [13] R. Engel, D. Heck, and T. Pierog, *Extensive Air Showers and Hadronic Interactions at High Energy*, *Annual Review of Nuclear and Particle Science*, 61 (2011), pp. 467–489.
- [14] W. Heitler, *Quantum theory of radiation*, Oxford University Press, London, 1954.
- [15] M. Tanabashi *et al.*, *Review of Particle Physics*, *Physical Review D*, 98 (2018), p. 030001.
- [16] S. Jennings, *The mean free path in air*, *Journal of Aerosol Science*, 19 (1988), pp. 159–166.
- [17] M. Spurio, *Particles and Astrophysics*, Springer-Verlag GmbH, 2014.
- [18] T. K. Gaisser, *Cosmic Rays and Particle Physics*, Cambridge University Press, 1991.
- [19] T. Pierog *et al.*, *EPOS LHC: Test of collective hadronization with data measured at the CERN Large Hadron Collider*, *Physical Review C*, 92 (2015), p. 034906.
- [20] R. Engel *et al.*, *The hadronic interaction model Sibyll 2.3c and Feynman scaling*, in *Proceedings of 35th International Cosmic Ray Conference — PoS(ICRC2017)*, Bexco, Busan, Korea, 2017, p. 301.
- [21] A. Fedynitch *et al.*, *The hadronic interaction model Sibyll-2.3c and inclusive lepton fluxes*, [arXiv:1806.04140], (2018).
- [22] S. Ostapchenko, *Monte Carlo treatment of hadronic interactions in enhanced Pomeron scheme: QGSJET-II model*, *Physical Review D*, 83 (2011), p. 014018.
- [23] J. Abraham *et al.*, *Measurement of the energy spectrum of cosmic rays above  $10^{18}$  eV using the Pierre Auger Observatory*, *Physics Letters B*, 685 (2010), pp. 239–246.
- [24] J. Bellido *et al.*, *Muon content of extensive air showers: Comparison of the energy spectra obtained by the Sydney University Giant Air-shower Recorder and by the Pierre Auger Observatory*, *Physical Review D*, 98 (2018), p. 023014.
- [25] T. K. Gaisser and A. M. Hillas, *Reliability of the method of constant intensity cuts for reconstructing the average development of vertical showers*, in *Proceedings of the 15th International Cosmic Ray Conference — (ICRC1977)*, vol. 8, Plovdiv, Bulgaria, 1977, pp. 353–357.
- [26] K. Greisen, *Cosmic Ray Showers*, *Annual Review of Nuclear Science*, 10 (1960), pp. 63–108.

- [27] K. Kamata and J. Nishimura, *The Lateral and the Angular Structure Functions of Electron Showers*, Progress of Theoretical Physics Supplement, 6 (1958), pp. 93–155.
- [28] K.-H. Kampert and M. Unger, *Measurements of the cosmic ray composition with air shower experiments*, Astroparticle Physics, 35 (2012), pp. 660–678.
- [29] R. Coy, G. Cunningham, C. Pryke, and A. Watson, *The lateral distribution of extensive air showers produced by cosmic rays above 1019 eV as measured by water-Čerenkov detectors*, Astroparticle Physics, 6 (1997), pp. 263–270.
- [30] T. Antoni *et al.*, *Electron, muon, and hadron lateral distributions measured in air showers by the KASCADE experiment*, Astroparticle Physics, 14 (2001), pp. 245–260.
- [31] A. A. Lagutin, R. I. Raikin, N. Inoue, and A. Misaki, *Electron lateral distribution in air showers: scaling formalism and its implications*, Journal of Physics G: Nuclear and Particle Physics, 28 (2002), pp. 1259–1274.
- [32] Markus Roth *for the Pierre Auger Collaboration*, *The Lateral distribution function of shower signals in the surface detector of the Pierre Auger Observatory*, in Proceedings of the 28th International Cosmic Ray Conference (ICRC2003), Tsukuba, Japan, 2003, pp. 333–336.
- [33] B. R. Dawson *for the Pierre Auger Collaboration*, *Hybrid Performance of the Pierre Auger Observatory*, in Proceedings of the 30th International Cosmic Ray Conference — (ICRC2007), vol. 4, Merida, Yucatan, Mexico, 2007, pp. 425–428.
- [34] I. Allekotte *et al.*, *The surface detector system of the Pierre Auger Observatory*, Nuclear Instruments and Methods in Physics Research Section A: Accelerators, Spectrometers, Detectors and Associated Equipment, 586 (2008), pp. 409–420.
- [35] A. Aab *et al.*, *Energy estimation of cosmic rays with the Engineering Radio Array of the Pierre Auger Observatory*, Physical Review D, 93 (2016), p. 122005.
- [36] A. Aab *et al.*, *Measurement of the Radiation Energy in the Radio Signal of Extensive Air Showers as a Universal Estimator of Cosmic-Ray Energy*, Physical Review Letters, 116 (2016), p. 241101.
- [37] A. Aab *et al.*, *Calibration of the logarithmic-periodic dipole antenna (LPDA) radio stations at the Pierre Auger Observatory using an octocopter*, Journal of Instrumentation, 12 (2017), pp. T10005–T10005.
- [38] Ewa Holt *for the Pierre Auger Collaboration*, *Recent Results of the Auger Engineering Radio Array (AERA)*, in Proceedings of the 35th International Cosmic Ray Conference — PoS(ICRC2017), vol. 35, Bexco, Busan, Korea, 2017, p. 492.

- [39] A. Aab *et al.*, *The Pierre Auger Cosmic Ray Observatory*, Nuclear Instruments and Methods in Physics Research Section A: Accelerators, Spectrometers, Detectors and Associated Equipment, 798 (2015), pp. 172–213.
- [40] A. Letessier-Selvon *for the Pierre Auger Collaboration*, *Highlights from the Pierre Auger Observatory*, Brazilian Journal of Physics, 44 (2014), pp. 560–570.
- [41] H. Barbosa, F. Catalani, J. Chinellato, and C. Dobrigkeit, *Determination of the calorimetric energy in extensive air showers*, Astroparticle Physics, 22 (2004), pp. 159–166.
- [42] M. Risse and D. Heck, *Energy release in air showers*, Astroparticle Physics, 20 (2004), pp. 661–667.
- [43] Markus Roth *for the Pierre Auger Collaboration*, *Measurement of the UHECR energy spectrum using data from the Surface Detector of the Pierre Auger Observatory*, in Proceedings of the 30th International Cosmic Ray Conference — (ICRC2007), vol. 4, Merida, Yucatan, Mexico, 2007, pp. 327–330.
- [44] Petr Nečesal *for the Pierre Auger Collaboration*, *The Fluorescence Detector of the Pierre Auger Observatory*, Journal of Physics: Conference Series, 293 (2011), p. 012036.
- [45] J. Abraham *et al.*, *The fluorescence detector of the Pierre Auger Observatory*, Nuclear Instruments and Methods in Physics Research Section A: Accelerators, Spectrometers, Detectors and Associated Equipment, 620 (2010), pp. 227–251.
- [46] Paul Sommers *for the Pierre Auger Collaboration*, *First estimate of the primary cosmic ray energy spectrum above 3-EeV from the Pierre Auger Observatory*, in Proceedings of the 29th International Cosmic Ray Conference (ICRC2005), Pune, India, 2005, pp. 387, [arXiv:astro-ph/0507150].
- [47] Enrique Varela *for the Pierre Auger Collaboration*, *The low-energy extensions of the Pierre Auger Observatory*, Journal of Physics: Conference Series, 468 (2013), p. 012013.
- [48] A. Aab *et al.*, *Muon counting using silicon photomultipliers in the AMIGA detector of the Pierre Auger observatory*, Journal of Instrumentation, 12 (2017), pp. P03002–P03002.
- [49] A. Aab *et al.*, *The Pierre Auger Observatory Upgrade - Preliminary Design Report*, [arXiv:1604.03637], (2016).
- [50] N. L. Grigorov, V. E. Nesterov, and I. D. Rappoport, *Measurements of particle spectra on the proton 1, 2, 3 satellites*, Sovj. J. Nucl. Phys, 11 (1970), pp. 1058–1067.
- [51] N. L. Grigorov, V. E. Nesterov, and I. D. Rappoport, in Proceedings of the 12th International Cosmic Ray Conference — (ICRC1971), vol. 1, Hobart, Australia, 1971, pp. 1746–1752.

- [52] K. Asakimori *for the JACEE Collaboration*, *Energy spectra and composition of cosmic rays above 1 TeV per nucleon.*, in Proceedings of the 22nd International Cosmic Ray Conference (ICRC1991), vol. 2, Dublin, Ireland, 1991, pp. 57–60.
- [53] K. Asakimori *for the JACEE Collaboration*, *Energy spectra of protons and helium nuclei above 5 TeV/nucleon.*, in Proceedings of the 22nd International Cosmic Ray Conference (ICRC1991), vol. 2, Dublin, Ireland, 1991, pp. 97–100.
- [54] T. V. Danilova *et al.*, *The Energy Spectrum of the Primary Cosmic Rays in the Range  $10^{13}$  -  $10^{16}$  eV*, in Proceedings of the 15th International Cosmic Ray Conference (ICRC1977), vol. 8, Budapest, Bulgaria, 1977, p. 129.
- [55] Y. A. Fomin *et al.*, *Energy Spectrum of Cosmic Rays at Energies of  $5 \times 10^{15}$  –  $5 \times 10^{17}$  eV*, in Proceedings of the 22nd International Cosmic Ray Conference (ICRC1991), vol. 2, Dublin, Ireland, 1991, p. 85.
- [56] M. Amenomori *et al.*, *The Cosmic-Ray Energy Spectrum between 10 14.5 and 10 16.3 eV Covering the “Knee” Region*, *The Astrophysical Journal*, 461 (1996), p. 408.
- [57] M. Nagano *et al.*, *Energy spectrum of primary cosmic rays between  $10^{14.5}$  and  $10^{18}$  eV*, *Journal of Physics G: Nuclear Physics*, 10 (1984), pp. 1295–1310.
- [58] F. Arqueros *et al.*, *Energy spectrum and chemical composition of cosmic rays between 0.3 and 10 PeV determined from the cherenkov-light and charged-particle distributions in air showers*, *Astronomy & Astrophysics*, 359 (2000), pp. 682–694.
- [59] Zhen Cao *for the Hires/Mia Collaboration*, *Measurement of the Cosmic Ray Energy Spectrum and Composition from  $10^{17}$  to  $10^{18.3}$  eV Using a Hybrid Technique*, in Proceedings of the 27th International Cosmic Ray Conference — PoS(ICRC2001), vol. 1, Hamburg, Germany, 2001, p. 374.
- [60] M. Amenomori *et al.*, *The All-Particle Spectrum of Primary Cosmic Rays in the Wide Energy Range from  $10^{14}$  to  $10^{17}$  eV Observed with the Tibet-III Air-Shower Array*, *The Astrophysical Journal*, 678 (2008), pp. 1165–1179.
- [61] W. D. Apel *et al.*, *Kneelike Structure in the Spectrum of the Heavy Component of Cosmic Rays Observed with KASCADE-Grande*, *Physical Review Letters*, 107 (2011), p. 171104.
- [62] R. U. Abbasi *et al.*, *First Observation of the Greisen-Zatsepin-Kuzmin Suppression*, *Physical Review Letters*, 100 (2008), p. 101101.
- [63] J. Abraham *et al.*, *Observation of the Suppression of the Flux of Cosmic Rays above  $4 \times 10^{19}$  eV*, *Physical Review Letters*, 101 (2008), p. 061101.
- [64] Dmitri Ivanov *for the Telescope Array Collaboration*, *TA Spectrum Summary*, in Proceedings of the 34th International Cosmic Ray Conference — PoS(ICRC2015), The Hague, The Netherlands, 2016, p. 349.

- [65] D. J. Bird *et al.*, *The cosmic-ray energy spectrum observed by the Fly's Eye*, *The Astrophysical Journal*, 424 (1994), pp. 491–502.
- [66] T. Stanev, P. L. Biermann, and T. K. Gaisser, *Cosmic rays. IV. The spectrum and chemical composition above  $10^7$  GeV*, *Astronomy & Astrophysics*, 274 (1993), p. 902.
- [67] V. S. Ptuskin *et al.*, *Diffusion and drift of very high energy cosmic rays in galactic magnetic fields*, *Astronomy and Astrophysics*, 268 (1993), pp. 726–735.
- [68] J. Candia, L. N. Epele, and E. Roulet, *Cosmic ray photodisintegration and the knee of the spectrum*, *Astroparticle Physics*, 17 (2002), pp. 23–33.
- [69] D. Kazanas and A. Nicolaidis, *Letter: Cosmic Rays and Large Extra Dimensions*, *General Relativity and Gravitation*, 35 (2003), pp. 1117–1123.
- [70] J. R. Hörandel, *Models of the knee in the energy spectrum of cosmic rays*, *Astroparticle Physics*, 21 (2004), pp. 241–265.
- [71] A. Haungs *et al.*, *Investigating the 2nd knee: The KASCADE-Grande experiment*, *Journal of Physics: Conference Series*, 47 (2006), pp. 238–247.
- [72] D. R. Bergman and J. W. Belz, *Cosmic rays: the Second Knee and beyond*, *Journal of Physics G: Nuclear and Particle Physics*, 34 (2007), pp. R359–R400.
- [73] J. R. Hörandel, *Cosmic Rays from the Knee to the Second Knee:  $10^{14}$  to  $10^{18}$  eV*, *Modern Physics Letters A*, 22 (2007), pp. 1533–1551.
- [74] T. Abu-Zayyad *et al.*, *The Knee and the Second Knee of the Cosmic-Ray Energy Spectrum*, [arXiv:1803.07052], (2018).
- [75] Francesco Fenu *for the Pierre Auger Collaboration*, *The cosmic ray energy spectrum measured using the Pierre Auger Observatory*, in *Proceedings of the 35th International Cosmic Ray Conference — PoS(ICRC2017)*, Bexco, Busan, Korea, 2017, p. 486.
- [76] D. Ivanov *et al.*, *Report of the Telescope Array - Pierre Auger Observatory Working Group on Energy Spectrum*, in *Proceedings of the 35th International Cosmic Ray Conference — PoS(ICRC2017)*, Bexco, Busan, Korea, 2017, p. 498.
- [77] A. Aab *et al.*, *Evidence for a mixed mass composition at the ‘ankle’ in the cosmic-ray spectrum*, *Physics Letters B*, 762 (2016), pp. 288–295.
- [78] P. Erdogdu *et al.*, *The dipole anisotropy of the 2 Micron All-Sky Redshift Survey*, *Monthly Notices of the Royal Astronomical Society*, 368 (2006), pp. 1515–1526.
- [79] R. Jansson and G. R. Farrar, *A new Model of the Galactic Magnetic Field*, *The Astrophysical Journal*, 757 (2012), p. 14.

- [80] M. F. Skrutskie *et al.*, *The Two Micron All Sky Survey (2MASS)*, *The Astronomical Journal*, 131 (2006), pp. 1163–1183.
- [81] A. Aab *et al.*, *Multi-resolution anisotropy studies of ultrahigh-energy cosmic rays detected at the Pierre Auger Observatory*, *Journal of Cosmology and Astroparticle Physics*, 2017 (2017), pp. 026–026.
- [82] P. Abreu *et al.*, *A search for anisotropy in the arrival directions of ultra high energy cosmic rays recorded at the Pierre Auger Observatory*, *Journal of Cosmology and Astroparticle Physics*, 2012 (2012), pp. 040–040.
- [83] P. Abreu *et al.*, *Search for signatures of magnetically-induced alignment in the arrival directions measured by the Pierre Auger Observatory*, *Astroparticle Physics*, 35 (2012), pp. 354–361.
- [84] A. Aab *et al.*, *Searches for Large-scale Anisotropy in the Arrival Directions of Cosmic Rays detected above Energy of  $10^{19}$  eV at the Pierre Auger Observatory and the Telescope Array*, *The Astrophysical Journal*, 794 (2014), p. 172.
- [85] R. U. Abbasi *et al.*, *Indications of Intermediate-scale Anisotropy of Cosmic Rays with Energy greater than 57 EeV in the Northern Sky Measured with the Surface Detector of the Telescope Array Experiment*, *The Astrophysical Journal*, 790 (2014), p. L21.
- [86] A. Aab *et al.*, *Searches for Anisotropies in the Arrival Directions of the Highest Energy Cosmic Rays detected by the Pierre Auger Observatory*, *The Astrophysical Journal*, 804 (2015), p. 15.
- [87] A. Aab *et al.*, *Combined fit of spectrum and composition data as measured by the Pierre Auger Observatory*, *Journal of Cosmology and Astroparticle Physics*, 2017 (2017), pp. 038–038.
- [88] B. P. Abbott *et al.*, *Multi-messenger Observations of a Binary Neutron Star Merger*, *The Astrophysical Journal*, 848 (2017), p. L12.
- [89] A. Albert *et al.*, *Search for High-energy Neutrinos from Binary Neutron Star Merger GW170817 with ANTARES, IceCube, and the Pierre Auger Observatory*, *The Astrophysical Journal*, 850 (2017), p. L35.
- [90] The Pierre Auger Collaboration, Telescope Array Collaboration, IceCube Collaboration, *Search for correlations between the arrival directions of IceCube neutrino events and ultrahigh-energy cosmic rays detected by the Pierre Auger Observatory and the Telescope Array*, *Journal of Cosmology and Astroparticle Physics*, 2016 (2016), pp. 037–037.
- [91] Michael Unger *for the Pierre Auger Collaboration*, *Highlights from the Pierre Auger Observatory*, in *Proceedings of the 35th International Cosmic Ray Conference — PoS(ICRC2017)*, Bexco, Busan, Korea, 2017, p. 1102.

- [92] Patricia Sanchez-Lucas *for the Pierre Auger Collaboration*,  *$X_{\max}$  measurements and tests of hadronic models using the surface detector of the Pierre Auger Observatory*, in Proceedings of the 35th International Cosmic Ray Conference — PoS(ICRC2017), Bexco, Busan, Korea, 2017, p. 495.
- [93] A. Aab *et al.*, *Inferences on mass composition and tests of hadronic interactions from 0.3 to 100 EeV using the water-Cherenkov detectors of the Pierre Auger Observatory*, Physical Review D, 96 (2017), p. 122003.
- [94] Ariel Bridgeman *for the Pierre Auger Collaboration*, *Shower universality reconstruction of data from the Pierre Auger Observatory and validations with hadronic interaction models*, in Proceedings of the 35th International Cosmic Ray Conference — PoS(ICRC2017), Bexco, Busan, Korea, 2017, p. 323.
- [95] A. Bridgeman, *Determining the Mass Composition of Ultra-high Energy Cosmic Rays Using Air Shower Universality*, PhD thesis, Karlsruhe School of Elementary Particle and Astroparticle Physics: Science and Technology (KSETA), 2018.
- [96] M. Erdmann, J. Glombitza, and D. Walz, *A deep learning-based reconstruction of cosmic ray-induced air showers*, Astroparticle Physics, 97 (2018), pp. 46–53.
- [97] A. Aab *et al.*, *Depth of maximum of air-shower profiles at the Pierre Auger Observatory. I. Measurements at energies above 1017.8 eV*, Physical Review D, 90 (2014), p. 122005.
- [98] V. de Souza *et al.*, *Testing the agreement between the  $X_{\max}$  distributions measured by the Pierre Auger and Telescope Array Observatories*, in Proceedings of the 35th International Cosmic Ray Conference — PoS(ICRC2017), Bexco, Busan, Korea, 2017, p. 522.
- [99] T. W. Anderson and D. A. Darling, *Asymptotic Theory of Certain "Goodness of Fit" Criteria Based on Stochastic Processes*, The Annals of Mathematical Statistics, 23 (1952), pp. 193–212.
- [100] A. N. Kolmogorow, *Sulla determinazione empirica di una legge di distribuzione*, Giornale dell'Istituto Italiano degli Attuari, (1933), p. 83–91.
- [101] N. Smirnov, *Table for Estimating the Goodness of Fit of Empirical Distributions*, The Annals of Mathematical Statistics, 19 (1948), pp. 279–281.
- [102] A. Aab *et al.*, *Depth of maximum of air-shower profiles at the Pierre Auger Observatory. II. Composition implications*, Physical Review D, 90 (2014), p. 122006.
- [103] M. D. Domenico, M. Settimo, S. Riggi, and E. Bertin, *Reinterpreting the development of extensive air showers initiated by nuclei and photons*, Journal of Cosmology and Astroparticle Physics, 2013 (2013), pp. 050–050.

- [104] D. Walz, *Constraining models of the extragalactic cosmic ray origin with the Pierre Auger Observatory*, PhD thesis, RWTH Aachen University, 2016.
- [105] David Wittkowski *for the Pierre Auger Collaboration*, *Reconstructed properties of the sources of UHECR and their dependence on the extragalactic magnetic field*, in Proceedings of the 35th International Cosmic Ray Conference — PoS(ICRC2017), Bexco, Busan, Korea, 2017, p. 563.
- [106] V. Berezhinsky, M. Kachelrieß, and A. Vilenkin, *Ultra-high Energy Cosmic Rays without Greisen-Zatsepin-Kuzmin Cutoff*, Physical Review Letters, 79 (1997), pp. 4302–4305.
- [107] M. Birkel and S. Sarkar, *Extremely high energy cosmic rays from relic particle decays*, Astroparticle Physics, 9 (1998), pp. 297–309.
- [108] I. F. M. Albuquerque and C. P. de los Heros, *Closing the window on strongly interacting dark matter with IceCube*, Physical Review D, 81 (2010), p. 063510.
- [109] C. T. Hill, *Monopolonium*, Nuclear Physics B, 224 (1983), pp. 469–490.
- [110] T. Weiler, *Resonant Absorption of Cosmic-Ray Neutrinos by the Relic-Neutrino Background*, Physical Review Letters, 49 (1982), pp. 234–237.
- [111] D. Fargion, B. Mele, and A. Salis, *Ultra-High-Energy Neutrino Scattering onto Relic Light Neutrinos in the Galactic Halo as a Possible Source of the Highest Energy Extragalactic Cosmic Rays*, The Astrophysical Journal, 517 (1999), pp. 725–733.
- [112] J. Abraham *et al.*, *An upper limit to the photon fraction in cosmic rays above  $10^{19}$  eV from the Pierre Auger Observatory*, Astroparticle Physics, 27 (2007), pp. 155–168.
- [113] J. Abraham *et al.*, *Upper limit on the cosmic-ray photon flux above  $10^{19}$  eV using the surface detector of the Pierre Auger Observatory*, Astroparticle Physics, 29 (2008), pp. 243–256.
- [114] J. Abraham *et al.*, *Upper limit on the cosmic-ray photon fraction at EeV energies from the Pierre Auger Observatory*, Astroparticle Physics, 31 (2009), pp. 399–406.
- [115] R. Abbasi *et al.*, *An absence of neutrinos associated with cosmic-ray acceleration in  $\Gamma$ -ray bursts*, Nature, 484 (2012), pp. 351–354.
- [116] A. Aab *et al.*, *Search for photons with energies above  $10^{18}$  eV using the hybrid detector of the Pierre Auger Observatory*, Journal of Cosmology and Astroparticle Physics, 2017 (2017), pp. 009–009.
- [117] B. J. Kavanagh, *Earth scattering of superheavy dark matter: Updated constraints from detectors old and new*, Physical Review D, 97 (2018), p. 123013.

- 
- [118] W. F. G. Swann, *A Mechanism of Acquirement of Cosmic-Ray Energies by Electrons*, *Physical Review*, 43 (1933), pp. 217–220.
- [119] T. G. Cowling, *The Magnetic Field of Sunspots*, *Monthly Notices of the Royal Astronomical Society*, 94 (1933), pp. 39–48.
- [120] R. Protheroe and P. Johnson, *Propagation of ultra high energy protons and gamma rays over cosmological distances and implications for topological defect models*, *Astroparticle Physics*, 4 (1996), pp. 253–269.
- [121] R. Protheroe and P. Johnson, *Propagation of ultra high energy protons and gamma rays over cosmological distances and implications for topological defect models, Erratum*, *Astroparticle Physics*, 5 (1996), p. 215.
- [122] E. Fermi, *On the Origin of the Cosmic Radiation*, *Physical Review*, 75 (1949), pp. 1169–1174.
- [123] J. G. Kirk and P. Duffy, *Particle acceleration and relativistic shocks*, *Journal of Physics G: Nuclear and Particle Physics*, 25 (1999), pp. R163–R194.
- [124] R. D. Blandford and J. P. Ostriker, *Particle acceleration by astrophysical shocks*, *The Astrophysical Journal*, 221 (1978), p. L29.
- [125] A. R. Bell, *The acceleration of cosmic rays in shock fronts - I*, *Monthly Notices of the Royal Astronomical Society*, 182 (1978), pp. 147–156.
- [126] R. J. Protheroe and R. W. Clay, *Ultra High Energy Cosmic Rays*, *Publications of the Astronomical Society of Australia*, 21 (2004), pp. 1–22.
- [127] A. M. Hillas, *The Origin of Ultra-High-Energy Cosmic Rays*, *Annual Review of Astronomy and Astrophysics*, 22 (1984), pp. 425–444.
- [128] T. Winchen, *The Principal Axes of the Directional Energy Distribution of Cosmic Rays Measured with the Pierre Auger Observatory*, PhD thesis, RWTH Aachen University, 2013.
- [129] A. S. Wilson and E. J. M. Colbert, *The difference between radio-loud and radio-quiet active galaxies*, *The Astrophysical Journal*, 438 (1995), p. 62.
- [130] W. H. Baumgartner *et al.*, *The 70 Month Swift-bat All-sky Hard X-ray Survey*, *The Astrophysical Journal Supplement Series*, 207 (2013), p. 19.
- [131] M.-P. Véron-Cetty and P. Véron, *A catalogue of quasars and active nuclei: 13th edition*, *Astronomy & Astrophysics*, 518 (2010), p. A10.
- [132] M. R. George *et al.*, *On active galactic nuclei as sources of ultra-high energy cosmic rays*, *Monthly Notices of the Royal Astronomical Society: Letters*, 388 (2008), pp. L59–L63.

- [133] J. Abraham *et al.*, *Correlation of the highest-energy cosmic rays with the positions of nearby active galactic nuclei*, *Astroparticle Physics*, 29 (2008), pp. 188–204.
- [134] P. Abreu *et al.*, *Update on the correlation of the highest energy cosmic rays with nearby extragalactic matter*, *Astroparticle Physics*, 34 (2010), pp. 314–326.
- [135] A. Aab *et al.*, *Large Scale Distribution of Ultra High Energy Cosmic Rays Detected at the Pierre Auger Observatory with Zenith Angles up to 80°*, *The Astrophysical Journal*, 802 (2015), p. 111.
- [136] C. Kouveliotou *et al.*, *An X-ray pulsar with a superstrong magnetic field in the soft  $\Gamma$ -ray repeater SGR1806 - 20*, *Nature*, 393 (1998), pp. 235–237.
- [137] S. Mereghetti, *The strongest cosmic magnets: soft gamma-ray repeaters and anomalous X-ray pulsars*, *The Astronomy and Astrophysics Review*, 15 (2008), pp. 225–287.
- [138] D. M. Siegel, R. Ciolfi, and L. Rezzolla, *Magnetically Driven Winds from Differentially Rotating Neutron Stars and X-ray Afterglows of Short Gamma-ray Bursts*, *The Astrophysical Journal*, 785 (2014), p. L6.
- [139] J. Arons, *Magnetars in the Metagalaxy: An Origin for Ultra-High-Energy Cosmic Rays in the Nearby Universe*, *The Astrophysical Journal*, 589 (2003), pp. 871–892.
- [140] B. P. Abbott *et al.*, *Gravitational Waves and Gamma-Rays from a Binary Neutron Star Merger: GW170817 and GRB 170817A*, *The Astrophysical Journal*, 848 (2017), p. L13.
- [141] B. P. Abbott *et al.*, *GW170817: Observation of Gravitational Waves from a Binary Neutron Star Inspiral*, *Physical Review Letters*, 119 (2017), p. 161101.
- [142] D. A. Frail *et al.*, *Beaming in Gamma-Ray Bursts: Evidence for a Standard Energy Reservoir*, *The Astrophysical Journal*, 562 (2001), pp. L55–L58.
- [143] W. S. Paciesas *et al.*, *The Fourth BATSE Gamma-Ray Burst Catalog (Revised)*, *The Astrophysical Journal Supplement Series*, 122 (1999), pp. 465–495.
- [144] D. Coward, *Open issues with the gamma-ray burst redshift distribution*, *New Astronomy Reviews*, 51 (2007), pp. 539–546.
- [145] T. M. Heckman, L. Armus, and G. K. Miley, *On the nature and implications of starburst-driven galactic superwinds*, *The Astrophysical Journal Supplement Series*, 74 (1990), p. 833.
- [146] L. A. Anchordoqui, G. E. Romero, and J. A. Combi, *Heavy nuclei at the end of the cosmic-ray spectrum?*, *Physical Review D*, 60 (1999), p. 103001.

- [147] P. P. Kronberg, R. Kothes, C. J. Salter, and P. Perillat, *Discovery of New Faint Radio Emission on  $8^\circ$  to  $3'$  Scales in the Coma Field, and Some Galactic and Extragalactic Implications*, *The Astrophysical Journal*, 659 (2007), pp. 267–274.
- [148] G. B. Taylor *et al.*, *Magnetic fields in the centre of the Perseus cluster*, *Monthly Notices of the Royal Astronomical Society*, 368 (2006), pp. 1500–1506.
- [149] A. Olinto, *Ultra high energy cosmic rays: the theoretical challenge*, *Physics Reports*, 333-334 (2000), pp. 329–348.
- [150] D. F. Torres and L. A. Anchordoqui, *Astrophysical origins of ultrahigh energy cosmic rays*, *Reports on Progress in Physics*, 67 (2004), pp. 1663–1730.
- [151] K. V. Ptitsyna and S. V. Troitsky, *Physical conditions in potential accelerators of ultra-high-energy cosmic rays: updated Hillas plot and radiation-loss constraints*, *Physics-Uspekhi*, 53 (2010), pp. 691–701.
- [152] R. Protheroe and P. Biermann, *A new estimate of the extragalactic radio background and implications for ultra-high-energy  $\Gamma$ -ray propagation*, *Astroparticle Physics*, 6 (1996), pp. 45–54.
- [153] A. Domínguez *et al.*, *Extragalactic background light inferred from AEGIS galaxy-SED-type fractions*, *Monthly Notices of the Royal Astronomical Society*, 410 (2010), pp. 2556–2578.
- [154] R. J. Protheroe, *Topics in cosmic-ray astrophysics*, Nova Science Publishing, New York, 1998, ch. Acceleration and Interaction of Ultra High Energy Cosmic Rays.
- [155] J. J. Condon *et al.*, *Resolving the Radio Source Background: Deeper Understanding through Confusion*, *The Astrophysical Journal*, 758 (2012), p. 23.
- [156] N. Fornengo, R. A. Lineros, M. Regis, and M. Taoso, *The isotropic radio background revisited*, *Journal of Cosmology and Astroparticle Physics*, 2014 (2014), pp. 008–008.
- [157] D. J. Fixsen *et al.*, *Arcade 2 Measurement of the Absolute Sky Brightness at 3-90 GHz*, *The Astrophysical Journal*, 734 (2011), p. 5.
- [158] A. A. Penzias and R. W. Wilson, *A Measurement of Excess Antenna Temperature at 4080 Mc/s.*, *The Astrophysical Journal*, 142 (1965), p. 419.
- [159] T. M. Kneiske, K. Mannheim, and D. H. Hartmann, *Implications of cosmological gamma-ray absorption*, *Astronomy & Astrophysics*, 386 (2002), pp. 1–11.
- [160] T. M. Kneiske and H. Dole, *A lower-limit flux for the extragalactic background light*, *Astronomy & Astrophysics*, 515 (2010), p. A19.

- [161] J. D. Finke, S. Razzaque, and C. D. Dermer, *Modeling the Extragalactic Background Light from Stars and Dust*, *The Astrophysical Journal*, 712 (2010), pp. 238–249.
- [162] R. C. Gilmore, R. S. Somerville, J. R. Primack, and A. Domínguez, *Semi-analytic modelling of the extragalactic background light and consequences for extragalactic gamma-ray spectra*, *Monthly Notices of the Royal Astronomical Society*, 422 (2012), pp. 3189–3207.
- [163] K. Greisen, *End to the Cosmic-Ray Spectrum?*, *Physical Review Letters*, 16 (1966), pp. 748–750.
- [164] G. T. Zatsepin and V. A. Kuzmin, *Upper Limit of the Spectrum of Cosmic Rays*, *Journal of Experimental and Theoretical Physics Letters*, 4 (1966), p. 78.
- [165] M. Takeda *et al.*, *Energy determination in the Akeno Giant Air Shower Array experiment*, *Astroparticle Physics*, 19 (2003), pp. 447–462.
- [166] T. Abu-Zayyad *et al.*, *The Cosmic-Ray Energy Spectrum Observed with the Surface Detector of the Telescope Array Experiment*, *The Astrophysical Journal*, 768 (2013), p. L1.
- [167] D. Kümpel, *Multivariate Search for a Directional Excess of EeV Photons with the Pierre Auger Observatory*, PhD thesis, Bergische Universität Wuppertal, 2011.
- [168] T. Bister, M. Erdmann, M. Urban, and M. Wirtz, *Consistency Checks between the Search Radius of the Starburst Galaxy Analysis and Deflections by Cosmic Magnetic Fields*, Tech. Report GAP2018-003, 2018.
- [169] M. Erdmann, G. Müller, M. Urban, and M. Wirtz, *The nuclear window to the extragalactic universe*, *Astroparticle Physics*, 85 (2016), pp. 54–64.
- [170] A. Kolmogorov, *The Local Structure of Turbulence in Incompressible Viscous Fluid for Very Large Reynolds' Numbers*, *Akademiia Nauk SSSR Doklady*, 30 (1941), pp. 301–305.
- [171] S. Lee, A. V. Olinto, and G. Sigl, *Extragalactic Magnetic Field and the Highest Energy Cosmic Rays*, *The Astrophysical Journal*, 455 (1995), p. L21.
- [172] P. Tinyakov and I. Tkachev, *Deflections of cosmic rays in a random component of the Galactic magnetic field*, *Astroparticle Physics*, 24 (2005), pp. 32–43.
- [173] K. Dolag, D. Grasso, V. Springel, and I. Tkachev, *Constrained simulations of the magnetic field in the local Universe and the propagation of ultrahigh energy cosmic rays*, *Journal of Cosmology and Astroparticle Physics*, 2005 (2005), pp. 009–009.
- [174] A. Neronov, A. M. Taylor, C. Tchernin, and I. Vovk, *Measuring the correlation length of intergalactic magnetic fields from observations of gamma-ray induced cascades*, *Astronomy & Astrophysics*, 554 (2013), p. A31.

- [175] R. A. Batista *et al.*, *CRPropa 3—a public astrophysical simulation framework for propagating extraterrestrial ultra-high energy particles*, *Journal of Cosmology and Astroparticle Physics*, 2016 (2016), pp. 038–038.
- [176] G. Sigl, F. Miniati, and T. A. Enßlin, *Cosmic Magnetic Fields and Their Influence on Ultra-High Energy Cosmic Ray Propagation*, *Nuclear Physics B - Proceedings Supplements*, 136 (2004), pp. 224–233.
- [177] M. Erdmann *et al.*, *A Benchmark Scenario for UHECR Propagation*, Tech. Report GAP2012-138, 2012.
- [178] P. Abreu *et al.*, *Bounds on the density of sources of ultra-high energy cosmic rays from the Pierre Auger Observatory*, *Journal of Cosmology and Astroparticle Physics*, 2013 (2013), pp. 009–009.
- [179] T. Stanev, *Ultra-High-Energy Cosmic Rays and the Large-Scale Structure of the Galactic Magnetic Field*, *The Astrophysical Journal*, 479 (1997), pp. 290–295.
- [180] G. Giacinti, M. Kachelrieß, D. Semikoz, and G. Sigl, *Ultrahigh energy nuclei in the galactic magnetic field*, *Journal of Cosmology and Astroparticle Physics*, 2010 (2010), pp. 036–036.
- [181] S. Hackstein *et al.*, *Propagation of ultrahigh energy cosmic rays in extragalactic magnetic fields: a view from cosmological simulations*, *Monthly Notices of the Royal Astronomical Society*, 462 (2016), pp. 3660–3671.
- [182] G. Golup, D. Harari, S. Mollerach, and E. Roulet, *Source position reconstruction and constraints on the galactic magnetic field from ultra-high energy cosmic rays*, *Astroparticle Physics*, 32 (2009), pp. 269–277.
- [183] G. Golup, D. Harari, S. Mollerach, and E. Roulet, *Searching for signals of magnetic lensing in ultra-high energy cosmic rays*, *Journal of Cosmology and Astroparticle Physics*, 2011 (2011), pp. 006–006.
- [184] D. Harari, S. Mollerach, E. Roulet, and F. Sánchez, *Lensing of ultra-high energy cosmic rays in turbulent magnetic fields*, *Journal of High Energy Physics*, 2002 (2002), pp. 045–045.
- [185] G. Giacinti, M. Kachelrieß, D. Semikoz, and G. Sigl, *Ultrahigh energy nuclei in the turbulent Galactic magnetic field*, *Astroparticle Physics*, 35 (2011), pp. 192–200.
- [186] P. Tinyakov and I. Tkachev, *Tracing protons through the Galactic magnetic field: a clue for charge composition of ultra-high-energy cosmic rays*, *Astroparticle Physics*, 18 (2002), pp. 165–172.
- [187] M. S. Pshirkov, P. G. Tinyakov, P. P. Kronberg, and K. J. Newton-McGee, *Deriving the Global Structure of the Galactic Magnetic Field from Faraday Rotation Measures of Extragalactic Sources*, *The Astrophysical Journal*, 738 (2011), p. 192.

- [188] G. R. Farrar, *The Galactic magnetic field and ultrahigh-energy cosmic ray deflections*, *Comptes Rendus Physique*, 15 (2014), pp. 339–348.
- [189] A. Keivani, G. R. Farrar, and M. Sutherland, *Magnetic deflections of ultrahigh energy cosmic rays from Centaurus A*, *Astroparticle Physics*, 61 (2015), pp. 47–55.
- [190] G. R. Farrar, N. Awal, D. Khurana, and M. Sutherland, *The Galactic Magnetic Field and UHECR Optics*, in *Proceedings of the 34th International Cosmic Ray Conference — PoS(ICRC2015)*, The Hague, The Netherlands, 2016, p. 560.
- [191] G. R. Farrar and M. S. Sutherland, *Deflections of UHECRs in the Galactic magnetic field*, [arXiv:1711.02730], (2017).
- [192] M. Urban, M. Erdmann, and G. Mueller, *Investigation of the galactic magnetic field with ultra-high energy cosmic rays*, in *Proceedings of the 34th International Cosmic Ray Conference — PoS(ICRC2015)*, The Hague, The Netherlands, 2016, p. 557.
- [193] J. M. Cordes and T. J. W. Lazio, *NE2001.I. A New Model for the Galactic Distribution of Free Electrons and its Fluctuations*, [arXiv:astro-ph/0207156], (2002).
- [194] D. Harari, S. Mollerach, and E. Roulet, *Signatures of galactic magnetic lensing upon ultra high energy cosmic rays*, *Journal of High Energy Physics*, 2000 (2000), pp. 035–035.
- [195] H.-P. Bretz *et al.*, *PARSEC: A parametrized simulation engine for ultra-high energy cosmic ray protons*, *Astroparticle Physics*, 54 (2014), pp. 110–117.
- [196] K. M. Gorski *et al.*, *HEALPix: A Framework for High-Resolution Discretization and Fast Analysis of Data Distributed on the Sphere*, *The Astrophysical Journal*, 622 (2005), pp. 759–771.
- [197] R. Fisher, *Dispersion on a Sphere*, *Proceedings of the Royal Society A: Mathematical, Physical and Engineering Sciences*, 217 (1953), pp. 295–305.
- [198] G. Müller, *Eine Suche nach Quellen von extragalaktischer kosmischer Strahlung unter Verwendung von strukturierten Magnetfeldern und moderner Propagations-Software mit dem Pierre Auger Observatorium*, PhD thesis, RWTH Aachen University, 2016.
- [199] M. S. Pshirkov, P. G. Tinyakov, and F. R. Urban, *Mapping ultrahigh energy cosmic rays deflections through the turbulent galactic magnetic field with the latest rotation measure data*, *Monthly Notices of the Royal Astronomical Society*, 436 (2013), pp. 2326–2333.
- [200] R. Jansson and G. R. Farrar, *The Galactic Magnetic Field*, *The Astrophysical Journal*, 761 (2012), p. L11.

- [201] M. C. Beck *et al.*, *New constraints on modelling the random magnetic field of the MW*, *Journal of Cosmology and Astroparticle Physics*, 2016 (2016), pp. 056–056.
- [202] S. S. Wilks, *The Large-Sample Distribution of the Likelihood Ratio for Testing Composite Hypotheses*, *The Annals of Mathematical Statistics*, 9 (1938), pp. 60–62.
- [203] J. Abraham *et al.*, *Trigger and aperture of the surface detector array of the Pierre Auger Observatory*, *Nuclear Instruments and Methods in Physics Research Section A: Accelerators, Spectrometers, Detectors and Associated Equipment*, A613 (2010), pp. 29–39.
- [204] D. Allard *for the Pierre Auger Collaboration*, *Aperture calculation of the Pierre Auger Observatory surface detector*, in *Proceedings of the 29th International Cosmic Ray Conference — PoS(ICRC2005)*, Pune, India, 2005, pp. 71–74.
- [205] M. Urban, D. Mockler, and D. Veberič, *Observer Data Set for Anisotropy Studies including 4T5 Events*, Tech. Report GAP2018-034, 2018.
- [206] M. Erdmann, L. Geiger, J. Glombitza, and D. Schmidt, *Generating and Refining Particle Detector Simulations Using the Wasserstein Distance in Adversarial Networks*, *Computing and Software for Big Science*, 2 (2018), p. 4.
- [207] D. Veberič and M. Roth, *SD Reconstruction; Offline Reference Manual*, Tech. Report GAP2005-035, 2005.
- [208] Darko Veberič *for the Pierre Auger Collaboration*, *Estimation of Signal in Saturated Stations of Pierre Auger Surface Detector*, in *Proceedings of the 33rd International Cosmic Ray Conference — PoS(ICRC2013)*, vol. 44, Rio de Janeiro, Brazil, 2013, pp. 415–608, [arXiv:1307.5059, p.23].
- [209] C. Bonifazi *for the Pierre Auger Collaboration*, *The angular resolution of the Pierre Auger Observatory*, *Nuclear Physics B - Proceedings Supplements*, 190 (2009), pp. 20–25.
- [210] M. Ave *for the Pierre Auger Collaboration*, *Reconstruction accuracy of the surface detector array of the Pierre Auger Observatory*, in *Proceedings of the 30th International Cosmic Ray Conference (ICRC2007)*, vol. 4, Merida, Yucatan, Mexico, 2007, pp. 307–310.
- [211] J. A. J. Matthews *et al.*, *A parameterization of cosmic ray shower profiles based on shower width*, *Journal of Physics G: Nuclear and Particle Physics*, 37 (2010), p. 025202.
- [212] J. Abraham *et al.*, *A study of the effect of molecular and aerosol conditions in the atmosphere on air fluorescence measurements at the Pierre Auger Observatory*, *Astroparticle Physics*, 33 (2010), pp. 108–129.

- [213] Max Malacari *for the Pierre Auger Collaboration*, *Improvements to aerosol attenuation measurements at the Pierre Auger Observatory*, in Proceedings of the 35th International Cosmic Ray Conference — PoS(ICRC2017), Bexco, Busan, Korea, 2017, p. 398.
- [214] A. M. Hillas, J. D. Hollows, H. W. Hunter, and D. J. Marsden, *Calculations on the particle and energy-loss densities in extensive air showers at large axial distances*, in Proceedings of the 11th International Cosmic Ray Conference — (ICRC1969), vol. 3 of Acta Physica, Supplement to Volume 29, Budapest, Hungary, 1970, p. 533.
- [215] J. Hersil *et al.*, *Observations of Extensive Air Showers near the Maximum of Their Longitudinal Development*, Physical Review Letters, 6 (1961), pp. 22–23.
- [216] Alexander Schulz *for the Pierre Auger Collaboration*, *The measurement of the energy spectrum of cosmic rays above  $3 \times 10^{17}$  eV with the Pierre Auger Observatory*, in Proceedings of the 33rd International Cosmic Ray Conference — PoS(ICRC2013), vol. 44, Rio de Janeiro, Brazil, 2013, pp. 415–608, [arXiv:1307.5059, p.27].
- [217] A. Aab *et al.*, *Reconstruction of inclined air showers detected with the Pierre Auger Observatory*, Journal of Cosmology and Astroparticle Physics, 1408 (2014), p. 019.
- [218] A. Aab *et al.*, *Measurement of the cosmic ray spectrum above  $4 \times 10^{18}$  eV using inclined events detected with the Pierre Auger Observatory*, Journal of Cosmology and Astroparticle Physics, 2015 (2015), pp. 049–049.
- [219] P. Abreu *et al.*, *Large-scale Distribution of Arrival Directions of Cosmic Rays Detected above  $10^{18}$  eV at the Pierre Auger Observatory*, The Astrophysical Journal Supplement Series, 203 (2012), p. 34.
- [220] M. Urban, M. Erdmann, G. Müller, and M. Wirtz, *A Method of Searching for Origins of Cosmic Rays correcting for Galactic Field Deflections and Charge Composition*, in Proceedings of the 35th International Cosmic Ray Conference — PoS(ICRC2017), Bexco, Busan, Korea, 2017, p. 518.
- [221] M. Urban, M. Erdmann, and M. Wirtz, *Search for Local Structures in the Arrival Directions of Cosmic Rays using an Extragalactic Directional Filter Method*, Tech. Report GAP2018-054, 2018.
- [222] Ines Valino *for the Pierre Auger Collaboration*, *The flux of ultra-high energy cosmic rays after ten years of operation of the Pierre Auger Observatory*, in Proceedings of the 34th International Cosmic Ray Conference — PoS(ICRC2015), The Hague, The Netherlands, 2016, p. 271.
- [223] T. Bister, M. Urban, M. Wirtz, and M. Erdmann, *Investigation of the correlation between Starburst Galaxies and the arrival directions of ultrahigh energy cosmic rays*, Tech. Report GAP2018-053, 2018.

- [224] M. Ave *et al.*, *Anisotropy of the Highest-Energy Auger Events*, Tech. Report GAP2007-076, 2007.
- [225] T. Hebbeker, *Two-Point Correlation Function and Kolmogorov-Smirnov Test*, Tech. Report GAP2007-087, 2007.
- [226] Y. V. Petrov and J. L. Harton, *Constraints on the Galactic Magnetic Field with 2-point Cumulative Autocorrelation Function*, Tech. Report GAP2011-131, 2011.
- [227] S. Schulte, *Autocorrelation studies of the arrival directions of UHECRs measured by the surface detector of the Pierre Auger Observatory*, PhD thesis, RWTH Aachen University, 2011.
- [228] A. Aab *et al.*, *Search for patterns by combining cosmic-ray energy and arrival directions at the Pierre Auger Observatory*, The European Physical Journal C, 75 (2015), p. 269.
- [229] M. Ester, H.-P. Kriegel, J. Sander, and X. Xu, *A density-based algorithm for discovering clusters in large spatial databases with noise*, in Proceedings of the Second International Conference on Knowledge Discovery and Data Mining (KDD-96), Menlo Park, California, 1996, pp. 226–231.
- [230] H. Steinhaus, *Sur la division des corp materiels en parties*, Bulletin of the Polish Academy of Sciences, 1 (1956), pp. 801–804.
- [231] J. Macqueen, *Some methods for classification and analysis of multivariate observations*, in Proceedings of the 5th Berkeley Symposium on Mathematical Statistics and Probability, vol. Vol. 1, Berkeley, California, USA, 1967, pp. 281–297.
- [232] W. E. Donath and A. J. Hoffman, *Lower Bounds for the Partitioning of Graphs*, IBM Journal of Research and Development, 17 (1973), pp. 420–425.
- [233] M. Fiedler, *Algebraic connectivity of graphs*, Czechoslovak Mathematical Journal, Vol. 23 (1973), pp. 298–305.
- [234] M. Cacciari, G. P. Salam, and G. Soyez, *FastJet user manual*, The European Physical Journal C, 72 (2012), p. 1896.
- [235] G. P. Salam and G. Soyez, *A practical seedless infrared-safe cone jet algorithm*, Journal of High Energy Physics, 2007 (2007), pp. 086–086.
- [236] F. Pedregosa *et al.*, *Scikit-learn: Machine Learning in Python*, Journal of Machine Learning Research, 12 (2011), pp. 2825–2830.
- [237] T. E. Oliphant, *Guide to NumPy*, <https://www.numpy.org/>, Trelgol Publishing, 2006.
- [238] E. Jones *et al.*, *SciPy: Open source scientific tools for Python*. <https://github.com/scipy/scipy>, 2001.

- [239] M. Urban, M. Wirtz, D. Walz, and G. Müller, *Astrotools - a lightweight python library for physics of ultra-high energy cosmic rays*. <https://git.rwth-aachen.de/astro/astrotools>, 2018.
- [240] J. D. Hunter, *Matplotlib: A 2D Graphics Environment*, Computing in Science & Engineering, 9 (2007), pp. 90–95.
- [241] H. P. Bretz *et al.*, *A development environment for visual physics analysis*, Journal of Instrumentation, 7 (2012), pp. T08005–T08005.
- [242] H.-P. Bretz *et al.*, *A Server-Client-Based Graphical Development Environment for Physics Analyses (VISPA)*, Journal of Physics: Conference Series, 396 (2012), p. 052015.
- [243] M. Erdmann *et al.*, *A Web-Based Development Environment for Collaborative Data Analysis*, Journal of Physics: Conference Series, 523 (2014), p. 012021.
- [244] M. Erdmann *et al.*, *A Browser-Based Multi-User Working Environment for Physicists*, Journal of Physics: Conference Series, 513 (2014), p. 062034.
- [245] M. Erdmann *et al.*, *A field study of data analysis exercises in a bachelor physics course using the internet platform VISPA*, European Journal of Physics, 35 (2014), p. 035018.
- [246] D. von Asseldonk *et al.*, *VISPA: Direct Access and Execution of Data Analyses for Collaborations*, Journal of Physics: Conference Series, 608 (2015), p. 012027.
- [247] D. Asseldonk *et al.*, *The VISPA Internet Platform for Students*, Nuclear and Particle Physics Proceedings, 273-275 (2016), pp. 2581–2583.
- [248] M. Urban *et al.*, *The VISPA internet platform for outreach, education and scientific research in various experiments*, Journal of Physics: Conference Series, 664 (2015), p. 032031.
- [249] M. Erdmann *et al.*, *Bringing Experiment Software to the Web with VISPA*, Journal of Physics: Conference Series, 762 (2016), p. 012008.
- [250] M. Erdmann *et al.*, *Experiment Software and Projects on the Web with VISPA*, Journal of Physics: Conference Series, 898 (2017), p. 072045.
- [251] M. Urban *et al.*, *The VISPA internet-platform in deep learning applications*, Journal of Physics: Conference Series, 1085 (2018), p. 042044.
- [252] J. Han, *The most updated results of the magnetic field structure of the Milky Way*, in Proceedings of the Ultra High Energy Cosmic Rays Conference (UHECR2018), Paris, France, 2018. In preparation.
- [253] J. L. Han, R. N. Manchester, W. van Straten, and P. Demorest, *Pulsar Rotation Measures and Large-scale Magnetic Field Reversals in the Galactic Disk*, The Astrophysical Journal Supplement Series, 234 (2018), p. 11.

- [254] J. Han, *Observing Interstellar and Intergalactic Magnetic Fields*, Annual Review of Astronomy and Astrophysics, 55 (2017), pp. 111–157.
- [255] M. Unger and G. R. Farrar, *Uncertainties in the Magnetic Field of the Milky Way*, in Proceedings of 35th International Cosmic Ray Conference — PoS(ICRC2017), Bexco, Busan, Korea, 2017, p. 558.

# Zusammenfassung

Zu den wichtigsten Fragen der Astroteilchenphysik zählen, wo und wie die ultrahochenergetische kosmische Strahlung (UHECRs) auf Energien weit über 1 EeV beschleunigt wird. Die Suche nach diesen Quellen stellt eine Herausforderung dar, da die kosmische Strahlung auf ihrem Weg zur Erde durch Magnetfelder abgelenkt wird und folglich die gemessenen Ankunftsrichtungen nicht direkt zu den Quellen zurück zeigen. Typischerweise wird bei den Magnetfeldern zwischen kleinskaligen Zufallsfeldern und strukturierten Feldern unterschieden. Ablenkungen in ersteren führen zu einer Verschmierung der Ankunftsrichtungen, ganz ähnlich zu einer Aufweitung eines Lichtstrahls in der Optik; Ablenkungen durch die strukturierten Felder sind gerichtet und von der Rigidität  $R = E/Z$  abhängig. Diese ist durch das Verhältnis aus Energie  $E$  und Ladung  $Z$  definiert. Insbesondere das galaktische Magnetfeld (GMF) mit Feldstärken von bis zu  $5 \mu\text{G}$ , trägt wesentlich zur Gesamtablenkung bei.

Im ersten Teil der Arbeit wurden diese Ablenkungen unter Verwendung von zwei Modellen des GMFs, die an Messungen von Faraday Rotationen und Synchrotron Emissionen angepasst sind, untersucht. Ein zentrales Ergebnis ist, dass diese Modelle die gerichteten Ablenkungen nur für Rigiditäten oberhalb von  $R = 6 \text{ EV}$  aussagekräftig beschreiben können. Darunter sind die Unterschiede in den Vorhersagen groß und beide Modelle sagen außerdem Ablenkungen voraus, die mit einer rein zufälligen Bewegung der Teilchen kompatibel sind. Darüber hinaus wurde festgestellt, dass die Unterschiede der Modelle in der Nähe der Milchstraße mit Latituden im Bereich von  $|l| < 19.5^\circ$  beträchtlich sind. Zusätzlich wurde diskutiert, dass das galaktische Magnetfeld Vorzugsrichtungen aufweist, bei denen die Durchlässigkeit für kosmische Strahlung erhöht ist, was zu einer inhomogenen Sicht auf das extragalaktische Universum führt. Schließlich wurde gezeigt, dass eine Quelle außerhalb der Galaxie auf der Erde von verschiedenen Richtungen aus beobachtet werden kann, was als Mehrfachabbildung bezeichnet wird.

Das erworbene Wissen über Magnetfelder wurde dann verwendet um ein neues Filterverfahren zu entwickeln, mit dem bandartige Strukturen in den Ankunftsrichtungen der kosmischen Strahlung aufgedeckt werden können. Diese Strukturen entstehen dadurch, dass UHECRs mit verschiedenen Rigiditäten in den strukturierten Feldern in leicht verschiedene Richtungen abgelenkt werden, ähnlich zu einem Spektrometer. Dabei werden kosmische Teilchen mit hohen Rigiditäten typischerweise in der Umgebung der extragalaktischen Quellrichtung beobachtet; kosmische Teilchen mit niedrigeren Rigiditäten weisen jedoch große Abstände zur Quellrichtung auf. Allgemein gefasst besteht die Idee der Methode daraus, zuerst Korrekturen der gemessenen Ankunftsrichtungen von UHECRs auf die Magnetfeldablenkungen durchzuführen, als nächstes Richtungen potentieller Quellkandidaten herauszufiltern und letztendlich diese Richtungen in einer Likelihood Analyse zu bewerten.

Diese Methode könnte theoretisch bei vollständigem Wissen über die Magnetfelder, die Energien und Ladungen der kosmischen Strahlung die Ausrichtungsmuster in den Ankunftsrichtungen zu den Quellrichtungen zusammenziehen. Es werden jedoch nur Ankunftsrichtungen und Energien aber nicht die Ladungen der UHECRs gemessen. Als Konsequenz daraus wurde eine Gleichverteilung für die Ladungen jedes kosmischen Teilchens angenommen. Dadurch wurden für jedes Teilchen mehrere Magnetfeldkorrekturen durchgeführt, die anschließend alle überlagert wurden.

Der Algorithmus „Density Based Spatial Clustering of Applications with Noise“ wurde verwendet, um potenzielle Quellrichtungen, die die isotropen Erwartungen übertreffen, aus dieser Überlagerung herauszufiltern. Seine Parameter wurden mit Hilfe von simulierten astrophysikalischen Szenarien so optimiert, dass die Sensitivität zur Erkennung von Anisotropien maximal ist. Dabei wurde in den Simulationen das Magnetfeldmodell von Pshirkov und Tinyakov (PT11) verwendet, während in der Auswertung der Szenarien mit der Filtermethode die Magnetfeldkorrekturen mit dem Modell von Jansson und Farrar (JF12) durchgeführt wurden, um die Unsicherheiten in den Vorhersagen durch verschiedene Modelle des GMFs abzubilden.

Das in der Auswertung verwendete Wahrscheinlichkeitsmodell kombiniert eine Hintergrund- und eine Signalverteilung über einen Signalanteil miteinander. Dabei verwendet die Signalverteilung die gefilterten Richtungen der Quellkandidaten, während die Hintergrundverteilung die Belichtung des Pierre Auger Observatoriums beschreibt. Schließlich wurde der untere Energieschwellenwert, der hauptsächlich die Anzahl der Ereignisse begrenzt, auch mit verschiedenen simulierten astrophysikalischen Szenarien gescannt, um die Gesamtsensitivität zur Erkennung einer Anisotropie zu maximieren. Dabei wurde bei einer unteren Energieschwelle von 12 EeV eine Sensitivität von mehr als  $3.4\sigma$  erreicht.

Im letzten Teil der Arbeit wurde die Analyse auf einen Datensatz angewandt, der mit dem Oberflächendetektor des Pierre Auger Observatoriums gemessen wurde und 13144 Ereignisse kosmischer Strahlung mit Energien über 12 EeV enthält. Dabei wurden in der Analyse mit dem JF12-Feld zwei Richtungen gefiltert. Tests mit isotropen Ankunftsrichtungsszenarien zeigten jedoch, dass solche gefilterten Richtungen mit Isotropie auf einem Niveau von 2.15 Standardabweichungen kompatibel sind. Bei Verwendung des PT11-Feldes konnte nur eine Richtung gefiltert werden, was zu einer Kompatibilität innerhalb von 1.24 Standardabweichungen führte. Eine mögliche Erklärung für die Kompatibilität mit isotropen Szenarien ist, dass die Diskrepanz zwischen dem in der Natur realisierten galaktischen Magnetfeld und den verwendeten Modellen größer ist als die Diskrepanz zwischen dem PT11- und JF12-Modell, welche beim Tuning der Analyse verwendet wird. Eine weitere Möglichkeit ist, dass die kosmischen Strahlen aus vielen verschiedenen Quellen stammen, diese aber jeweils nur zu einem kleinen Teil beitragen. Daraus kann geschlossen werden, dass für zukünftige Analysen sowohl eine bessere Kenntnis des galaktischen Magnetfeldes als auch der Ladungen der kosmischen Strahlung erforderlich sind.

# List of Publications

## Published articles with significant personal contribution

**Martin Erdmann, Martin Urban et al.**

”A field study of data analysis exercises in a bachelor physics course using the internet platform VISPA”

European Journal of Physics **35** 35018 (2014)

*The author of this thesis has participated in the field study, significantly contributed to the development of the VISPA web platform and to the design and setup of the underlying computing cluster. The text of the publication has been revised and copy-edited by the author of this thesis.*

**Martin Erdmann, Gero Müller, Martin Urban and Marcus Wirtz**

”The nuclear window to the extragalactic universe”

Astroparticle Physics **85** 54-64 (2016)

*The author of this thesis contributed significantly to the strategic development of the analysis technique to study various effects on cosmic rays from the galactic magnetic field, performed the execution of all partial analyses and provided all figures. The text of the publication has been revised and copy-edited by the author of this thesis.*

**Martin Erdmann, Lukas Geiger, David Schmidt, Martin Urban and Marcus Wirtz**

“Origins of Extragalactic Cosmic Ray Nuclei by Contracting Alignment Patterns induced in the Galactic Magnetic Field”

Astroparticle Physics, in press, doi:10.1016/j.astropartphys.2018.11.004

*The author of this thesis contributed to the strategic development of the analysis technique which can be considered as a refinement of the analysis method presented in this thesis. The text of the publication has been revised and copy-edited by the author of this thesis.*

## Conference Proceedings

**Martin Urban (for the VISPA group)**

“The VISPA internet platform for outreach, education and scientific research in various experiments”

Journal of Physics: Conference Series **664** 032031 (2015)

*The author of this thesis significantly contributed to the development of the VISPA web platform and to the design and setup of the underlying computing cluster. The text of the publication has been written by the author of this thesis and revised and copy-edited by the co-authors of the publication.*

**Martin Erdmann, Gero Müller, and Martin Urban**

“Investigation of the galactic magnetic field with ultra-high energy cosmic rays” Proceedings of Science (ICRC2015) **236** 557 (2015)

*The author of this thesis contributed to the strategic development of the analysis technique, performed the execution of many partial analyses. The text of the publication has been revised and copy-edited by the author of this thesis.*

**Martin Erdmann, Gero Müller, and Martin Urban**

“A Method for Investigation of the Galactic Magnetic Field using Ultra-High Energy Cosmic Rays”

Proceedings of Science (EPS-HEP2015) **234** 415 (2016)

*The author of this thesis contributed to the strategic development of the analysis technique, performed the execution of all partial analyses and provided all figures. The text of the publication has been revised and copy-edited by the author of this thesis.*

**Martin Urban, Martin Erdmann, and Gero Müller**

“Sensitivity of a search for cosmic ray sources including magnetic field effects”

Journal of Physics: Conference Series **718** 052042 (2016)

*The author of this thesis contributed to the strategic development of the analysis technique, performed the execution of all partial analyses and provided all figures. The text of the publication has been written by the author of this thesis and revised and copy-edited by the co-authors of the publication.*

**Martin Urban, Martin Erdmann, Gero Müller, and Marcus Wirtz**

“A Method of Searching for Origins of Cosmic Rays correcting for Galactic Field Deflections and Charge Composition”

Proceedings of Science (ICRC2017) **301** 518 (2017)

*The author of this thesis contributed to the strategic development of the analysis technique, performed the execution of all partial analyses and provided all figures. The text of the publication has been written by the author of this thesis and revised and copy-edited by the co-authors of the publication.*

**Martin Urban (for the VISPA group)**

“The VISPA Internet-Platform in Deep Learning Applications”

Journal of Physics: Conference Series **1085** 042044 (2017)

*The author of this thesis significantly contributed to the development of the VISPA web platform and to the design and setup of the underlying computing cluster. The text of the publication has been written by the author of this thesis and revised and copy-edited by the co-authors of the publication.*

## Internal Publications

### **Fabian Heidemann, Martin Urban, and Martin Erdmann**

“A method of event-by-event identification of cosmic nuclei using shower depth and total muon number for the Pierre Auger Observatory”

Internal note of the Pierre Auger Collaboration (2014), GAP2014-088

*The work presented in this publication is based on the Bachelor thesis of F. Heidemann which was co-supervised by the author of this thesis. The text of the publication has been revised and copy-edited by the author of this thesis.*

### **Martin Urban, Martin Erdmann, and Gero Müller**

“Combining mass composition and magnetic fields to investigate AGN correlations”

Internal note of the Pierre Auger Collaboration (2015), GAP2015-040

*The author of this thesis contributed to the strategic development of the analysis technique, performed the execution of many partial analyses and provided many figures. The text of the publication has been written by the author of this thesis and revised and copy-edited by the co-authors of the publication.*

### **Martin Urban, Martin Erdmann, and Gero Müller**

“Evidence for Magnetic Field Effects in a Search for Point Sources at the Pierre Auger Observatory”

Internal note of the Pierre Auger Collaboration (2015), GAP2015-041

*The author of this thesis contributed to the strategic development of the analysis technique, performed the execution of many partial analyses and provided many figures. The text of the publication has been written by the author of this thesis and revised and copy-edited by the co-authors of the publication.*

### **Martin Erdmann, Gero Müller, and Martin Urban**

“Discovery potential for point sources including proton identification”

Internal note of the Pierre Auger Collaboration (2015), GAP2015-042

*The author of this thesis contributed to the strategic development of the analysis and revised and copy-edited the text of the publication.*

### **Martin Erdmann, Gero Müller, and Martin Urban**

“Combining Neutrinos and Cosmic Rays to investigate the Galactic Magnetic Field”

Internal note of the Pierre Auger Collaboration (2015), GAP2015-073

*The author of this thesis contributed to the strategic development of the analysis and revised and copy-edited the text of the publication.*

### **Marcus Wirtz, Martin Erdmann, Markus Lauscher, Gero Müller, Martin Urban**

“Modelling the origin of the dipole signal”

Internal note of the Pierre Auger Collaboration (2016), GAP2016-057

*The work presented in this publication is based on the Master thesis of M. Wirtz which was co-supervised by the author of this thesis. The text of the publication has been revised and copy-edited by the author of this thesis.*

**Martin Erdmann, Martin Urban, and Marcus Wirtz**

“Constraining Nuclear Composition for Ultra-high Energy Cosmic Rays from Starburst Galaxies”

Internal note of the Pierre Auger Collaboration (2017), GAP2017-028

*The author of this thesis contributed to the strategic development of the analysis and revised and copy-edited the text of the publication.*

**Teresa Bister, Martin Erdmann, Martin Urban, and Marcus Wirtz**

“Consistency Checks between the Search Radius of the Starburst Galaxy Analysis and Deflections by Cosmic Magnetic Fields”

Internal note of the Pierre Auger Collaboration (2018), GAP2018-003

*The work presented in this publication is based on the Master thesis of T. Bister which was partly supervised by the author of this thesis. The text of the publication has been revised and copy-edited by the author of this thesis.*

**Martin Urban, Daniela Mockler, and Darko Veberič**

“Observer Data Set for Anisotropy Studies including 4T5 Events”

Internal note of the Pierre Auger Collaboration (2018), GAP2018-034

*The work presented in this publication was primarily performed by the author of this thesis. The text of this publication has been written and all figures created by the author of this thesis and was revised and copy-edited by the co-authors of the publication.*

**Teresa Bister, Martin Erdmann, Martin Urban, and Marcus Wirtz**

“Investigation of the correlation between Starburst Galaxies and the arrival directions of ultrahigh energy cosmic rays”

Internal note of the Pierre Auger Collaboration (2018), GAP2018-053

*The work presented in this publication is based on the Master thesis of T. Bister which was partly supervised by the author of this thesis. The text of the publication has been revised and copy-edited by the author of this thesis.*

**Martin Urban, Martin Erdmann, and Marcus Wirtz**

“Search for Local Structures in the Arrival Directions of Cosmic Rays using an Extragalactic Directional Filter Method”

Internal note of the Pierre Auger Collaboration (2018), GAP2018-054

*The work presented in this publication was performed by the author of this thesis. All figures were created by the author of this thesis and the text was revised and copy-edited by the author of this thesis.*

# Danksagung

An dieser Stelle möchte ich mich bei den Menschen bedanken, ohne deren Mitwirken diese Arbeit nicht entstanden wäre.

Prof. Dr. Erdmann danke ich dafür, es mir ermöglicht zu haben an diesem interessanten und aktuellen wissenschaftlichen Thema zu arbeiten. Seine Anmerkungen waren immer weiterführend.

Weiterhin danke ich Prof. Dr. Hebbeker dafür, dass er sich freundlicherweise als Zweitgutachter zur Verfügung gestellt hat.

Für die ertragreichen Diskussionen in den wöchentlich stattfindenden Treffen danke ich der gesamten Auger Arbeitsgruppe des III. Physikalischen Instituts A. Mein besonderer Dank geht an alle Personen, die Teile meiner Arbeit Korrektur gelesen haben, hier sind besonders Marcus Wirtz, Florian Briechle, Jonas Glombitza, Teresa Bister und mein Bruder Stephan Urban zu erwähnen.

Ein großes Dankeschön möchte ich auch meiner Freundin Julia Baier aussprechen, sie unterstützt mich stets und hat mir besonders in den Zeiten, in denen die Ergebnisse finalisiert wurden und die schriftliche Form Arbeit verfasst wurde, den Rücken gestärkt. Weiterhin möchte ich mich auch bei meinen Eltern für ihre stetige Unterstützung bedanken.